Temperature Scaling of Leakage Current in Irradiated Silicon Sensors

Dissertation
zur Erlangung des akademischen Grades
Doktor der Naturwissenschaften

vorgelegt von
Felix Wizemann
geboren in Stuttgart

Lehrstuhl für Experimentelle Physik IV
Fakultät Physik
Technische Universität Dortmund
2019

Der Fakultät Physik der TU Dortmund zur Erlangung des akademischen Grades eines Doktors der Naturwissenschaften vorgelegte Dissertation.

1. Gutachter : Prof. Dr. Kevin Kröninger
2. Gutachter : Dr. Johannes Albrecht
Vorsitzender der Prüfungskommission: Prof. Dr. Götz S. Uhrig
Weiteres Mitglied der Prüfungskommission: PD Dr. Catalin Gainaru

Datum des Einreichens der Arbeit: 30. September 2019
Datum des mündlichen Prüfung: 09. Dezember 2019

Abstract

With the High Luminosity LHC (HL-LHC) upgrade, the tracking detector of the ATLAS experiment will be replaced by the Inner Tracker (ITk) which uses silicon pixel and strip sensors. In Dortmund, modules for the ITk strip detector end cap will be built. The development of the production work flow of these modules is part of this thesis.

During the operation of the ITk, radiation damage will cause an increase in the leakage current of its silicon sensors, which can be scaled with temperature using the parameter E_{eff}. In previous studies, this parameter was determined to be 1.21 eV for samples irradiated to fluences up to $1 \times 10^{15}\,\text{n}_{\text{eq}}\text{cm}^{-2}$. Sensors irradiated to higher fluences have shown lower values of E_{eff}. To investigate this change in scaling behaviour, E_{eff} is determined in this thesis as a function of the applied bias voltage for irradiated samples with fluences from $6 \times 10^{14}\,\text{n}_{\text{eq}}\text{cm}^{-2}$ to $3 \times 10^{15}\,\text{n}_{\text{eq}}\text{cm}^{-2}$. It is observed that E_{eff} is dependent on voltage and that 1.21 eV is only applicable above depletion voltage.

Zusammenfassung

Mit dem Ausbau zum High Luminosity LHC (HL-LHC) wird der Spurdetekor des ATLAS Experiments durch den Inner Tracker (ITk) ersetzt, der Pixel- und Streifensensoren aus Silizium nutzen wird. In Dortmund werden Module für die Endkappe des ITK Streifendetektors gebaut werden. In einem Teil der Arbeit wird der Ablauf der Produktion dieser Module entwickelt.

Während des Betriebs werden Strahlenschäden den Leckstrom der Siliziumsensoren erhöhen. Mit Hilfe des Parameters E_{eff} kann dieser mit der Temperatur skaliert werden. Studien haben gezeigt, dass dieser Parameter 1.21 eV für Sensoren beträgt, die zu einer Fluenz von bis zu $1 \times 10^{15}\,\text{n}_{\text{eq}}\text{cm}^{-2}$ bestrahlt wurden. Bei höherer Bestrahlung wurde ein niedriger Wert für E_{eff} beobachtet. Um diese Änderung in der Skalierung mit der Temperatur zu untersuchen, wird E_{eff} in dieser Arbeit für bestrahlte Sensoren mit Fluenzen zwischen $6 \times 10^{14}\,\text{n}_{\text{eq}}\text{cm}^{-2}$ und $3 \times 10^{15}\,\text{n}_{\text{eq}}\text{cm}^{-2}$ in Abhängigkeit von der angelegten Spannung bestimmt. Es wird beobachtet, dass E_{eff} spannungsabhängig ist und 1.21 eV nur oberhalb der Depletionsspannung anwendbar ist.

Contents

Introduction

The search for elementary particles as building blocks of matter has been a scientific objective since the concept of matter built from discrete units was developed in ancient Greece. This search has resulted in the standard model of particle physics describing the elementary particles and fundamental forces. This model consists of three generations of quarks and leptons, four gauge bosons and the higgs boson which interact through the electroweak and the strong nuclear force.

As particles get smaller, the necessary energy to study them increases. Therefore, the interactions of accelerated particles with a target are used. To reach even higher energies, two counterpropagating beams are collided. In the collision of two particles, new particles can be created. They or the products of their decay can now be detected in a detector surrounding the point where the beams collide. Such detectors consist of multiple subdetectors which study different particle properties, such as momentum and charge. Today, the Large Hadron Collider (LHC) [1] is the largest particle accelerator in the world. After the start of its physics program in 2011, ATLAS and CMS, two multi-purpose experiments at the LHC, were able to complete the standard model with the discovery of the higgs boson in 2012 [2, 3]. An ongoing effort is the study of the properties of the higgs boson. To improve the precision of these results, the High Luminosity LHC (HL-LHC) upgrade is planned to be implemented in the middle of the next decade providing higher event rates for added statistics. This could shed light on what lies beyond the standard model and answer questions about dark matter and the matter-antimatter asymmetry.

The LHC, the HL-LHC and the ATLAS experiment with its subdetectors are discussed in Chapter 1. As silicon sensors, which are used to track charged particles, are the topic of this thesis, a brief introduction into semiconductors, their interaction with particles and their use as sensors in particle physics experiments is provided in Chapter 2.

With the HL-LHC upgrade, the track density in the detector increases significantly. Therefore, the ITk, an all-silicon tracking detector, which is presented in Chapter 3, will replace the Inner Detector (ID). Modules for the end cap of the strip detector of the ITk will be produced in Dortmund. Their production flow is discussed in Chapter 4.

The main scope of this thesis is the study of leakage current behaviour of silicon diodes irradiated to fluences in the range expected for the ITk strip detector, which is presented in Chapter 5. The focus lies on the investigation of the scaling of leakage current with temperature. A novel approach of this thesis is to study the scaling as a function of the applied bias voltage. Part of this study has been published in [4]. Chapter 6 summarises the results of this thesis and provides an outlook.

1. The LHC and the ATLAS Experiment

CERN, located near Geneva, Switzerland, is the leading centre of particle physics. Since its founding in 1953 [5], it has housed many particle physics experiments as well as particle accelerators. Research at CERN contributed greatly to establishing the Standard Model of particle physics. An example for this is the discovery of the W-Boson in 1983 by the UA1 and UA2 experiments at the Super Proton Synchrotron (SPS) [6, 7]. The standard model serves today as a model for fundamental forces and elementary particles.

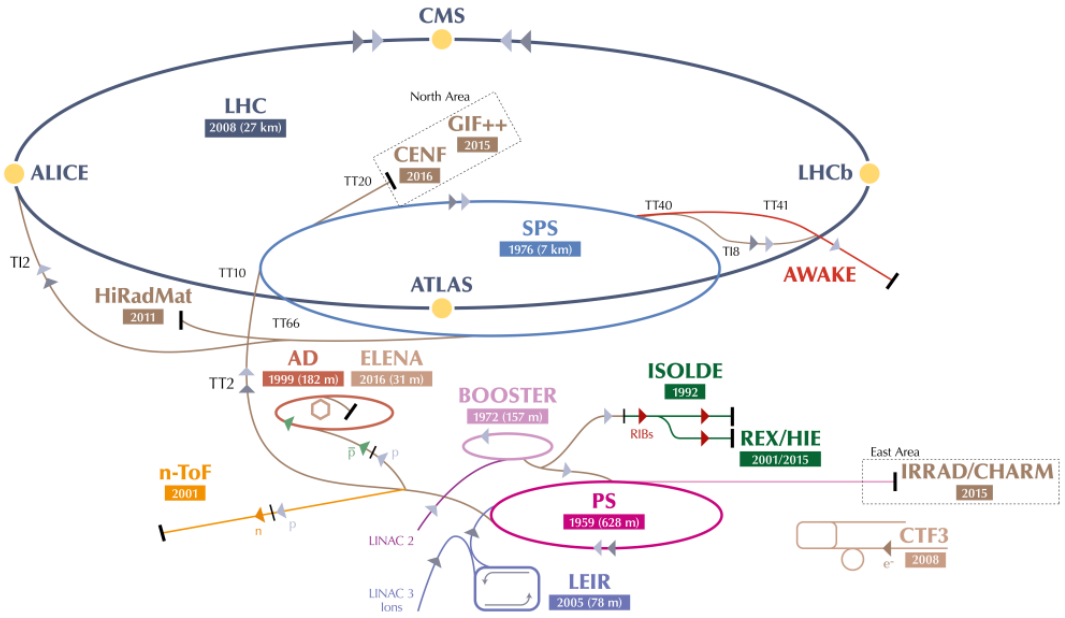

Figure 1.1.: The accelerator complex at CERN. [8], modified

1.1. The LHC

The current accelerator complex at CERN is shown in Figure 1.1. Over the years, the complex has grown to its current size. Newer accelerators were added to the complex and old accelerators were replaced or upgraded in order to gain new capabilities. The Large Hadron Collider (LHC), which saw first collisions in 2009, is currently the largest particle accelerator in the world with a circumference of 27 km and a maximum centre of mass energy $\sqrt{s}$ of 14 TeV. To operate the LHC, four pre-accelerators are used to accelerate protons to the necessary energy for injection into the LHC: The LINear ACcelerator 2 (LINAC 2, to be replaced by LINAC 4), the BOOSTER, the

Proton Synchrotron (PS) and the SPS. In addition to their use as pre-accelerators, the BOOSTER, the PS and the SPS provide particles for the beamlines of fixed target experiments.

After the discovery of the top quark in 1995 [9, 10], the last missing piece of the Standard Model was the higgs boson. Its discovery was a major goal of the LHC, which was achieved in 2012 when it was first observed at an energy of 125 GeV[2, 3].

Figure 1.2.: The (HL-)LHC schedule as of May 2018 [11]

The LHC is able to accelerate protons as well as heavy ions in two opposing beams. Bunches of particles from the two beams can be brought to collision at four interaction points, where major experiments are located. The operation of the LHC is divided into multi-year runs. Between these runs, Long Shutdowns (LSs) take place in which the accelerator and the machines are upgraded. The schedule is shown in figure 1.2.

In 2009, LHC started operations in Run 1 at $\sqrt{s} = 7\,\text{TeV}$, which was increased to 8 TeV in 2012. For Run 2 starting in 2015, $\sqrt{s}$ was increased to 13 TeV. A further increase of $\sqrt{s}$ to the maximum of 14 TeV is scheduled for Run 3 which starts in 2021. Along with the energy, the instantaneous luminosity was increased. The nominal luminosity of $1 \times 10^{34}\,\text{cm}^{-2}\,\text{s}^{-1}$ was reached at the start of Run 2. Due to the excellent performance of the LHC, double the nominal luminosity was achieved at the end of Run 2 and a further increase is foreseen for Run 3. The High Luminosity LHC (HL-LHC), an upgrade significantly increasing the luminosity, is foreseen to be completed in 2026.

At each of these interaction points, one of the four major LHC experiments is located: ATLAS, CMS, ALICE and LHCb.

1.1.1. ATLAS

The ATLAS (A Toroidal LHC ApparatuS) experiment is a general purpose detector at Point 1, one of the LHCs interaction points. The layout of ATLAS is optimised to be able to discover and study heavy particles, for example the higgs boson and the top quark, at a high instantaneous luminosity.

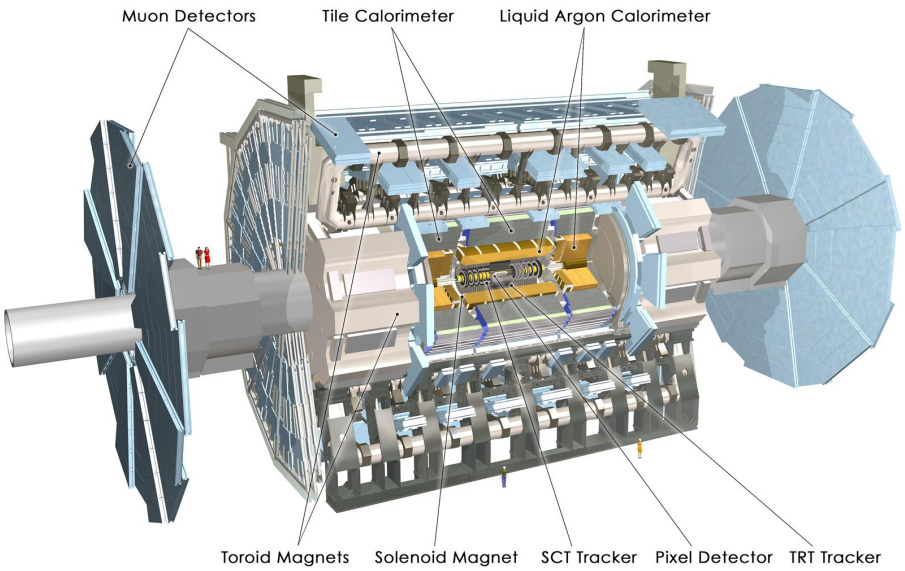

Figure 1.3.: Schematic view of the ATLAS detector. [12]

The nominal luminosity of $1 \times 10^{34}\,\mathrm{cm}^{-2}\,\mathrm{s}^{-1}$ at the LHC is achieved with multiple collisions per bunch crossing (pile-up). To be able to separate the tracks from each vertex and detect secondary vertices, a high granularity is necessary. The luminosity also causes high radiation levels, especially close to the interaction point. Therefore, detectors need to be sufficiently radiation hard. Due to wide range of physics processes studied, a large acceptance in pseudorapidity $\eta = -\ln\tan(\theta/2)$[1] is required. This results in a 4π-detector surrounding the interaction point from nearly all angles using highly granular subdetectors.

The detector is a cylinder with a length of 44 m and a diameter of 25 m and a weight of 7000 t. The layout of the ATLAS detector, which is shown in Figure 1.3, is typical for a particle detector: A tracking detector, the ID, is the innermost layer. The ID is used to gain information about the trajectory of a charged particle, its charge and its momentum. The next layers are the electromagnetic and hadronic calorimeters which measure the energy of particles by stopping them and measuring the energy deposited during the process. Two types of particles are able to fully traverse the calorimeters: muons and neutrinos. Muons are measured in the next layer: the muon system. Similar to the tracker, the muon spectrometer measures the trajectory of muons to get a precise measurement of their momentum. Neutrinos cannot be measured directly in the ATLAS detector. The interactions of different particles in the detector are shown in Figure 1.4. To be able to measure the momentum and charge of a charged particle in a tracking detector, a magnetic field is necessary to bend the trajectories of these particles. ATLAS uses two systems: a superconducting

[1] The following coordinate system is used for the description of the detector: The origin is the interaction point with the z-axis along the beampipe. The x axis points from the interaction point to the centre of the LHC ring and the y-axis points upwards. In the (x,y) plane, cylindrical coordinates (R,ϕ) are used. The angle from the beam axis is called θ.

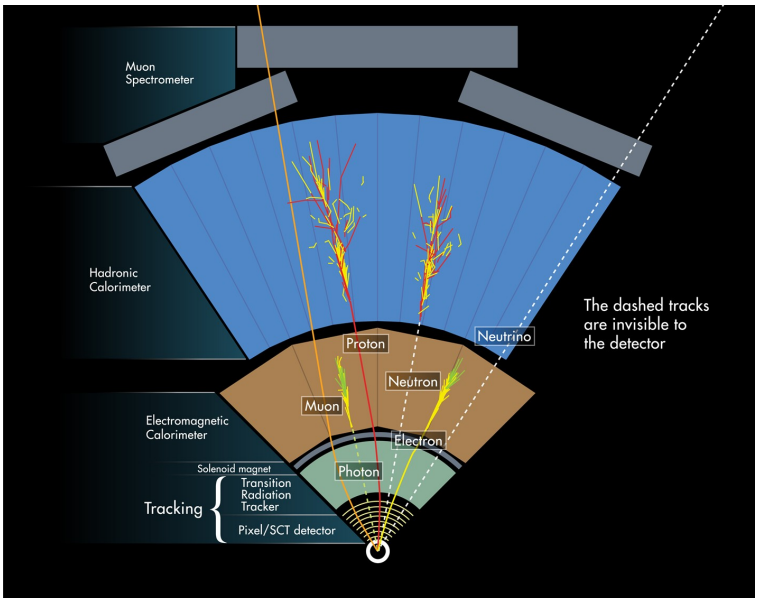

Figure 1.4.: Detection of particles in the different subdetectors. [13]

air-core toroid magnet system for the muon spectrometer and a superconducting air-core solenoid for the magnetic field in the Inner Detector (ID).

ATLAS is divided into the barrel and the end-cap region. The barrel covers the low η region and consists of detector planes longitudinal to the beam axis. The end-cap segments of the subdetectors are at a higher z than their counterparts in the barrel region. Their detector planes are transverse to the beam axis.

The Inner Detector

The ID of the ATLAS experiment consists of multiple subdetectors. The layout of the barrel is shown in Figure 1.5 and the end-cap region can be seen in Figure 1.6. It has a length of 7 m and an outer radius of 1.1 m and covers a pseudorapidity of up to $|\eta| = 2.5$. It is located in a 2 T magnetic field generated by the solenoid.

The goal of a tracking detector like the ID is to provide excellent vertex and momentum resolution. This has to be achieved while minimising cost and material. Therefore, multiple detector technologies are used in the ID, which provide the best compromise at their respective location in the detector. The innermost of the three subdetectors is the pixel detector. The pixel detector consists of four layers of silicon pixel detectors in the barrel and three disks per end-cap. The next subdetector is the Semi-Conductor Tracker (SCT) consisting of four double layers in the barrel section and nine disks per side in the end-cap. Each module in a double layer consists of two slightly twisted sensors to provide a single tracking point. The third subdetector is the Transition Radiation Tracker (TRT) consisting of straw tubes. The TRT typically provides 36 tracking points on top of the seven provided by the strips and pixels.

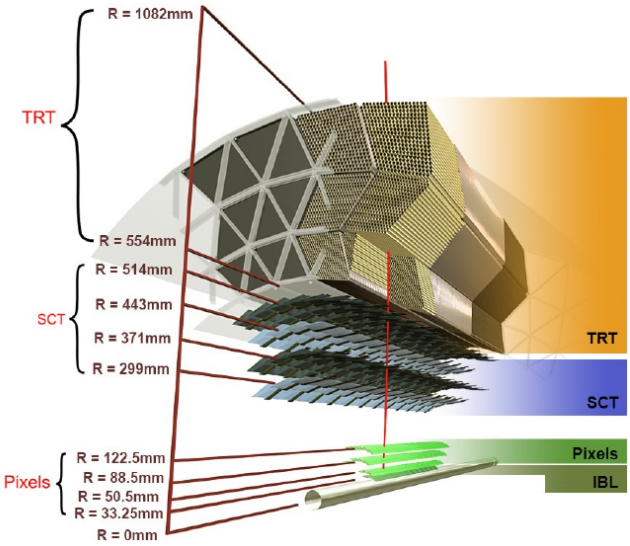

Figure 1.5.: Crosssection of the Inner Detectors barrel section after installation of the IBL. [14]

The Pixel Detector

All layers of the pixel detector use hybrid pixel detectors. This means pixels are read out by an application-specific integrated circuit (ASIC) which is connected to each pixel with a bumpbond. In the outer three layers, 16 FrondEnd (FE) I3 readout ASICs are connected to a single planar sensor forming one module with a total of 46080 readout channels. A total of 1744 of these modules are used in the pixel detector. A standard pixel has a size of 50 µm × 400 µm. At the edges of the ASICs, pixels have varying dimensions to cover the gap between the chips. The pixel detector is designed for fluences up to $1 \times 10^{15} n_{\text{eq}} \text{cm}^{-2}$ [2].

The innermost layer of the pixel detector is the Insertable B-Layer (IBL). The IBL was added to the existing pixel detector during LS 1 in 2013. The decision to add an additional layer between the beampipe and the existing layers was motivated by the increase in luminosity beyond the nominal level. Without the IBL, the performance of the tracking system would have dropped at a higher luminosity due to bandwidth limitations and degradation of the modules caused by the increased level of radiation. Because of its close proximity to the interaction point, the IBL is exposed to higher levels of radiation and is therefore designed for fluences up to $5 \times 10^{15} n_{\text{eq}} \text{cm}^{-2}$.

The IBL has a standard pixel size of 50 µm × 250 µm. It uses the newer FE-I4 readout ASICs. It consists of 14 staves with 32 readout FE-I4s each and 26880 pixels per FE-I4.

[2] The fluence is normalised to an equivalent fluence of 1 MeV neutrons and is used to quantify radiation damage to the silicon bulk. For further details, see Section 5.1.

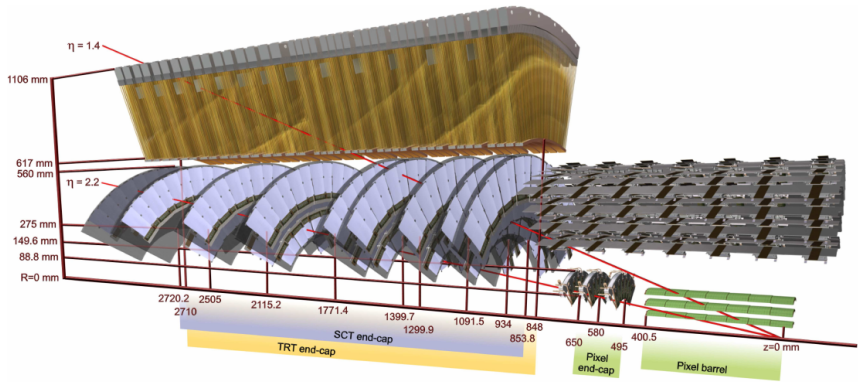

Figure 1.6.: Drawing of the Inner Detector with two tracks at $\eta = 1.4$ and $\eta = 2.2$ showing the end-cap region. The barrel section of the TRT is not shown. [15]

The Semi-Conductor Tracker

The SCT is made of silicon micro strip modules. The sensors have a thickness of 285 µm and are read out via AC-coupled strips on the p-side. The SCT is designed for fluences up to $2 \times 10^{14} n_{\text{eq}} \text{cm}^{-2}$.

The 2112 barrel modules (see Figure 1.7) use four sensors: two on the front and two on the back side of a baseboard. The baseboard is used for mechanical stability, cooling and to apply the bias voltage of up to 500 V to the sensors. The sensors on front and back are rotated by 20 mrad around the geometric centre of the module. With this rotation, the module is able to provide a single tracking point for a particle passing through both layers with a resolution of 17 µm in R-ϕ and 576 µm in z[15]. Binary readout chips are mounted on a polyimide hybrid bridging the sensor. They are connected via wirebonds to the AC-coupled strips of the sensors. The strips have a pitch of 80 µm.

The SCT has three types of end-cap modules: inner, middle and outer modules. The modules use wedge shaped sensors which are mounted on a spine (similar to the baseboard for barrel modules). The strips point towards the beamline. Therefore, they are not parallel and have a varying pitch. The middle and outer modules have two sensors on each side of the spine. In these modules, the strips of the first sensor are connected to the corresponding strip on the other sensor and read out as a single channel. The hybrids with the readout chips are mounted on the outer end of the sensors for the inner and middle modules and on the inner end for the outer modules. Fan-outs are used between sensor and readout chips due to the different pitch.

The SCT is designed for an operation temperature of −7 °C. This is achieved with a evaporative cooling system using C_3F_8 (perfluoropropane) as a coolant which is supplied via tubes through the support structure.

The Transition Radiation Tracker

The TRT is the outermost subdetector of the ID. It uses straw tubes with a central electrode wire which collect the gas ionised by traversing charged particles as well

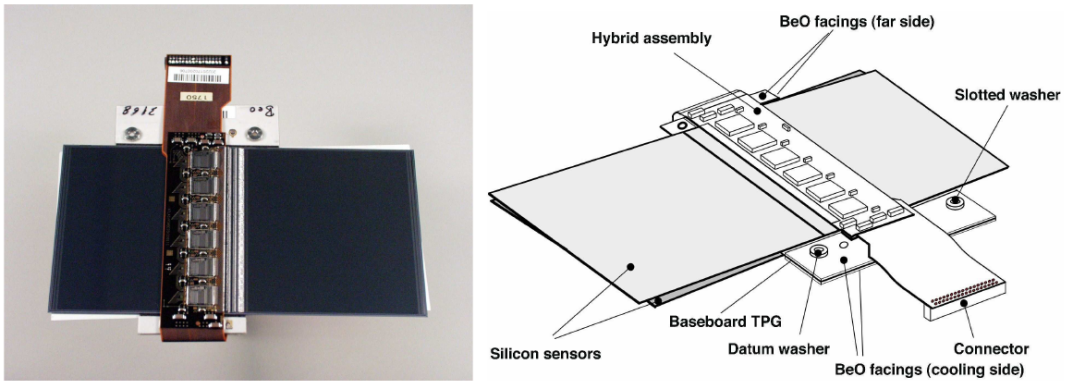

Figure 1.7.: Picture and schematic drawing of a ATLAS SCT barrel module. [15]

as the transition radiation emitted by a particle passing the interface of two media. Due to the linear scaling of the intensity of the transition radiation with the Lorentz factor γ, the mass of particles with a known energy can be determined. This feature improves the particle identification in the ATLAS experiment, especially the identification of electrons and pions. The tracking information from the TRT is limited to R-ϕ with an intrinsic resolution of 130 µm of the straw tubes. Due to the up to 36 measurements over a long track length, the TRT significantly contributes to the momentum resolution even though its precision is lower than the resolution of the two semiconductor trackers.

The detector consists of 73 layers of straws in the barrel and and 160 straw planes in the end-cap, totalling 35100 channels. The 144 cm long straws in the barrel are arranged in parallel with the beam axis and the 37 cm long straws are aligned radially to the beam axis covering up to $|\eta| = 2$. The straws are made of two layers of foil. The polyimide foil is coated with an adhesive on one side and a thin Al layer on the other side. The Al layer is under a protective graphite-polyimide layer and serves as electrical conductor. The adhesive sides of the two layers are facing each other. A gold plated tungsten wire serves as the electrode inside the tube. In between the straws are polypropylene fibres to generate transition radiation.

The gas used inside the tubes was selected to have a stable working point while efficiently absorbing transition radiation [16]. It was also important for the selection of the gas that it is not flammable and does not damage the detector during operation. This has lead to a mixture of 70 % Xenon, 27 % CO_2 and 3 % O_2. With this choice, transition radiation signals are larger than tracking signals and can be separated by using a high and a low threshold.

The calorimeter system

The calorimeter system of ATLAS consists of an electromagnetic (EM) calorimeter, a hadronic calorimeter and a forward calorimeter.

The high granularity EM calorimeter is a sampling calorimeter using liquid Argon (LAr) as active medium and lead as absorber. It has an accordion structure to achieve symmetry in ϕ without any cracks. It covers a pseudorapidity of up to $\eta = 2.5$ with

the high granular barrel and outer wheel in the end-cap, matching the acceptance of the ID and up to $|\eta| = 3.2$ with the less granular inner end-cap wheel. It covers a minimum of 22 radiation lengths (X_0). Its relative energy resolution was determined in test-beam measurements with electrons to be $\frac{\sigma_E}{E} = \frac{10\%\sqrt{\text{GeV}}}{\sqrt{E}} \oplus 0.17\%$.

The hadronic calorimeter system is made up of the tile calorimeter (TileCal) in the barrel and the Hadronic End-cap Calorimeter (HEC). The tile calorimeter is a sampling calorimeter and uses scintillator tiles with steel as an absorber covering up to $|\eta| = 1.7$. The HEC uses liquid argon as active medium and covers up to $|\eta| = 3.2$. Together with the EM calorimeter, the hadronic calorimeters have a minimum of 11 interaction lengths (λ) to avoid punch through into the muon system. In the barrel region, the TileCal achieves in combination with the LAr EM calorimeter a combined resolution of $\frac{\sigma_E}{E} = \frac{52\%\sqrt{\text{GeV}}}{\sqrt{E}} \oplus \frac{1.6\,\text{GeV}}{E} \oplus 3\%$ for pions.

The forward calorimeter is a sampling calorimeter using liquid argon as well and covers up to $|\eta| = 4.9$ and has a thickness of 10 interaction lengths. It is made up of three modules. The first one uses copper as absorber to measure the energy of electromagnetic particles. The other two modules use tungsten to absorb hadrons.

The calorimeter system is used for the Level-1 calorimeter trigger (L1Calo) trigger.

The muon spectrometer

The muon spectrometer measures the trajectories and momenta of charged particles (mostly muons) that have traversed the calorimeter. The spectrometer covers a pseudorapidity of up to $|\eta| = 2.7$ and uses Monitored Drift Tube chambers (MDTs) in the barrel and Cathode-Strip chambers (CSCs) in the end-cap for tracking, both filled with an Ar/CO_2 mixture. It is also provides signals for the Level-1 muon trigger (L1Muon) from fast trigger chambers distributed throughout the spectrometer.

Trigger system

The Level 1 (L1) hardware trigger is used to reduce the data rate from the bunch crossing rate of 40 MHz down to 75 kHz and makes the decision to store or delete an event in a time frame of 2.5 µs. The L1 trigger uses the information from the L1Muon and L1Calo triggers to select events with particles with high transversal energy (E_T) or high missing transversal energy ($E_{T,\text{miss}}$). The software based triggers are used for a further reduction to 200 Hz.

Upgrades in Long Shutdown 2

With the increase in luminosity after LS 2, upgrades of various detector components are planned during the shutdown. This is necessary to keep the trigger bandwidth constant while keeping the thresholds low. The background in the muon system will increase well above design levels. The innermost tracking station in the end-cap is especially affected by this and will be replaced with the New Small Wheels (NSW). This is necessary to avoid an increase in fake triggers and a degradation of the resolution of the muon momentum. The NSW will use multiple small-strip

Thin Gap Chamber (sTGC) for the L1Muon trigger and Micromegas[3][17] detectors for precision tracking.

The L1Calo is another system which will be upgraded in LS 2. This upgrade enables the use of a higher granularity in the calorimeter for the trigger decision and improve background rejection. The new Fast Track Trigger (FTK) system uses data from the pixel detector and the SCT to reconstruct tracks after a L1 trigger as input for the software trigger. This enables the software trigger to use vertex information in its decisions.

1.1.2. CMS

CMS (Compact Muon Solenoid) is a general purpose, 4π detector with similar physics goals as the ATLAS detector. With a length of 21.6 m, a radius of 14.6 m and a mass of 12 500 t, CMS is much denser than ATLAS.

CMS uses a single magnet, the eponymous superconducting solenoid. The inner tracker and the calorimetry are in the bore while the muon system uses the return field. The inner tracker is an all-silicon design originally consisting of three pixel layers and ten layers of strip detectors. In 2017, the pixel detector was replaced with a higher granularity pixel detector with a fourth layer [18]. The electromagnetic homogeneous calorimeter uses scintillating lead tungstate crystals. The hadronic calorimeter is a sampling calorimeter using a brass/scintillator design. The muon system uses Drift Tubes (DTs) in the barrel and CSCs in end-cap for tracking as well as Resistive Plate Chambers (RPCs) for triggering.

1.1.3. LHCb

The LHC-beauty (LHCb) experiment is designed for the study of rare decays of beauty and charm hadrons as well as CP violation [19]. Beauty hadrons are mainly produced in an event with a $b\bar{b}$ pair. Predominantly, both the b and the $\bar{b}$ hadrons are produced in the same forward or backward cone. Therefore, LHCb is not a 4π detector but a single-arm detector covering a pseudorapidity from $\eta = 2$ to $\eta = 5$.

Starting at the collision point, the vertex locater system (VELO) is the first subdetector using silicon microstrip sensors followed by the first Ring Imaging CHerenkov counter (RICH) whose primary goal is particle identification. Next is the tracking system consisting of silicon microstrip trackers, which are used for triggering, followed by the magnet system and a further three tracking stations made up of silicon microstrip detectors close to the beampipe and straw tubes in the outer regions. This is followed by the second RICH, the calorimeters and the muon system.

1.1.4. ALICE

A Large Ion Collider Experiment (ALICE) is a general purpose detector focusing on heavy-ion collisions (lead-lead and lead-proton) [20]. The aim is to study the Quantum ChromoDynamics (QCD) in quark-gluon plasma after a collision involving heavy nuclei. A major challenge in this study is the large particle multiplicity after the

[3] MICRO-MEsh-GAseous Structure

decay of a quark-gluon plasma requiring ALICE to have excellent particle separation and particle identification capabilities.

ALICE is built from a barrel section and a forward muon spectrometer arm. The barrel section consists of the Inner Tracking System consisting of six layers of silicon detectors and a Time-Projection Chamber for tracking. Particle Identification is provided by Time-of-Flight, Ring Imaging Cherenkov and Transition Radiation detectors. Two electromagnetic calorimeters are used for energy measurements. The muon arm uses absorbers to isolate muons, which are then tracked in a magnetic field.

1.2. The High Luminosity LHC

The HL-LHC is a future upgrade of the LHC to greatly increase its instantaneous luminosity in order to achieve an integrated luminosity of $4000\,\mathrm{fb}^{-1}$ after a decade of operation. The HL-LHC is needed since the running time necessary to reduce the statistical uncertainty on a given measurement will exceed 10 years in 2020 [21]. The HL-LHC upgrade is to be installed in LS 3 to be operational in 2026.

The increased integrated luminosity allows to study the standard model with increased precision, enhances the study of rare channels and furthers the reach for discoveries beyond the standard model. For the ATLAS Experiment, a focus of the HL-LHC physics program will be the precision measurement of production and decay channels of the Higgs boson. For example, the HL-LHC enables the detailed study of the decay of a Higgs boson into two muons ($H \to \mu\mu$). This will allow to compare the coupling of a Higgs boson to the second and third (via $H \to \tau\tau$) lepton generation with standard model predictions and to test for possible influences of physics beyond the standard model (BSM physics) [22]. Detailed discussions of the physics prospects of the HL-LHC can be found in the reports of the working groups of the *HL/HE-LHC Physics Workshop* in the sectors of standard model physics, Higgs physics, physics beyond the standard model, flavour physics and high-density QCD [23–27].

To achieve the ten-fold increase in integrated luminosity, the instantaneous luminosity needs to be increased. Therefore the design luminosity is increased to $7.5 \times 10^{34}\,\mathrm{cm}^{-2}\,\mathrm{s}^{-1}$ after luminosity levelling resulting in an average pile up of 200 collisions per bunch crossing while keeping the bunch crossing rate at 40 MHz [21]. To allow vertex separation as well as reaching similar or improved track reconstruction performance, a higher granularity and improved radiation hardness is required for the tracking detector in comparison to the first three runs of the LHC.

The ID of the ATLAS experiment will not be able to meet these increased requirements. These requirements include:

- Due to the increased occupancy, the detector performance would be compromised by a decreased track finding efficiency. For example, the occupancy in the TRT would approach 100 % for a pile up of 200 collisions per event [28].
- The ID does not have enough bandwidth to cope with a pile up above 50 collisions per event. Due to the use of zero surpression in the Pixel and the SCT, the required bandwidth increases with occupancy [28].

- To be able to achieve sustainable trigger rates without increasing thresholds, information from the tracking detector is required for the Level-1 trigger which is not provided by the ID [29].

These limitations necessitate the replacement of the ID with a new tracking detector with increased granularity, radiation hardness and the readout electronics necessary to deal with the luminosity. This replacement will be the Inner Tracker (ITk), which is described in Section 3.

2. Silicon Tracking Detectors in High Energy Physics

Today, semiconductors are used in a vast variety of applications. In high energy physics, semiconductors serve in many different roles. Apart from their usage in computing and readout electronics, they are utilised as sensitive material in modern detectors. Semiconductor sensors can be engineered to serve various purposes, for example for spectroscopy with an excellent energy resolution or in tracking detectors as sensors which can resolve particle crossing with high accuracy in time and space.

This chapter provides a brief introduction about semiconductors and their use in tracking detectors of high energy physics experiments with a focus on silicon sensors. More detailed information about semiconductors and their use can be found in literature, e.g. [30–32].

2.1. Semiconductors

Based on their ability to conduct electricity, solids can be grouped into three classes: conductors, semiconductors and insulators. Semiconductors have a resistivity in the range of $1 \times 10^{-3}\,\Omega\,\mathrm{cm}$ to $1 \times 10^{8}\,\Omega\,\mathrm{cm}$ [31].

Their conductivity can be explained with the help of the band model. Electrons in the hull of an isolated atom have discrete energy levels. If multiple atoms are brought together into a structure with small distances in between them, their interactions cause the energy levels to split into multiple levels in accordance with the Pauli exclusion principle. This causes the formation of energy bands with closely spaced energy levels when atoms are arranged in a crystal structure. The outermost band with occupied energy levels at 0 K is called the valence band. The Fermi energy E_F is defined as the energy half way between the highest occupied and the lowest unoccupied energy state at absolute zero. For conductors, the valence band is either partially filled or overlapping with another band, the conduction band, resulting in a minimal resistivity. For isolaters and semiconductors, the valence band is fully filled and the conduction band with higher energy levels is empty. The energy difference between the lowest level in the conduction band and the highest level in the valence band is called the band gap energy E_g. For semiconductors, E_g is small enough for electrons to transition into the conduction band due to thermal activation. In case of silicon, E_g is 1.12 eV [31] at 300 K.

Semiconductors can be element semiconductors, for example silicon and germanium, or compound semiconductors consisting of two (for example GaAs) or more (for example CdZnTe) elements. Element semiconductor crystals have a diamond lattice structure were every atom has four equidistant nearest neighbours. A covalent bond is formed between the atom and its four nearest neighbours and a two-dimensional

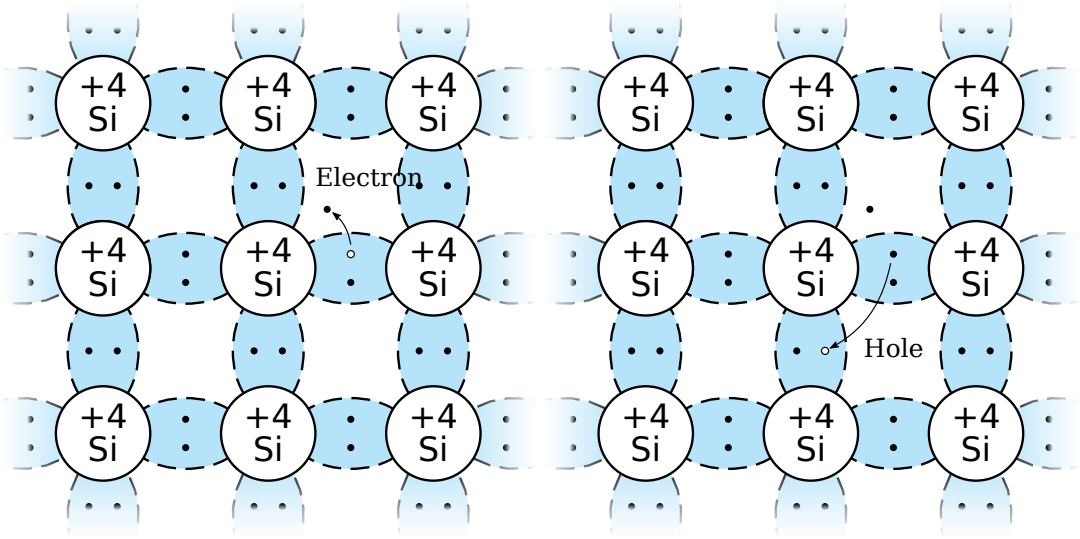

(a) An electron is excited and leaves behind a hole in the covalent bond

(b) An neighbouring electron moves into the hole and thereby dislocates the hole.

Figure 2.1.: Basic representation of the bonds and conduction in intrinsic silicon. [33], after [30]

bonding diagram is shown in Figure 2.1. In case of a transition into the conduction band (Figure 2.1a), electrons can move as free charge carriers in the lattice with the effective mass m_n. The transition of the electron into the conduction band leaves an electron deficiency in the valence band. This deficiency is called a hole. Other electrons from the valence band can fill the hole (see Figure 2.1b), which can therefore be seen as a quasi charge carrier with the effective mass m_p. The reversal of the transition into the conduction band is called the recombination, where an electron from the conduction band fills a hole. At a constant temperature, both effects are in equilibrium and the probability of an electronic state being occupied can be described with the Fermi-Dirac distribution function.

In GaAs, the lowest electronic state in the conduction band occurs at the same momentum as the highest state in the valence band and is therefore called an direct semiconductor. This is not the case in silicon, which is therefore called an indirect semiconductor. For a transition between the valence and conduction band in an indirect semiconductor, the electron needs to exchange momentum with the lattice. This results in an average ionisation energy per electron hole pair of 3.65 eV at 300 K [31].

2.2. Doping of Semiconductors

The characteristics of semiconductors can be modified by adding additional energy states and free charge carriers. This is achieved by doping the semiconductor with atoms of other elements. Such materials are called extrinsic semiconductors.

Silicon is an element of the fourth main group in the periodic system. By adding an element of the fifth main group, for example phosphorus, an additional electron

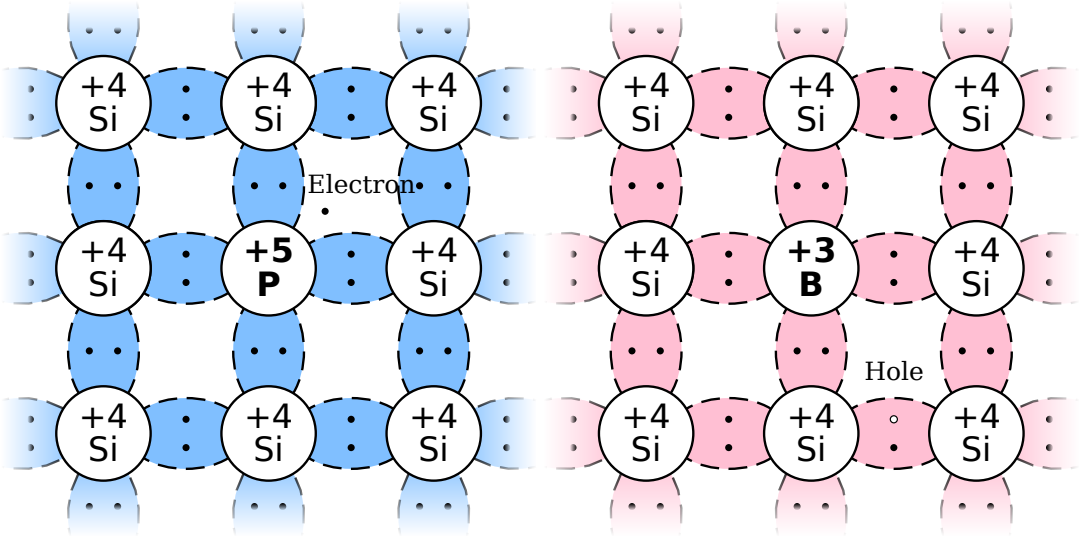

(a) Silicon doped with phosphorus. (b) Silicon doped with boron.

Figure 2.2.: Schematic bonds in a silicon lattice added a) donor or b) acceptor impurities. [33], after [30]

is added (see Figure 2.2a). Its ground state is slightly below the conduction band, in case of phosphorus in silicon 0.045 eV [30] and therefore easily excitable. The added atom "donates" the electron to the conduction band and is therefore called a donor. A semiconductor doped with donors is called an n-type semiconductor due to the added negative charge carriers.

Doping silicon with an element of the third main group, for example boron, results in a hole with an energy state slightly above the valence band (0.045 eV for boron in silicon [30]). This results in an excess of holes and the semiconductor is considered to be p-type. The added dopant is called an acceptor.

Due to these low excitation energies, dopants are typically fully ionised at room temperature. If enough dopants are added, an extrinsic region forms where the majority charge carrier concentration is essentially constant over a wide temperature region at

$$N_D = n \text{ or } N_A = p \tag{2.1}$$

with the donor concentration N_D, the electron density n, the acceptor concentration N_A and the hole density p. This region starts when all dopants are ionised and ends when the intrinsic charge carrier concentration n_i becomes dominant at high temperatures. The law of mass action states that

$$np = n_i^2 \tag{2.2}$$

is constant for a given temperature. In case of extrinsic semiconductors, the added charge carriers lead to a higher recombination rate. Therefore, the number of minority charge carriers is reduced until this condition is met.

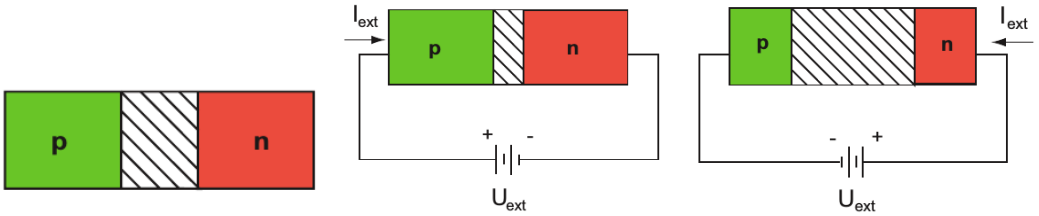

(a) (b) (c)

Figure 2.3.: Depletion zone in silicon for a) an unbiased, b) a forward biased and c) a reverse biased pn junction. [31]

Unintentional impurities, for example due to contamination in the production process can also have an influence on the semiconductor properties, for example by adding deep level traps. Those are energy states with excitation energies above $3k_BT$ with the Boltzmann constant k_B and the temperature T. Such impurities can affect the leakage current behaviour as discussed in chapter 2.4.

2.3. pn-Junction

A pn-junction is a contact between an n-type and a p-type region in a semiconductor device. For simplicity it is approximated to be an abrupt change in doping concentration. Most semiconductor detectors are based on pn-junctions.

In n-type and p-type semiconductors, the Fermi energy is different due to the added impurities. Due to the carrier concentration differences, charge carriers diffuse across the pn-junction. This causes a net exchange of charge and causes a space charge near the junction. This results in an equilibrium once the diffusion is compensated by a drift of charge carriers due to the electric field across the space charge region. Due to recombination, the space charge region is void of free charge carrier and also called the depletion zone. Due to the potential difference (the built-in voltage U_{bi}) across the space charge region, the Fermi level is constant across the junction.

If one side of the junction has a much higher doping concentration, it is called a one-sided abrupt junction. In this case, the depletion zone is much larger on the side of the junction with the lower doping concentration and overall space charge neutrality is thereby maintained. In case of a junction with a much higher concentration on the p-side (a p^+-n junction), the width W of the depletion zone is

$$W \cong x_n = \sqrt{\frac{2\epsilon U_{bi}}{qN_D}} \tag{2.3}$$

with the depletion width x_n on the n-side and the permittivity ϵ.

Figure 2.3a illustrates the situation without externally applied voltage. A forward bias (negative bias to the n-side of the junction) reduces the potential difference and therefore the depletion width as shown in Figure 2.3b. A reverse bias (shown in Figure 2.3c) increases the depletion width.

With an external voltage U, Equation 2.3 becomes

$$W = \sqrt{\frac{2\epsilon(U_{bi} - U)}{qN_D}}. \tag{2.4}$$

2.4. Current-Voltage Characteristic of a pn-Junction

For an ideal diode, the following assumptions are used:

a) The diode is one dimensional

b) The applied voltage appears across the depletion zone. Outside of the depletion zone, a field free neutral region is assumed.

c) There is no net carrier generation or recombination in the depletion zone and therefore the current is constant across the depletion zone.

d) The low-injection condition, that minority charge carrier densities remain small in comparison to majority charge carrier densities, is met.

Under these assumptions, the current I_{ideal} of an ideal diode is described as

$$I_{\text{ideal}} = I_S(\exp(qU/k_BT) - 1) \text{ with} \tag{2.5}$$

$$I_S = qAn_i^2 \left(\frac{D_p}{N_D L_p} + \frac{D_n}{N_A L_n} \right), \tag{2.6}$$

where I_S is the saturation current, A is the junction area, D_p and D_n are the respective diffusion coefficients of holes and electrons, L_p and L_n are the respective the diffusion length of holes and electrons, and q is the elementary charge.

For real passive silicon sensors, the conditions of an ideal diode are not met. The dominant effects causing this are the generation of current in the depletion zone (bulk currents) and surface currents.

The bulk current is generated from energy levels in the bandgap. To generate free charge carriers, an electron needs to move from the valence band into the trap level in a hole emission and then be emitted into the conduction band. The emission probabilities ϵ of electrons and holes are

$$\epsilon_n = \nu_{\text{th},n}\sigma_n n_i \exp\left(\frac{E_t - E_i}{kT} \right), \tag{2.7}$$

$$\epsilon_h = \nu_{\text{th},h}\sigma_h n_i \exp\left(\frac{E_i - E_t}{kT} \right) \tag{2.8}$$

with the intrinsic Fermi level E_i, the trap level E_t, the thermal velocity ν_{th} and the capture cross-section σ for electrons and holes respectively [34]. Therefore, energy levels close to the intrinsic Fermi energy are dominant carrier generation centres. For reverse biased diodes, the recombination rate U for such levels can be expressed as

$$U = -\frac{n_i}{2\tau} \tag{2.9}$$

with the effective carrier lifetime τ. The negative U results in the current I_{gen} being generated in the depleted volume. Integration over the depletion zone results in

$$I_{\text{gen}} = qA \int_{-x_p}^{x_n} U dx = -qWA\frac{n_i}{2\tau}. \tag{2.10}$$

Passive silicon sensors for particle tracking are typically operated with a reverse bias large enough to deplete the entire volume. Therefore the generation current remains constant with a further increase in voltage.

For real diodes under reverse bias, the current can be written as

$$I = I_{\text{ideal}} + I_{\text{gen}}, \tag{2.11}$$

which results in an increase of the reverse volume current I with voltage until I_{S} is reached and the entire volume is depleted. I_{S} scales with n_i^2 while I_{gen} scales with n_i. Therefore, I_{gen} dominates when n_i is low, for example in silicon up to 175 °C [32]. If n_i is high, for example in germanium at room temperature, I_{S} dominates.

In most cases, surface currents are caused by contamination or damage on the surface caused in production or during handling of the device. The contribution of the surface to the total current can be identified due to its linear increase with voltage while the current generated in volume increases with the depletion depth. Typically, the total current is dominated by the reverse volume current [31].

For silicon sensors used in particle physics, the total reverse current is dominated by I_{gen}. For these devices, an abrupt breakdown occurs at high bias voltages. The breakdown is due to an avalanche effect. It occurs, when the electric field is high enough for electrons to gain enough kinetic energy between collisions to break lattice bonds creating new free charge carriers. They can now gain enough kinetic energy on their own which results in avalanche multiplication.

In Figure 2.4, the bulk current of a diode is shown in a current-voltage (I-V) plot. As expected from Equation 2.10, the current increases with the applied bias voltage proportional to the increase of the depletion width (see Equation 2.4) until full depletion is reached around 200 V and remains nearly constant afterwards in what is called the plateau region. In this example, no breakdown occurs up to 1000 V.

2.4.1. Temperature Scaling of the Generation Current in Silicon

The volume current in silicon increases with temperature. Here, the change with temperature is described for devices dominated by I_{gen}. A more detailed derivation can be found in References [35, 36]. In Equation 2.10 for the generation current, there are two contributions which depend on the temperature.

The first one is the intrinsic carrier concentration

$$n_i(T) \propto T^{3/2} \exp\left(\frac{-E_g}{2k_B T}\right). \tag{2.12}$$

The second one is the mean charge carrier lifetime τ. Charge carrier generation is most efficient for traps close to the band gap energy. Therefore, an approximation for a single trap level E_t can be used.

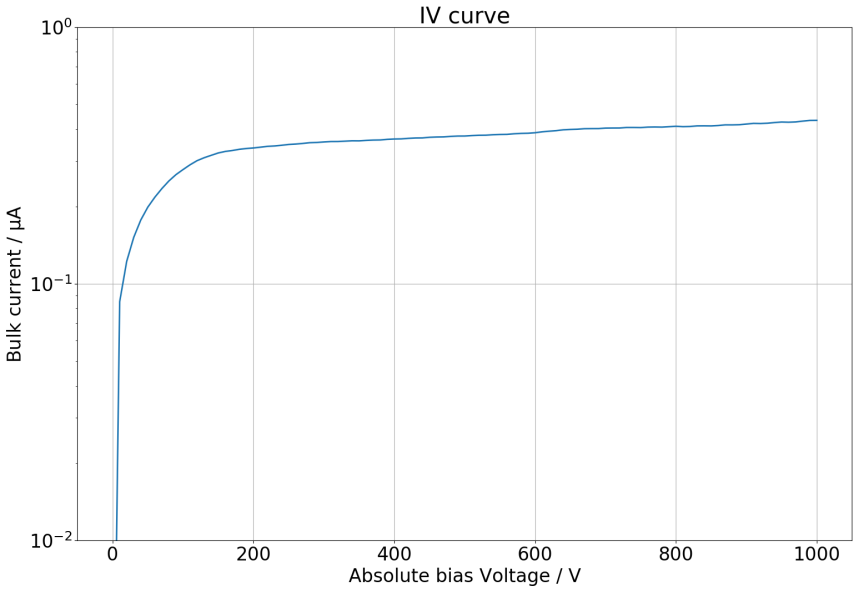

Figure 2.4.: Example of the bulk current against the bias voltage in a silicon diode.

According to Reference [34],

$$\tau = \frac{1}{N_t}\left(\frac{\exp\frac{E_t-E_i}{k_BT}}{v_{tp}\sigma_p} + \frac{\exp\frac{E_t-E_i}{k_BT}}{v_{tn}\sigma_n}\right) \tag{2.13}$$

with the trap density N_t, the intrinsic Fermi energy E_i, the thermal velocity $v_{tn(p)}$ for electrons (holes) and the trapping cross-section $\sigma_{n(p)}$ for electrons (holes). Reference [35] shows with $v_t(T) \propto T^{1/2}$ and the assumption of $v_{tp}\sigma_p \approx v_{tn}\sigma_n$, that

$$\tau(T) \propto T^{-1/2}\exp\left(\frac{\Delta}{k_BT}\right) \tag{2.14}$$

with $\Delta = E_t - E_i$.

With equations 2.10,2.12 and 2.14, we get

$$I(T) \propto \frac{T^{3/2}\exp\left(\frac{-E_g}{2k_BT}\right)}{T^{-1/2}\exp\left(\frac{\Delta}{k_BT}\right)} = T^2\exp\left(\frac{-Eg+2\Delta}{2k_BT}\right). \tag{2.15}$$

As shown in Reference [37], $E_g(T)$ depends on temperature and can be approximated to $E_g(T) = E_0 - \alpha T$ with $E_0 = 1.206\,\mathrm{eV}$ and $\alpha = 2.73\times10^{-4}\,\mathrm{eV\,K^{-1}}$ for $250\,\mathrm{K} \leq T \leq 415\,\mathrm{K}$.

From this, we get

$$I(T) \propto T^2\exp\left(-\frac{E_{\mathrm{eff}}}{2k_BT}\right) \tag{2.16}$$

with the effective bandgap $E_{\mathrm{eff}} = E_0 + 2\Delta$. Due to the most efficient generation of current from traps close to the mid-level, Δ is minimal and E_{eff} can be expected to be close to E_0.

2.5. Energy Deposition of Particles in Silicon Detectors

In silicon tracking detectors, free charge carriers are generated by traversing ionising particles and collected into a readout system. The mean energy deposition of a particle with large mass in comparison to the electron mass can be described with the Bethe formula following the parameterization in [31]:

$$-\left\langle \frac{dE}{dx} \right\rangle = K \frac{Z}{A} \rho \frac{z^2}{\beta^2} \left[\frac{1}{2} \ln \frac{2 m_e c^2 \beta^2 \gamma^2 T_{max}}{I^2} - \beta^2 - \frac{\delta(\beta\gamma)}{2} - \frac{C(\beta\gamma, I)}{Z} \right] \tag{2.17}$$

with $K = 4\pi N r_e^2 m_e c^2$. The charge, the velocity and the Lorentz factor of the traversing particle are z, β and γ, Z and A are the atomic number and the mass number of medium, I is the mean energy necessary to ionise the medium, T_{max} is the maximum energy transfer in a single collision, δ is the density correction (relevant for high energies), C/Z is the shell correction (relevant for small velocities), N is the Avogadro constant, r_e is the electron radius and m_e is the electron mass.

The energy loss is dominated by elastic collisions at low energies. At $\beta\gamma \approx 3$, the Bethe formula has its minimum and particles with such energies are called Minimum Ionising Particles (MIPs). At higher energies, the energy loss increases only slightly until bremsstrahlung becomes dominant. Further details on the formula and its constituents can be found in References [31, 38, 39]. For electrons, the equation needs to be modified, which is shown in Reference [38].

Photons deposit energy in silicon through deflection in Compton scattering or through absorption by the photo effect or pair production.

2.5.1. Signal Generation in Silicon Detectors

In undepleted silicon, the excess charge carriers recombine after ionisation and return to equilibrium state and cannot reach readout electronics. Therefore, silicon detectors use the depletion zone at a pn-junction with an applied reverse bias. This prohibits direct recombination and due to the applied electric field, charge carriers drift towards the electrodes, where they induce a signal.

Silicon detectors are diodes with highly asymmetric pn-junctions with highly doped surfaces and a bulk with a low doping concentration. The bulk can be either a p-type or an n-type bulk. As shown in Figure 2.5 a) and c), this results in the depletion zone expanding from one side of the diode. Since only the charge generated in the depleted volume can be read out, full depletion (shown in Figure 2.5) is necessary to detect the maximum signal.

Equation 2.17 predicts the mean energy deposited by a particle of a specific type and energy. The distribution of the deposited energy depends on the thickness of the detector. For thick sensors, the central limit theorem is valid due to the large number of interactions and the distribution of the deposited energy is Gaussian in form as long as the total energy loss is small in comparison to the original energy.

For thin sensors, the energy deposition can be approximated with a Landau distribution, parametrised for example in [39]. It has a peak at its Most Probable Value (MPV) with a tail towards higher energies which is due to the possibility of

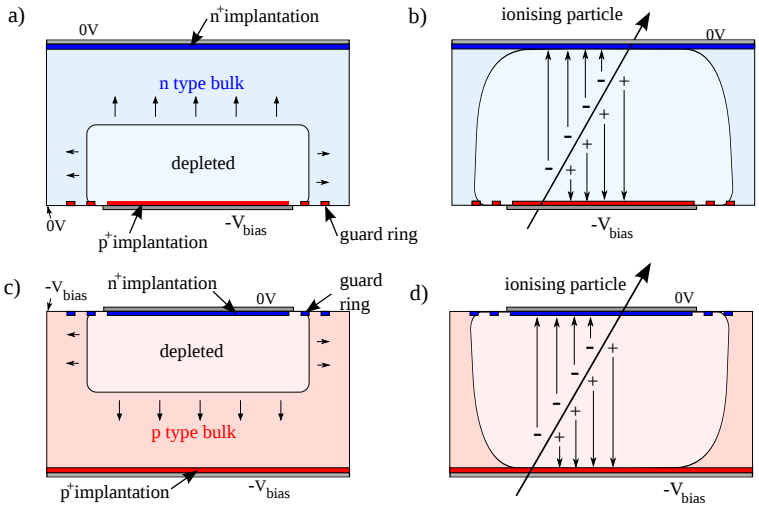

Figure 2.5.: Growth of the depleted region and ionisation in depleted n-bulk (a,b) and p-bulk (c,d) diodes. [40]

large energy transfers in a single collision. Thus, the MPV is below the mean of the distribution. Since there is no tail to lower energies, signal and noise can be easily separated with a threshold value for MPVs significantly above the noise level.

As shown in [39], the most probable energy deposited by a MIP in 300 μm silicon is 80 keV. With an ionisation energy in silicon of 3.62 eV, 22000 electron-hole pairs arecreated. Thus, a charge of 3.5 fC can be read out on either side.

2.6. Use of Silicon Tracking Detectors in High Energy Physics

In high energy physics, silicon tracking detectors are widely used, for example in the VELO of LHCb or the current and future inner tracking detectors of ATLAS and CMS. Silicon sensors are produced by using lithographic processes on the surface of mono-crystalline silicon wafers. This enables the small structures needed for highly granular designs. Due to their widespread use in industry, affordable large scale production of sensors is possible. They can be optimised for a compromise between radiation hardness, spacial resolution, precision timing and cost depending on the needs in an experiment.

Typically, a highly granular detection plane is achieved with either a double layer of strip or a single layer of pixel sensors. Both are based on diodes as shown in Figure 2.5. To increase their granularity, the implant on one side of the diode is divided into smaller implants. The implants in form of strips or pixels collect the charge of a small area of the sensor and are read out individually. This can be done either on the n^+ or the p^+ side.

The two strip sensors of a double layer are slightly rotated with respect to the other sensor. Therefore, the granularity can be achieved with significantly less read out channels and therefore, strip sensors are the more cost effective solution. Most

commonly, read out chips are glued on a PCB and are connected to the strips using wirebonds.

At high occupancy, the additional readout channels of pixel detectors are required. Thus pixel sensors are used close to the interaction point and therefore are exposed to the highest radiation levels. To be able to operate pixel sensors in high radiation environments, the distance between the electrodes is reduced. This can be achieved by using thinner wafers or by 3D sensors [41]. In 3D sensors, columns of n^+ and p^+ in the bulk are used as electrodes resulting in a smaller distance. In experiments like ATLAS, hybrid pixel detectors are used. In hybrid pixel detectors, one or multiple readout chips are bump bonded to a pixel sensor. In this process, each pixel is connected via a small solder ball to a readout channel on the readout chip.

The ITk upgrade of the ATLAS experiment, which is described in Chapter 3, uses strip sensors, planar pixel sensors and 3D pixel sensors.

3. The ATLAS ITk Upgrade

With the HL-LHC described in Section 1.2, new requirements for tracking detectors arise which lead to the decision to replace the ATLAS ID in LS 3. The new tracking detector, the Inner Tracker (ITk), is designed to deliver at least the same tracking performance as the current ID at the higher occupancy expected for the HL-LHC. Due to the increased integrated luminosity during the operation of the HL-LHC, the detector needs to be able to cope with a higher fluence than the ID. Additionally, ITk will be used for the Hardware-based Tracking for the Trigger (HTT) sub-processors of the Event Filter of the new trigger system [42].

As a result of these requirements, the ITk will be an all-silicon detector using pixel detectors in the inner and strip detectors on the outer layers. The ITk is designed for an average pile-up of $\langle\mu\rangle = 200$ and an integrated luminosity of $4000\,\text{fb}^{-1}$ at the end of its life. The ITk will use the same volume as the ID with the 2 T magnetic field from the solenoid magnet system. Apart from tracking performance, a major target is minimal use of material to achieve as little deposited energy in the detector volume as possible to improve the energy measurement in the calorimeters.

A more detailed description of the ITk can be found in the technical design reports of the ITk Pixel [43] and the ITk Strip Detector [28].

3.1. Detector Layout

The ITk is designed around the collision point where the collisions are expected to happen in a region around the nominal interaction point with a length of 50 mm. The detector's base unit is a module for the pixel and the strip detector. A module consists of one or multiple sensors which are read out by one or multiple read-out chips. These modules are mounted on a local support structure, for example a stave in the barrel region, a ring in the pixel end-cap or a petal in the strip end-cap. The sensitive layers of the ITk are built from these local support structures.

The layout of the detector is shown in Figure 3.1a and covers a pseudorapidity of up to $|\eta| = 4$. Due to a finite efficiency of the detectors and possible detector failures, for example due to radiation damage, the layout is designed to provide 13 hits per track. Therefore, the ITk will consist of five layers of pixel and four double layers of strip modules in the barrel region arranged in cylinders surrounding the beam axis. In the forward region, the strip detector uses six disks while the pixel detector uses rings of sensors corresponding to a layer in the barrel. The simulated amount of hits is shown against the pseudorapidity in Figure 3.1b. The pixel detector is divided into an inner (layers 0 and 1) and an outer (layers 2, 3 and 4) pixel detector to allow the inner layers to be replaced. Figure 3.2 shows a 3D image of the detector layout.

With this design, the ITk will achieve the same track reconstruction efficiency at $\langle\mu\rangle = 200$ as the ID at $\langle\mu\rangle = 20$ at a decreased fake rate. Figure 3.3 illustrates the

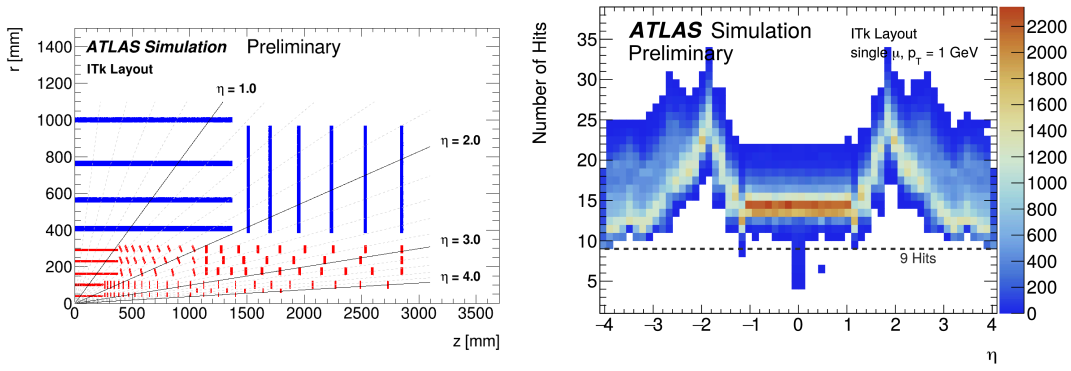

(a) (b)

Figure 3.1.: a) Sensitive layers in one quadrant of the ITk. Layout as of March 2019. b) Simulated number of hits in the strip plus the pixel layers of a track as a function of η. [44]

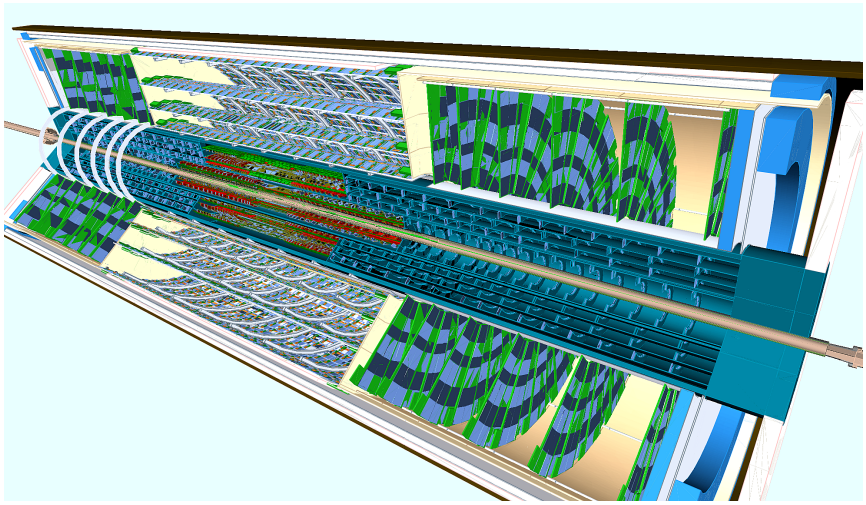

Figure 3.2.: Visualisation of the ITk. [28]

amount of tracks expected during the HL-LHC. The decision to use 5 pixel layers instead of 4, as proposed in the Letter of Intent [29], is based on simulations showing 13 hits to be sufficient to provide robust tracking. With the additional pixel layer, an improved separation of close-by-tracks is achieved, for example in $\tau \to \nu_\tau 3\pi^\pm$ events [28].

In Figure 3.4a, the expected fluence is shown for the ITk for a integrated luminosity of $3000\,\mathrm{fb}^{-1}$ at $\sqrt{s} = 14\,\mathrm{TeV}$. The expected integrated luminosity at the end of HL-LHC has been further increased to $4000\,\mathrm{fb}^{-1}$. Including a safety factor of 1.5, the strip modules are expected to be exposed to a fluence of $1.6 \times 10^{15}\,\mathrm{n_{eq}cm}^{-2}$ at this stage [46]. Due to the extreme fluences, the inner two layers of the pixel detectors are planned to be replaced in a shutdown during HL-LHC operation. The innermost layer of the pixel detector is expected to reach a fluence of $1.31 \times 10^{16}\,\mathrm{n_{eq}cm}^{-2}$ after $2000\,\mathrm{fb}^{-1}$ [43].

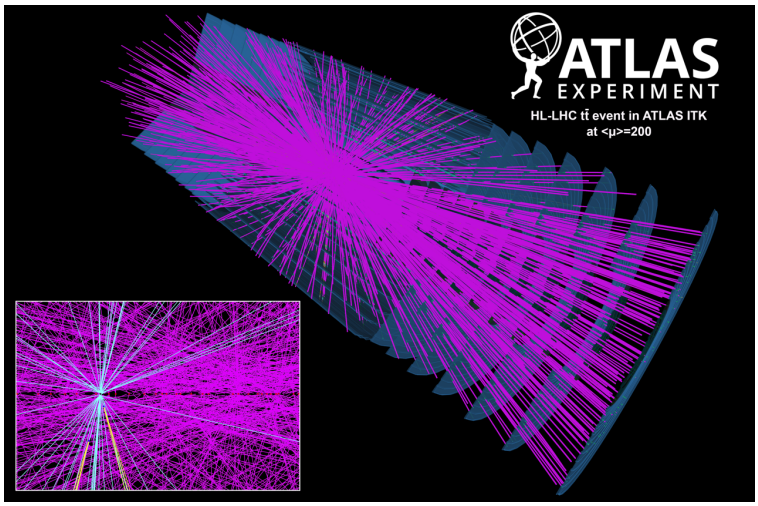

Figure 3.3.: Simulated event with $\langle\mu\rangle = 200$. [45]

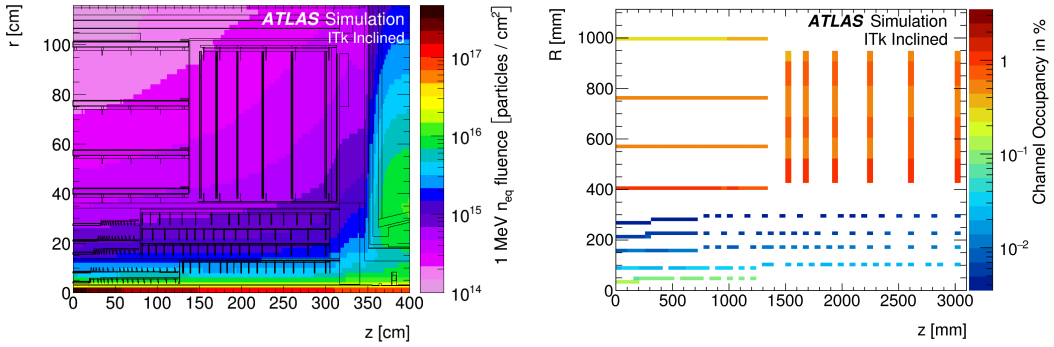

(a) (b)

Figure 3.4.: a) Simulated fluence after $3000\,\mathrm{fb}^{-1}$. b) Simulated occupancy of the read-out channels in the pixel and the strip detector from minimum bias events for $\langle\mu\rangle = 200$. [28]

The increased number of channels in comparison to the ID is motivated by keeping the occupancy low. As shown in Figure 3.4b, the simulated occupancy in most segments is below 1 % at $\langle\mu\rangle = 200$ with a maximum of 1.2 % in the inner modules of the outer strip disks. This ensures robust pattern recognition [28]. Furthermore, the maximum occupancy in an event is kept below 90 % per link to avoid data losses due to bandwidth saturation.

Trigger and DAQ

With the increase in luminosity, the trigger of the ATLAS experiment is upgraded as described in Reference [42]. The new trigger system will use a single stage hardware trigger, the Level 0 (L0) trigger, and the high-level Event Filter (EF). The L0 trigger uses data from the calorimeters and the muon system to reduce the rate from the

40 MHz bunch crossing rate to a 1 MHz trigger rate with a latency of 10 µs. Due to the increased luminosity, the new trigger system uses data with a higher granularity than the old L0 trigger. With its additional coverage in the forward region, the ITk allows to retain low thresholds for the transverse momentum p_T there without an increase in the trigger rate. For the selected events, the detector is fully read out and the data is transfered into a buffer, while the EF makes a decision. The EF uses a processing farm which is aided by the HTT system. The HTT will use ASICs and Field-Programmable Gate Arrays (FPGAs) to provide tracking information from ITk data to the EF. The HTT is designed to provide regional tracking for the full rate of 1 MHz and additionally global tracking at a rate of 100 kHz. Overall, the EF brings the data rate down to 10 kHz, which is then moved to permanent storage.

Since an increase in full read outs is not possible due to the detector design, a L1 hardware trigger is an option if the L0 trigger becomes insufficient due to a higher than expected occupancy or trigger rate. In both cases, the bandwidth would be insufficient to read out the full L0 trigger rate. In this option, the L0 trigger rate would be up to 4 MHz and the L1 Trigger would use regional tracks from the strip and the outer pixel detector to reduce the rate of full detector read outs.

The interface between the detector, the trigger, the EF and permanent storage is the readout subsystem. It is responsible for Detector Control System (DCS) communication as well - for example configuring detector modules and reading out temperature sensors. The Front-End LInk eXchange (FELIX) subsystem receives detector information via point to point links to the subdetectors and is the interface for the data handlers and the DCS system to the detector. In ATLAS, the FELIX system will first be used for the upgrades in LS 2 introduced in Section 1.1.1. It is implemented with servers using custom FPGA-cards

Cooling system

Due to the heat load of 250 kW [28] produced in the ITk, a cooling system is necessary which needs to be able to transport the heat from the modules to a cooling plant with as little use of volume and material as possible. The cooling system will be operated as a two phase cooling system where only a fraction of the coolant evaporates in the detector. This allows to keep temperature differences small throughout the detector. The temperature of the coolant in the detector can be controlled by changing the pressure down to −35 °C. With this design, it is achieved to have minimal hardware in the detectors acceptance and therefore uses only a small material budget.

The system will use CO_2 as coolant due to advantageous physical properties in comparison with other coolants such as C_3F_8 used in the current detector. To reduce the material in the detector, small tubing is preferred. However small tubing has the disadvantage of a high pressure drop in the system. With CO_2, the pressure drop can be reduced by a lower flow rate due to its high latent heat and its low viscosity. Additionally two phase cooling system using CO_2 can be operated at higher pressures reducing the effect of a given pressure drop. Further advantages are its low cost, its radiation hardness and its low environmental impact in comparison to other coolants.

The High-Granularity Timing Detector

The High-Granularity Timing Detector (HGTD) is proposed to get precision timing measurements for tracks in the range of $|\eta| = 2.4$ to $|\eta| = 4$ [47]. While not part of the ITk, it uses the same volume and complements the ITks tracking capabilities. The HGTD reduces the available space in the forward region for the strip end-cap section with regard to the envelope assumed in the Technical Design Report (TDR) [28].

Precision timing will be achieved with the use of Low Gain Avalanche Detectors (LGADs). These sensors are similar to silicon detectors as presented in section 2.6. Close to the read-out on the n-side, a highly doped p-implant is added to the p-type bulk. This highly doped area results in an locally increased electric field. If the field strength is sufficient in this area, an avalanche effect results in an internal gain. Sensors with a thickness of 50 µm or below will be used to achieve a high slew rate, which enables time resolution in the order of 30 ps. The sensors will have pixels with a size of 1.3 mm × 1.3 mm and will be read out via a bump-bonded read-out chip.

The HGTD is used to compensate the lower z_0 resolution in the forward region in comparison to the resolution in the central region of the ITk. As collisions during a bunch crossing are spread out over 175 ps, the 30 ps of the HGTD can effectively reduce pile up in the forward region by a factor of six [47] and help associate tracks with vertices.

3.2. The ATLAS ITk Pixel Detector

The pixel detector is mounted inside of a support tube with an inner radius of 341 mm. Since the two innermost layers are designed to be replaceable, they are mounted in a separate support tube with an inner radius of 145 mm. Furthermore, the outer pixel detector must not rely on the presence of the inner tracker. In case of catastrophic failure during the replacement, the outer tracker must also be able to support the beampipe to operate without the inner pixel layers.

The planned layout of the pixel detector is shown in Figure 3.5. The five layers of the pixel detector can be described as having a central barrel, an outer barrel and an end-cap region. In Table 3.1, the position as well as the used module type are listed for all layers and regions. In the central barrel region, modules are mounted on staves in parallel with the beam axis. In the outer barrel, the staves extend into the outer barrel region. However, these modules are inclined and spaced in z to achieve higher coverage with a reduced surface area. In the end-cap region, individual rings perpendicular to the beam axis are used for each layer. In comparison to disks, rings are positioned in the optimal position for each layer which allows to keep the hit count stable over this interval in pseudorapidity. A further advantage is that supports can be routed between the rings. The inner pixel detector uses staves in the central barrel and rings in the forward region and end-cap. The layer 0 rings in the end-cap are at a higher radius than the barrel rings to cover up to the same pseudorapidity. Modules with a single read-out chip bonded to a sensor will be used in layer 0. The other layers will use quad modules made up of four read-out chips on a single, larger sensor. The layout results in an overall surface area of 12.55 m^2 [43]. The local support structures

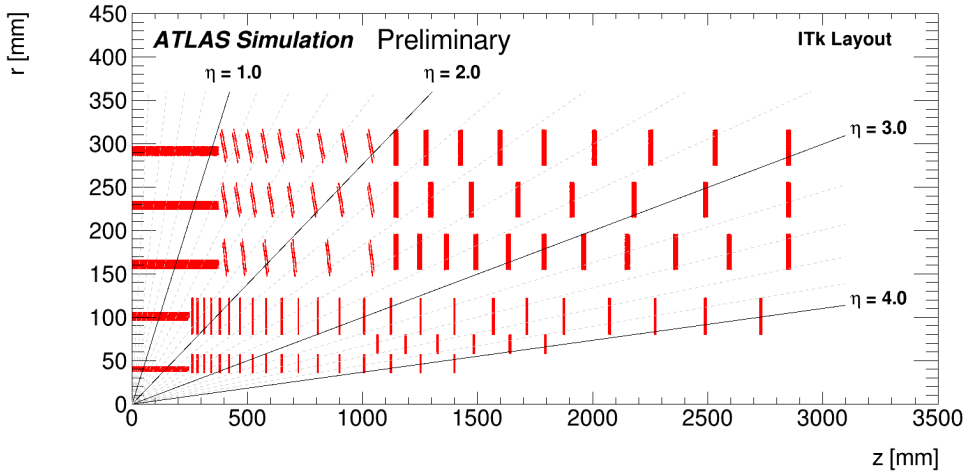

Figure 3.5.: Layout of the ITk Pixel detector. [44]

Table 3.1.: Parameters of the pixel detector. Layout as presented in [44].

	Central Barrel		Outer Barrel		End-cap		
Layer	R [mm]	z [mm]	R [mm]	z [mm]	R [mm]	z [mm]	Module Type
0	39.00	0-245	36.00	261-1400	58.70	1065-1795	single
1	99.00	0-245	80.00	261-1400	80.00	1595-2730	quad
2	160.00	0-372	150.00	372-1047	154.50	1145-2850	quad
3	228.00	0-372	218.00	372-1047	214.55	1145-2850	quad
4	291.00	0-372	281.00	372-1047	274.60	1145-2850	quad

are made of carbon based composites with high stability at a low mass. The design also achieves a good thermal connection between the modules and the titanium tubes inside the structure that are used for the coolant.

Due to the close proximity of the ITk Pixel detector to the interaction point, the radiation hardness is the motivator for most design choices such as sensor technology. At the End of Life (EoL), the sensors must not exceed a leakage current of 10 nA per channel and the available cooling power must be sufficient to avoid thermal runaway. In thermal runaway, the power dissipation of a sensor increases with temperature more than the cooling power with temperature difference to the coolant and the sensor keeps increasing power dissipation and temperature.

The detector uses three different types of passive high resistivity silicon sensors. All of them use a p-doped bulk and are read out on the n-side. For layer 0, 3D-sensors (see Section 2.6) will be used due to their excellent radiation hardness. Since production capacity is limited and 3D processing is expensive, layers 1 to 4 will use planar sensors. In layer 1, sensors with a thickness of 100 µm are used while layers 2 to 4 will use 150 µm, which are easier to produce and handle. A final decision

regarding the pixel being sized 50 µm × 50 µm or 25 µm × 100 µm is yet to be made. It is still under investigation if there are sufficient physics benefits to outweigh the higher complexity and increased noise of a rectangular pixel.

The sensors are connected to read-out chips in a flip chip bump-bonding process. These bare modules are mounted with the sensor side on flexible PCBs which provide the outside connection for the power supply of the read-out chip, the data and the high voltage for sensor biasing. In case of quad modules, the read-out chips are powered in parallel to achieve a common ground level on the sensor. The power consumption of a single chip module is estimated to be 7 W [43]. The module is mounted with the backside of the read-out chips on the support structure which provides cooling.

The final readout chip is not yet available. It will be produced in a 65 nm CMOS process and will have 153600 channels and a size of 19.2 mm × 20 mm. The switch from the 130 nm process used for the IBL read-out chips is necessary to achieve the smaller pixel size. The chip will be based on the RD53-A demonstrator chip developed by the RD53 collaboration [48]. This collaboration is a common research effort between CMS and ATLAS. In comparison to the read-out chip of the current pixel detector, the new chip is targeted to provide a lower threshold of $600\,e^-$ after irradiation. The chip needs to be able to sustain a Total Ionising Dose (TID) of 5 MGy. Furthermore, the chip has to be robust against single event upsets which are for example caused by a radiation induced change of a flip-flop status. This robustness is achieved with redundancy where possible. Additionally, the configuration of the chip will be refreshed regularly.

The pixel detector will use a serial power scheme where multiple modules are powered by a single line. With this, a reduced number of cables and therefore less material is achieved. This also reduces temperature fluctuation with changes in the power consumption of the read-out chip. To implement this scheme, two shunt-low-dropout regulators are used. They are supplied by a constant current source, and each of them provides a constant voltage (analogue and digital voltage of the read-out chip) with the excess current being shunted to module ground. Each module uses the ground potential of the previous module as high potential. Modules can be bypassed in case of failure to avoid failure of the entire chain. High voltage for the sensors is provided with a single line in parallel for the modules in a serial powering chain. Since sensor uses the same ground potential as the read-out chips, the applied bias voltage to the sensors changes for each module in the chain.

Data links with a 5.12 Gbit s^{-1} bandwidth are used for data transmission. With a goal of less than 70 % occupancy of the data links, quad chip modules are connected with up to four data links depending on the occupancy at their location in the detector. One link per single chip module is used in layer 0. A conversion into an optical signal will be performed outside of the ITk. This allows the use of established technology as well as easy access during shutdowns.

3.3. The ATLAS ITk Strip Detector

The ATLAS ITk strip detector is the outer subdetector of the ITk and covers a pseudorapidity up to $|\eta| = 2.5$. It is separated into a barrel section (up to $|z| =$

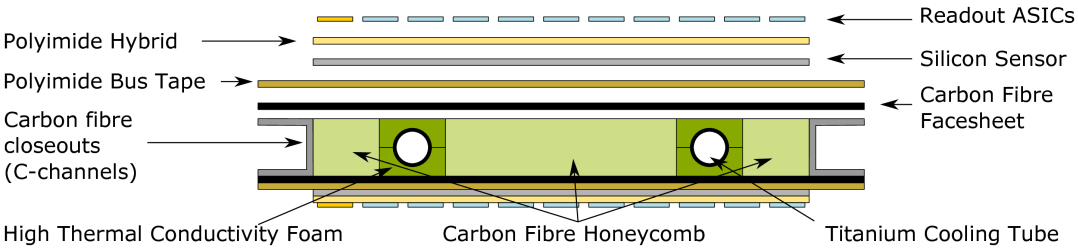

Figure 3.6.: Cross-section of the local support structure. Not to scale. [28]

1400 mm) and an end-cap on each side (up to $|z| = 2850$ mm).

The four layers in the barrel region use modules mounted parallel with the beam axis resulting in four sensitive cylinders around the axis. Each end-cap uses six disks with modules perpendicular to the beam axis. This design results in an overall sensitive area of 165 m^2.

The physics performance targets and simulations of the ITk are discussed in Section 3.4. Apart from performance, the detector design accounts for multiple other constraints. To provide tracking at EoL, the detector is designed to achieve a signal to noise ratio of 10:1 at the final fluence of $1.6 \times 10^{15}\,n_{eq}cm^{-2}$ (including a safety factor of 1.5). Due to the large sensitive area, the design needs to be easy to produce at a low cost. Furthermore, geometric constraints on the available support lines, the material budget and the detector volume had to be taken into account.

3.3.1. Local Support

The local support in the barrel and the end-cap use the same concept as shown in Figure 3.6. This design is able to supply the electric connections and the necessary cooling while being rigid and of light weight. The basis is a carbon fibre honeycomb structure with embedded cooling structure, which consists of a titanium pipe for the coolant in high thermal conductivity foam. On both sides, the honeycomb is covered by a carbon face sheet. The next layer is the bus tape, which provides data and power links between the modules and the End of Substructure card (EoS). The modules are mounted with the sensor side down onto the bus tape. The design allows to test all components before assembly on the local support.

Each end-cap is made of six disks. On both sides of the disks, 16 petals are mounted, which are used as local support in the end-cap. The front and back petals overlap to achieve hermeticity. In Figure 3.7, a petal is shown next to a stave as used in the barrel. Due to the wedge shape, six different modules in six rows are used to cover each side of a petal. The rows are named after their location on the petal R0 (the innermost geometry) to R5 (the outermost geometry). In the outer rows R3 to R5, two sensors are used to cover the increased petal width. The sensors have two to four rows of strips in radial orientation. An angle of 40 mrad between the strips of the sensors on the front and the back of the petal is implemented in the sensor design as discussed in Section 3.3.3. In Table 3.2, the inner radius, the strip length and the average strip pitch are given for each row.

Table 3.2.: Parameters of the ITk end-cap disks. [28]

Ring/Row	**Inner Radius [mm]**	**Strip Length [mm]**	**Strip Pitch [μm]**
Ring 0 Row 0	384.5	19	75.0
Ring 0 Row 1	403.5	24	79.2
Ring 0 Row 2	427.5	29	74.9
Ring 0 Row 3	456.4	32	80.2
Ring 1 Row 0	489.8	18.1	69.9
Ring 1 Row 1	507.9	27.1	72.9
Ring 1 Row 2	535	24.1	75.6
Ring 1 Row 3	559.1	15.1	78.6
Ring 2 Row 0	575.6	30.8	75.7
Ring 2 Row 1	606.4	30.8	79.8
Ring 3 Row 0	638.6	32.2	71.1
Ring 3 Row 1	670.8	26.2	74.3
Ring 3 Row 2	697.1	26.2	77.5
Ring 3 Row 3	723.3	32.2	80.7
Ring 4 Row 0	756.9	54.6	75.0
Ring 4 Row 1	811.5	54.6	80.3
Ring 5 Row 0	867.5	40.2	76.2
Ring 5 Row 1	907.6	60.2	80.5

Table 3.3.: Parameters of the ITk Strip barrel layers. [28]

Layer	**Radius [mm]**	**Channels in ϕ**	**Strip Pitch [μm]**	**Strip Length [mm]**	**Tilt Angle [°]**
0	405	28×1280	75.5	24.1	11.5
1	562	40×1280	75.5	24.1	11.0
2	762	56×1280	75.5	48.2	10.0
3	1000	72×1280	75.5	48.2	10.0

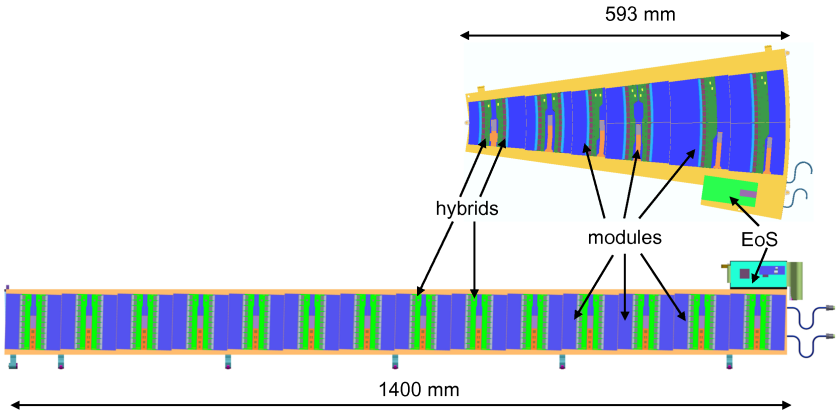

Figure 3.7.: Petal (top) and stave (bottom) used for local support in the ITk Strip detector. [28]

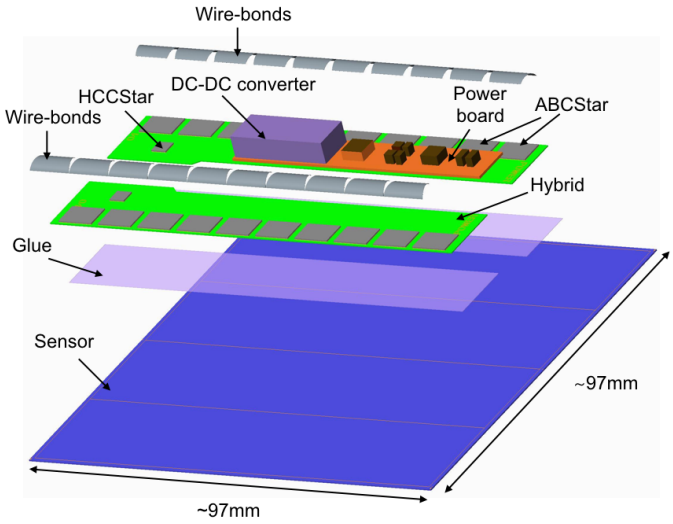

Figure 3.8.: Blow-up drawing of an ITk Strip barrel module. [28]

In the barrel, a total of 392 staves are used to form the four barrel layers. A stave has 14 modules of a single type on each side. Table 3.3 lists the parameters of each layer. The modules on the staves are rotated by 26 mrad to achieve an angle of 52 mrad between the strips on the front and the back of a stave. To achieve hermeticity, the staves are tilted around z.

3.3.2. Modules

A total of 17888 Modules are used as the basic building blocks of the ITk Strip Detector. In the barrel as well as the end-cap, they follow the same basic design which is illustrated in Figure 3.8 for a barrel module. To keep the modules simple and use as little material as possible, Flexible Printed Circuit (FPC)-Hybrids are directly glued onto the sensors with electronics-grade epoxy. The Hybrids are loaded with two types of ASICs: the HCCStar (Hybrid Control Chip) and the ABCStar (Atlas Binary Chip) readout chips. Each ABCStar is connected with wirebonds to 256 strips from two rows. The power for the ASICs, the sensor bias voltage and DCS functionality are provided by the powerboard, which is a FPC as well.

The specific module layout is adapted to the requirements at their location. The strip length varies between inner and outer modules in order to achieve a similar occupancy. A shorter strip length and therefore a lower noise helps modules which are exposed to high fluences to preserve a signal to noise ratio above 10.

In the inner two layers of the barrel, the modules are so-called short strip modules while in the outer layer, long strip modules are used. The short strip module uses four rows of strips along z, the long strip modules use two rows for the same external dimensions. Therefore, the long strip module uses a single hybrid with a row of ten ABCStar chips while the short strip module uses two hybrids with ten ABCStar chips

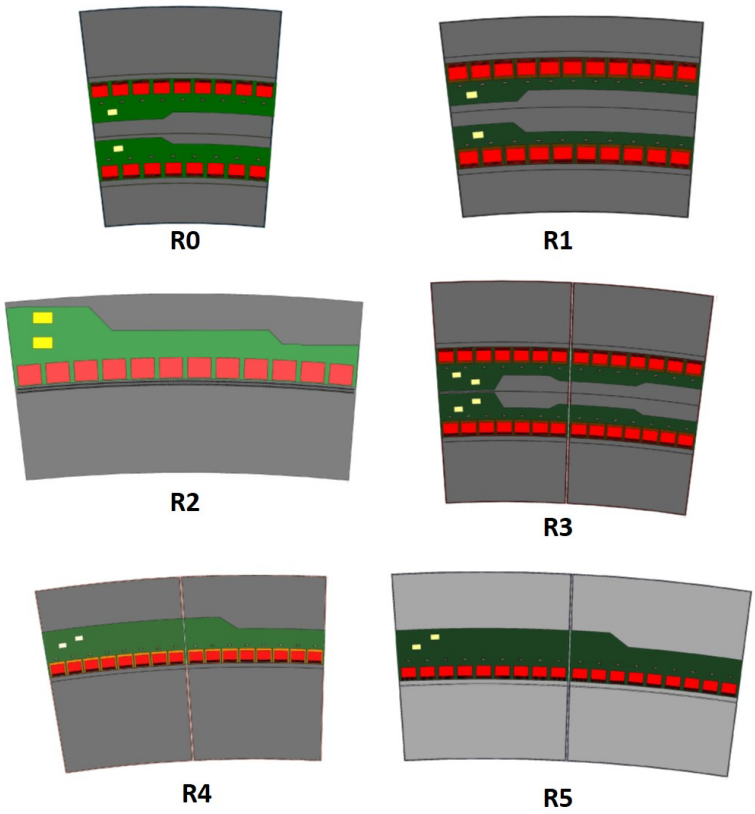

Figure 3.9.: Drawings of the different end-cap modules with sensors in grey, hybrids in green, the HCCs in yellow and the ABCs in red. Powerboards are not shown. [28]

each. Each of these hybrids has one HCCstar. Overall, the barrel consists of 10976 modules.

The end-cap uses 6912 modules of six different module types, which are listed in Table 3.4 and illustrated in Figure 3.9. R3, R4 and R5 are called split modules using two sensors each. For these modules, the hybrids on the first sensor are connected with wirebonds to hybrids on the second sensor. To be able to address all the ABCStars, two HCCStars are used per row of hybrids, which are both located on the hybrid on the left sensor. The powerboard serving both sensors and hybrids is on the right sensor. For production and total module numbers, a split-module is counted as two modules. The R2 module also uses two HCCStars due to the number of ABCStar exceeding the number of input channels of one HCCStar.

3.3.3. Sensors

The sensors are p-bulk devices read out from the n-side. This change in technology in comparison to the SCT was made because the p-bulk sensors can be operated without being fully depleted after substantial irradiation and the improved availability of p-bulk substrate since the production of the SCT.

Table 3.4.: End-cap modules of a petal with strip rows and number of ASICs per row.

Module	#Rows	#Sensors	#ABCStars
R0	0-1	1	8
	2-3		9
R1	0-1	1	10
	2-3		11
R2	0-1	1	12
R3	0-1	2	7
	2-3		7
R4	0-1	2	8
R5	0-1	2	9

All different sensor types are produced on 6-inch wafers with a thickness of 300 µm and are designed to be as large as possible on the wafer. The barrel sensors are nearly square with a size of 96.640 mm × 96.669 mm. The construction of the end-cap sensors is shown in Figure 3.10. The upper and lower edges are on circles around the centre of the beam pipe (point O). To achieve an angle between the strips on the front and the back of the petal, the strips (as well as the left and the right edge of the sensors) are not pointing towards the centre of the beam-pipe but to a point close by (point F). This stereo angle allows both measurements to be combined into a single measurement of a 3D space point. With this design, it is achieved to have similar pitch as the barrel for the bonding pads, a good coverage and a constant strip length in each row for a uniform capacitance of each strip and therefore noise in each channel.

To read out the strip implants in the detector, Aluminium strips with a bonding pad are used which run in parallel to the implants with a passivation layer in between them. Deposited charges in the detector are collected by the implants and induce a signal in the AC-coupled aluminium strips, which is then carried by the wire bonds into the ABCStar chips. The bias voltage is applied via the back side of the sensor. The ground contact is provided by a bias ring surrounding the strips. It is connected to the strip implants via a poly silicon resistor. This design avoids passing the sensor leakage current through the ABCStars. To isolate the strip implants from each other, p-stop implants are used. The sensors will be operated with a bias voltage of up to 500 V.

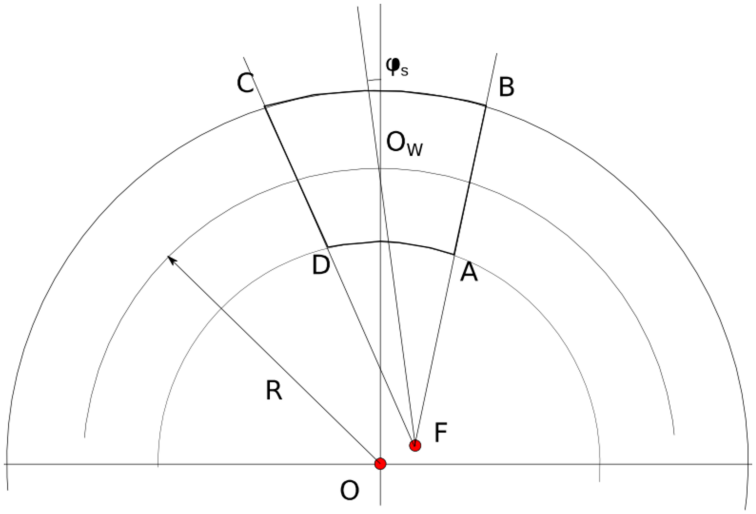

Figure 3.10.: Sketch showing the construction of the shape of end-cap sensors. The circles have their centre in O and determine the inner (DA) and outer (CB) edge of the sensor. The strips are pointing towards F to implement the stereo angle. The left (CD) and right (AB) edge of the sensor are parallel to the strips. [28]

3.3.4. Hybrids

Hybrids are used to read out the sensors and consist of an FPC loaded with passive components and the ABCStar and the HCCStar custom ASICs. The FPC provides a single ground for low noise, data transfer, supply voltages for the ASICs and a Negative Temperature Coefficient thermistor (NTC) to monitor module temperature.

While the prototype chips ABC130 and HCC130 used a serial readout with multiple ABC130s connected in a single link to the HCC130, the final chips will use a star layout where every ABCStar is directly linked to an HCCStar. The change was necessary since originally proposed L0 trigger rate of 500 kHz was increased to 1000 MHz. This made a new set of ASICs necessary and the star architecture was adopted as at most three chips in a chain could be used in high occupancy regions. The star layout has the advantage of being simpler, however the additional connections result in an additional layer in the FPC. A schematic of the star layout is shown in Figure 3.11.

The ASICs are produced in the 130 nm IBM CMOS8RF process, which offers a reduced power consumption, improved radiation hardness and a higher density in comparison to the 250 nm process used for the SCT readout chips. The process uses 8-inch wafers which are thinned down to between 200 µm and 320 µm. This process has the problematic feature of an increased digital current in the TID range from 1 Mrad to 2 Mrad, which was observed during operation of the IBL [49]. The increased leakage current is reversible with further irradiation and is dependent on the dose rate and the temperature. This effect is caused by a build up of positive charges in NMOS transistors which open a parasitic source-drain channel resulting in leakage current. At higher doses, this is compensated by the build up of negative charges. The Star ASICs were designed to minimise this effect. However, it is still

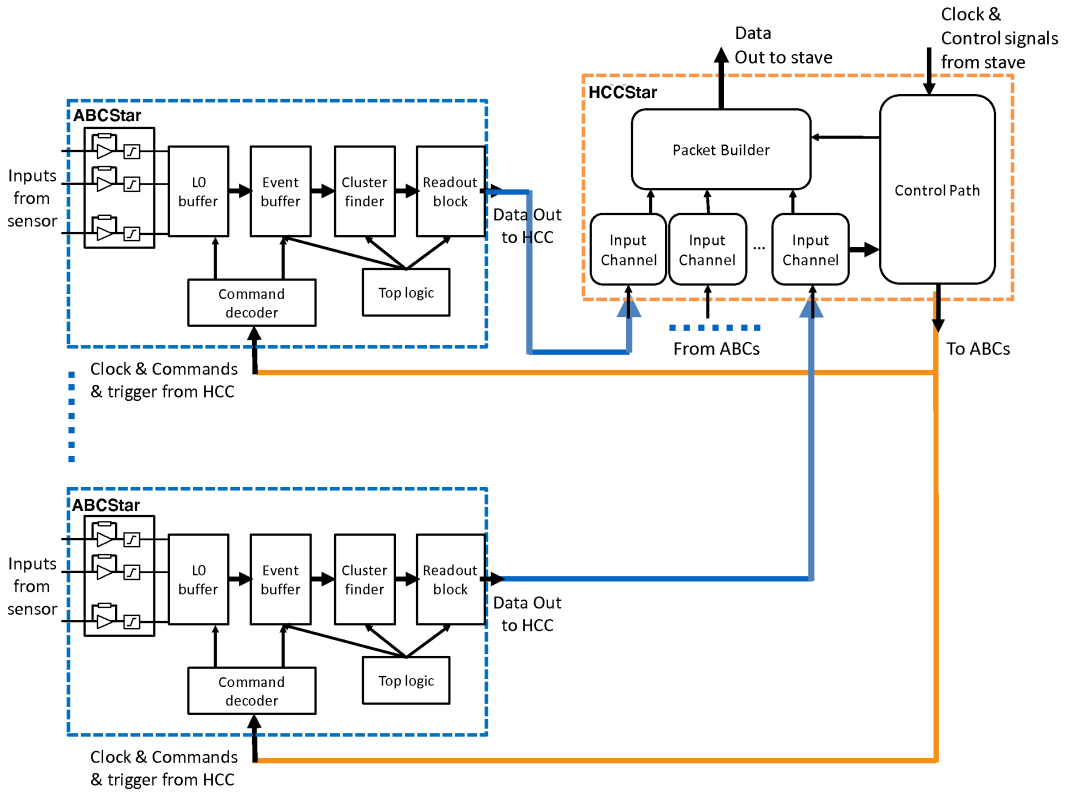

Figure 3.11.: Simplified schematic of a hybrid for the ITk strip modules. [28]

under discussion if the power drain can be limited to a sustainable level by adapting the operation conditions (primarily the detector temperature) or if the ASICs will be irradiated before usage to avoid having this effect in the detector.

When the n-doped strip implant collects a charge after a traversing particle has deposited energy in the sensor, a charge is induced in the aluminium strip which is connected via a wire bond to one of the 256 read out channels of the ABCStar. The charge is then converted into a voltage in a transimpedance amplifier, shaped into a quasi-Gaussian pulse and fed into a differential discriminator. The binary output is then sampled and stored in the L0-buffer. A global threshold in the range of 0 fC to 6.5 fC is set for the discriminator. To compensate threshold dispersion, the threshold can be adjusted for each channel. The channels are calibrated by injecting known charges into the readout channel. In a finished module, a noise level of 1000 e is expected allowing to use a threshold below 1 fC (6242 e). Upon a L0 trigger signal, the corresponding entry is moved from the L0-buffer into the Event Buffer and tagged with a trigger identifier. The next stage is the cluster finder. If the two level hardware trigger option is used, events move to the next stage if either the Level 1 Trigger requires data for regional tracking or if the Level 1 trigger accepts the event. In case of the initial single level hardware trigger layout, no further selection of events is made in the detector. The cluster finder compresses the data by using 12-bit cluster words. It scans through the channels and creates a cluster word for the

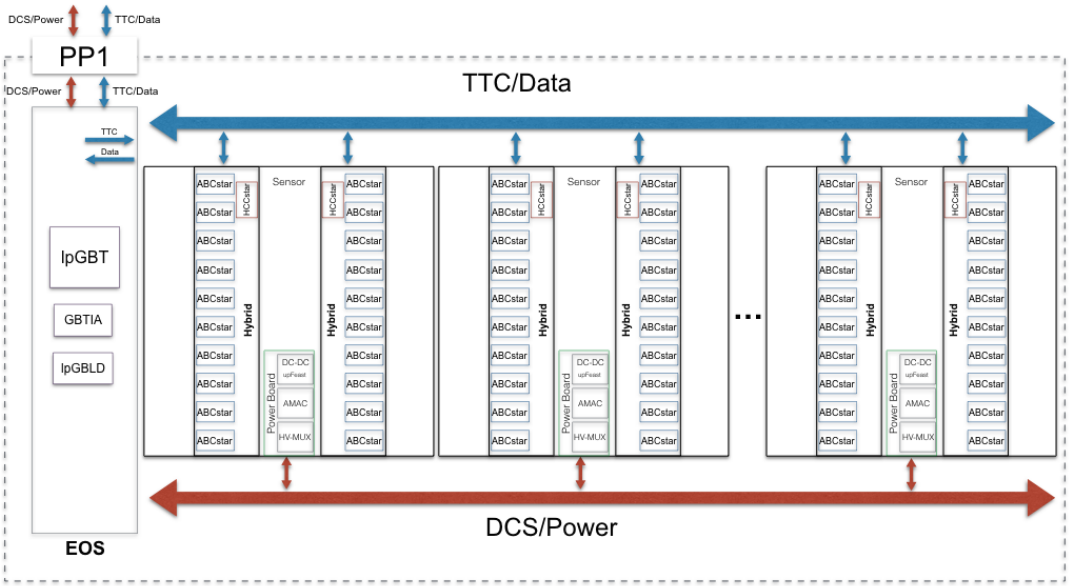

Figure 3.12.: Simplified schematic of the electronics of the ITk Strip Detector. [28]

first hit found. The channel number is stored in the first eight bits. The next three bits are used to specify if a hit has been found in the next three channels and the last bit is used to specify if this is the last cluster in this event. Finally, the readout block builds packets from the incoming hit data and sends them via a 160 Mbit s^{-1} connection to the HCC. The ABCStar is controlled via the command decoder, which receives command, trigger and clock information from the HCC.

The HCCStar serves as interface between the ABCStars and the EoS. It receives trigger, clock and control commands from the EoS and relays them to the ABCStar chips. It has eleven input channels to receive data from one ABCStar each. This data is then built into packets and sent to the EoS via a 640 Mbit link to the EoS. A schematic of the electrical layout of a local support structure is shown in Figure 3.12.

3.3.5. Powerboard

As shown in Figure 3.12, the second active component on a module is the powerboard, which provides high voltage for the sensors, control and monitoring capabilities for the module as well as the low voltage needed for the ASICs. It is an additional FPC directly glued onto the sensor and connected to the hybrids with wire bonds. While the functionality is the same for any module, the geometry of the board is adapted for each module type.

Due to a limited number of lines to supply the detector, four sensors share a single high voltage line. To avoid the failure of multiple modules due to a single defect sensor, an HV Multiplexer is implemented on the powerboard to be able to disconnect sensors individually. The bias voltage is connected from the powerboard to the backside of the sensor via the HV-tab. For the barrel, this is a 11 mm long, 2 mm wide and 17 µm thin piece of aluminium foil protected by a capton cover layer.

One end is welded with a wire bonder to the back of the sensor while the other end is connected to the bus tape from where it is routed to the powerboard.

The Autonomous Monitor and Control Chip (AMAC) ASIC will monitor voltages and currents of the DC-DC converter and the ASICs on the hybrid, the temperatures of the NTCs on the hybrid and near the DC-DC converter and the sensor bias current. It is in control of powering up the hybrid and can power it down independently if the monitored parameters imply a malfunctioning state of the hybrid. The powerboard directly communicates with the EoS via an independent I^2C link and can therefore be addressed independently from the rest of the module. This enables a low power mode where diagnostic measurements can be performed without powering the ASICs on the hybrid. These include measurements of the sensor current to avoid influence from the heat generated in the ASICs and module temperature. In combination, this provides an option for monitoring radiation damage via the increase of current with fluence.

Although the ITk Strip Detector needs less power per channel than the SCT, the number of channels lead to an overall increase in power consumption. To supply this additional power without room for additional cabling, a DC-DC conversion scheme is used to supply the ASIC voltage of 1.5 V. This allows to supply 11 V voltage on the power lines and therefore reduces the ohmic loss. The DC-DC converter module uses a buck converter ASIC [50] and a flat type coil. The final chip, the upFEAST, is under development. Due to its close proximity to the module, electromagnetic shielding is necessary to avoid interference in other parts of the module. This is achieved with a shield box made from copper and aluminium.

3.4. Expected Tracking Performance

A full detector simulation including the ITk is used to determine performance parameters of the ITk and their impact on the measurement of physics processes.

From the simulated data output of the ITk, tracks of charged particles are generated and used for benchmark studies of physics processes. Table 3.5 lists the requirements for tracks during track reconstruction. It is based on the ID track reconstruction, which is presented in [51]. Further details are found in [43].

To generate tracks, the first step is the clustering of the hits in the detector. As the strip detector output does only include hit or no hit information, digital clustering is used which determines the position of the cluster by weighting the strips in the cluster equally. In combination with the module on the backside of the local support structure, a single space point is generated from a double layer. In the pixel detector, digital and analogue clustering can be used. Analogue clustering utilises the charge information in the pixels for a more accurate measurement and the separation of merged clusters.

In the first stage, triplets ('seeds') of space points are formed, which are required to be on a straight line in Rz. Then, seeds are selected based on their p_{T} and track parameters. In the next step, confirmation from a fourth layer is required before the track is propagated to further layers and clusters on the trajectory are attached to the track candidate. Finally, incomplete tracks are removed and clusters shared

Table 3.5.: Requirements to accept a track in the ITk. d_0 and z_0 are the transverse and longitudinal impact parameters. [44]

Requirement	Pseudorapidity Interval		
	$\lvert\eta\rvert < 2.0$	$2.0 \leq \lvert\eta\rvert < 2.6$	$2.6 \leq \lvert\eta\rvert < 4.0$
pixel + strip hits	≥ 9	≥ 8	≥ 7
pixel hits	≥ 1	≥ 1	≥ 1
holes	< 2	< 2	< 2
p_{T} [MeV]	> 900	> 400	> 400
$\lvert d_0\rvert$ [mm]	≤ 2	≤ 2	≤ 10
$\lvert z_0\rvert$[cm]	≤ 20	≤ 20	≤ 20

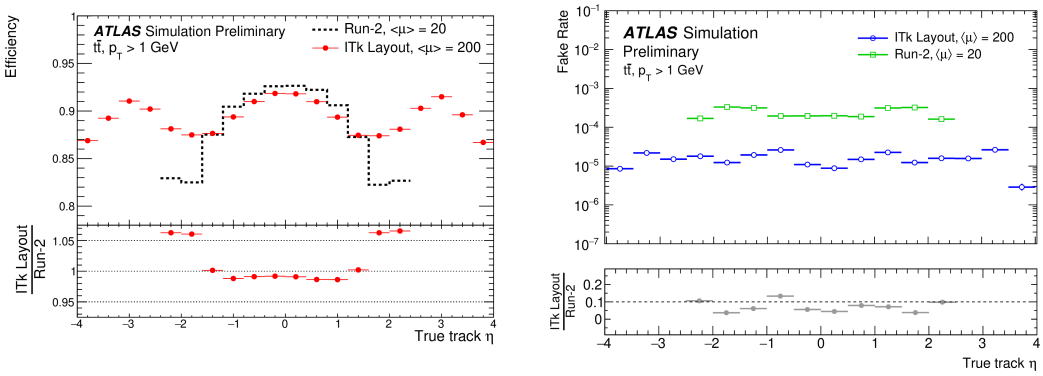

(a) (b)

Figure 3.13.: Simulated track reconstruction efficiency (a) and fake rate (b) of the ITk for $t\bar{t}$ events at $\langle\mu\rangle = 200$ in comparison to the ID at $\langle\mu\rangle = 20$. [44]

between candidates are attributed to a single track based on a scoring. Tracks are then reconstructed from the seeds using an iterative Kalman filter. Starting from the track parameters gained from the seed and their uncertainties, hits on neighbouring layers are estimated. If a hit is found, a weighted average is used to update the track parameters. The candidates matching the criteria listed in Table 3.5 are then included in the list of selected good tracks.

To optimise and compare detector performance, simulations of benchmark processes are used. The plots shown here are cited from [44] and use $t\bar{t}$ events. They are commonly used as benchmark processes as they are the primary decay product of new heavy particles predicted by theories beyond the standard model such as the Z'. In Figure 3.13a, the simulated track reconstruction efficiency of the ITk is plotted against η and compared with the ID. This shows that the goal of a comparable performance to the ID in the central detector region is achieved in regard of the track efficiency, while the fake rate is reduced as shown in Figure 3.13b. This simulation also demonstrates the increased performance and acceptance in the end-cap region.

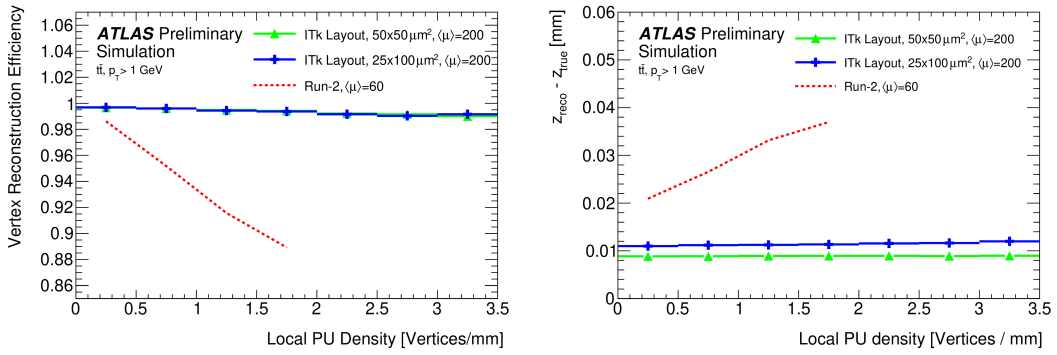

(a) (b)

Figure 3.14.: Vertex reconstruction and longitudinal resolution for the ITk in comparison to the ID. [44]

The resolution of the transverse impact parameter d_0 matches the resolution of the current detector with the exception of p_{T}, where the current detector provides a better resolution due to the inner layer at 33 mm in comparison to the 39 mm of the ITk. The longitudinal impact parameter z_0 is improved due to shorter pixels in the ITk. The p_{T} resolution is improved due to the strip detectors improved granularity with respect to the TRT.

To be able to attribute tracks to the corresponding event, the vertices need to be found and reconstructed correctly. In the simulation of $t\bar{t}$ events shown in 3.14a, the ITk achieves a vertex reconstruction efficiency close to 100% with a significantly improved resolution in z, which is shown in Figure 3.14b.

This shows that ITk is achieving the goal of matching or exceeding the tracking performance of Run 2 in the demanding environment of the HL-LHC.

4. Module Production in Dortmund

The production of the ITk strip detector is split into multiple steps which are distributed among different institutions. In Figure 4.1, major steps in the production of a full stave or petal are shown. In the first step of the module production, sensors, ASICs and Flexible Printed Circuits (FPCs) are received from the vendors and tested at dedicated sites. ASICs and FPCs are then distributed to hybrid building sites. The hybrids assembled there are then sent to a module building site (often the same site as the hybrid building site), which also receive powerboards and sensors. The finished modules are sent to a module loading site were the modules are mounted on local support structures.

In this chapter, the planned production flow in Dortmund for the assembly of hybrids and modules is discussed. The production of the local support structures is not discussed here but can be looked up in [28].

4.1. DAQ

During production, electrical testing of hybrids and modules is essential to identify defects and problems with the production process. For the DAQ system, commercially available FPGA boards with adaptor boards are used with the *ITSDAQ* software[1]. During production, tests are performed to investigate the threshold, the gain and the noise of the readout channels.

These parameters are determined from threshold scans. This scan is performed by injecting a known charge into the readout channel where it is converted into a voltage signal and the response for different threshold levels of the discriminator is measured. From this, a hit rate can be determined for every threshold resulting in an S-curve. The threshold "Vt50" is determined by fitting a skewed error function and taking the voltage with a hit efficiency of 50 %. The output noise σ is defined as the width of the error function. The gain and the input noise can be determined from threshold scans for different charges. The change of Vt50 with the injected charge is called the response curve and the gradient is called the gain. The input noise or Equivalent Noise Charge (ENC) is the charge at the input which creates the same signal level as the noise:

$$\mathrm{ENC} = \frac{\sigma[\mathrm{mV}]}{\text{gain } [\mathrm{mV/fC}]}. \tag{4.1}$$

ITSDAQ Tests

The *ITSDAQ* provides the scans used for the electrical tests of the hybrids and modules. In the first step, the IDs of the ASICs are read out. The **Strobe Delay**

[1] Internal software of the ATLAS ITk collaboration

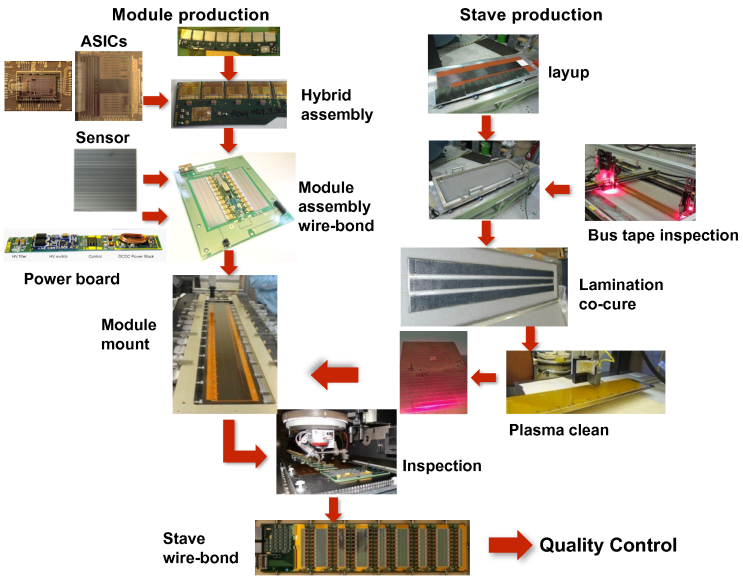

Figure 4.1.: Overview of the production flow for a full stave or petal. In Dortmund, hybrids and modules will be assembled. [28]

scan is used to determine the delay between the command to inject a calibration pulse and and the signal of the measured pulse. A **Three Point Gain** scan performs a threshold scan for three different injected charges. It is used as a quick measurement to determine the gain and the ENC of the readout channels. The **Response Curve** scan is similar to the Three Point Gain but uses 10 points for its measurement. The **Noise Occupancy** scan determines the occupancy of the readout channels due to noise induced hits at multiple thresholds. The **Trim Range** scan performs threshold scans and then adjusts the threshold of each channel to achieve a uniform threshold among the channels.

4.2. Production

The production is organised in clusters. For the end-cap, four clusters are each responsible to produce modules for approximately a quarter of one end-cap. Dortmund is a hybrid assembly and a module assembly site in the cluster funded by the Bundesministerium für Bildung und Forschung (BMBF) and will build 192 R2 and 96 R5 split-modules. As the two sensors of the R5 split-module with their respective hybrids are connected at a late stage, they are considered as two modules during production.

In Figure 4.2, a schematic of the module production flow to be used in Dortmund is shown. For this, production steps which are to be performed immediately after each other are grouped into production blocks. On the left of the schematic, the blocks for the hybrid assembly is shown while the module assembly is on the right. In the following, each of the blocks is briefly summarised while the hybrid gluing block is discussed in detail as an example.

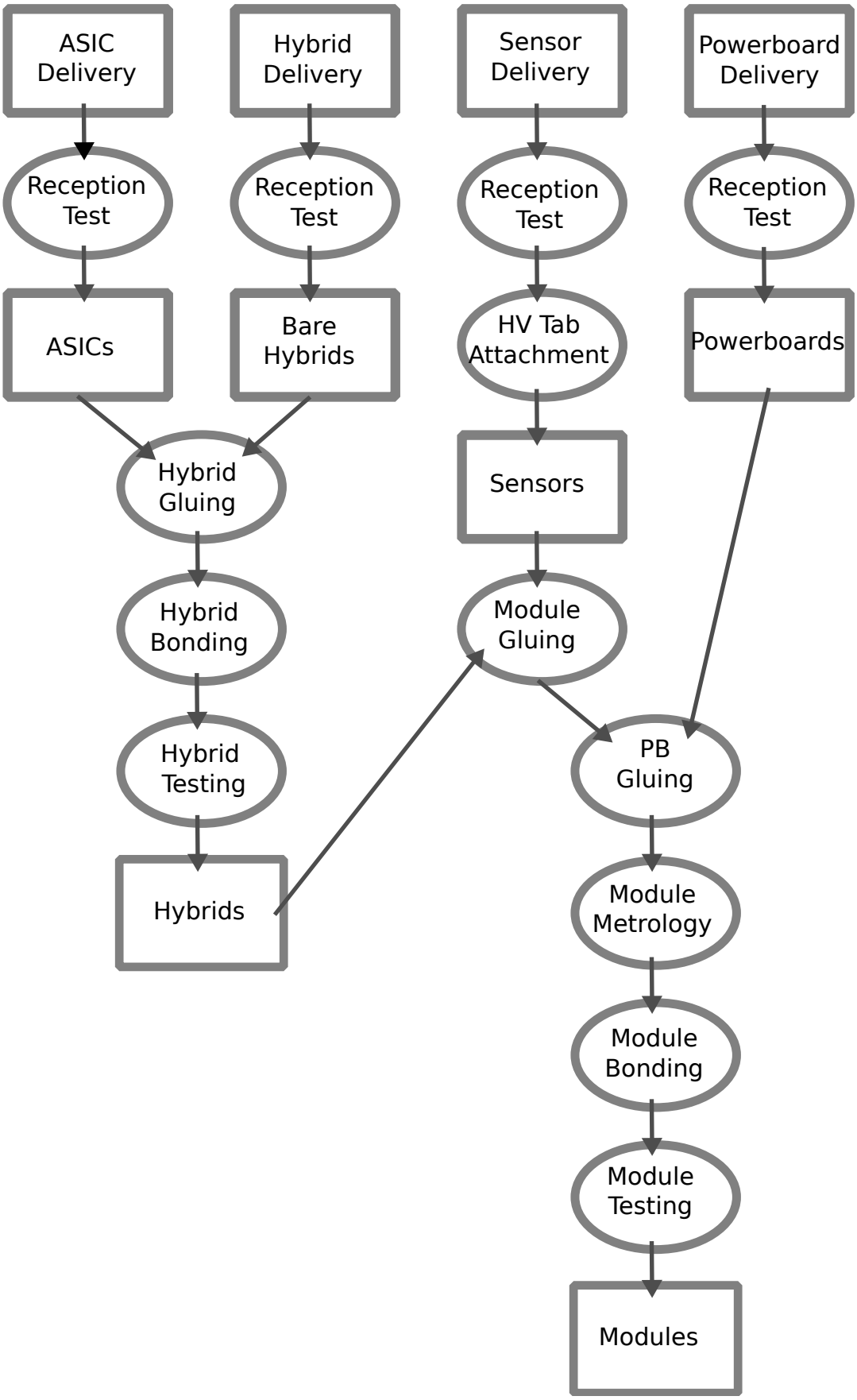

Figure 4.2.: Schematic production flow of modules in Dortmund

Material			Time per Step			Total Time
Hybrids		Total	25	per Session	Gluing setup time	25
2	R2		5	per Hybrid	Additional setup time per hybrid	20
1	R5a		2	per Hybrid	Weighing of hybrids and ASICs	8
1	R5b	4	1	per Hybrid	Upload to the database (weighing)	4
ASICs			10	per Hybrid	ASIC to hybrid gluing	40
6	HCCStar		5	per Hybrid	Metrology	20
42	ABCStar		1	per Hybrid	Upload to the database (metrology)	4
			2	per Hybrid	Weighing of assembled hybrids	8
			1	per Hybrid	Upload to the database (weighing)	4
			1	per Hybrid	Placement of hybrids in the Panel	4

Setups			Time	
Hybrid Gluing	Scale	PC	Estimate	137
Macrosscope	Desk		Rounded up	**150**

Figure 4.3.: The steps of the hybrid gluing block with time estimates in minutes.

Reception and Preparation

For the module production, sensors, hybrids, power boards and ASICs are delivered to Dortmund from other institutes of the ITk collaboration. After they arrive, a reception test is performed to identify damage from the shipment. This includes a visual inspection of the package and the components and an I-V scan for the sensor. Before sensors are used for module building, the HV-tab (described in Section 3.3.5) is attached to the back of the sensor. Afterwards, the components are put into storage.

Hybrid Gluing Block

The hybrid gluing block includes the preparation for gluing, gluing as well as weighing the components. The time estimate for each step, the necessary setups and the overall time are shown in Figure 4.3. This block requires one worker for all steps.

At first, the necessary equipment is prepared. This includes a scale with an accuracy of 0.1 mg, a *Keyence VR-3200* macroscope, the necessary tools and a gluing robot. Then, components are prepared for the gluing step. Hybrids loaded with passive components, which are delivered and stored on flex sheets, are separated from the sheet and weighed before they are placed on the hybrid building jig as shown in 4.4a, where their position is controlled by positioning pins and held in place by vacuum. Afterwards, the ASICs for each hybrid are weighed and put into the chip tray, which has indentations to position the chips accurately.

A glue robot is used to deposit *Loctite 3525*, an UV-cured adhesive, on the hybrid in a five dot pattern on each ASIC pad. Then, a pick-up tool as shown in Figure 4.4b is placed on the chip tray using positioning pins to achieve the necessary precision. Vacuum is used to pick up the ASICs and the tool is placed on the hybrid building jig. With vacuum holding ASICs and hybrids in place, the glue height of (120 ± 40) µm is ensured. The glue is cured by putting bars with 405 nm UV LEDs next to the hybrid for a duration of 120 s, which is shown in Figure 4.5a.

Two Quality Control (QC) steps are performed to ensure that the ASICs are glued according to specification. The first one is metrology which is performed with the macroscope. By projecting light patterns on the hybrid, it generates a 3D image shown in Figure 4.5b. From this image, the coordinates of the corners of the ASICs

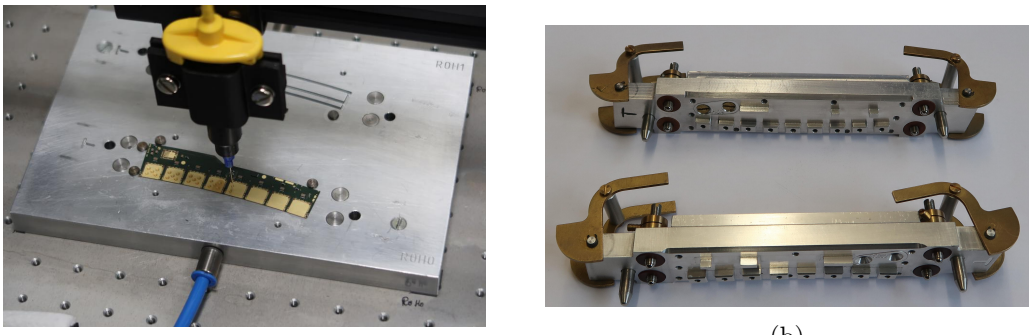

(a) (b)

Figure 4.4.: a) R0 hybrid building jig with placement pins and a R0H0 hybrid while the glue is applied by the gluing robot. b) The pick-up tools for an ABC130 R0H1 (top) and an an ABC130 R0H0 (bottom).

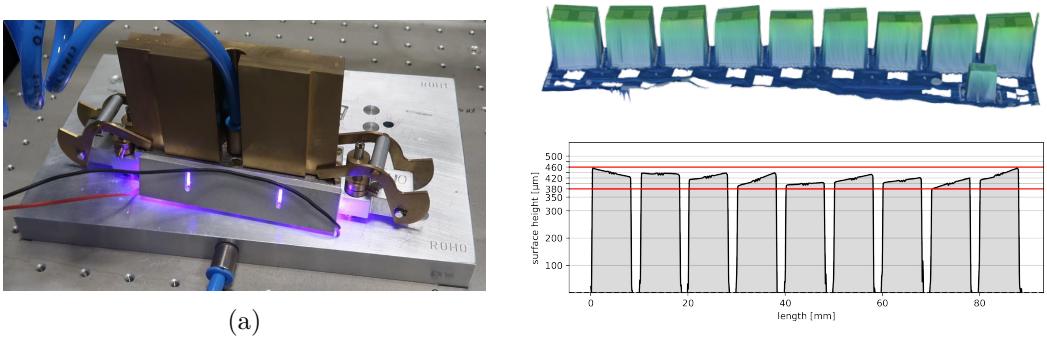

(a) (b)

Figure 4.5.: a) UV-gluing of the ASICs to the Hybrid. The hybrid and the ASICs are held in place by vacuum resulting in a defined glue height. b) 3D metrology plot of a hybrid and a profile showing ASIC height. [52]

are extracted and compared with the coordinates of reference points on the hybrid. To pass the QC tests, ASICs have to be within 100 µm in x and y of their nominal position to ensure the hybrid can be picked up with the pick-up tool for further steps and is compatible with the bonding program of the wirebonder. The glue height can be determined by subtracting the ASIC thickness from the difference in z between ASIC surface and Hybrid surface. The second one is determining the amount of glue used by weighing the assembled hybrid and comparing the weight with the weight of the components. This serves the purpose to monitor the amount of glue used by measuring the weight of the components before and after the gluing step. The goal is the use of 3 mg per ABC and 1.2 mg per HCC to ensure a glue coverage from 40 % to 90 % of the ASIC.

Finally, the hybrids are placed in in a hybrid panel, a Printed Circuit Board (PCB) which enables to read out hybrids after bonding.

Hybrid Bonding and Testing

In the next block, a wire bonder is used to connect the ASICs to the hybrid and the hybrid to the panel followed by a visual inspection and electrical testing to catch any defective bonds. Then, a burn in test is performed where hybrids are operated at 40 °C for 100 h as a stress test to ensure component reliability. Afterwards, hybrids are ready for module building.

Module Building and Testing

In the first block of module building, the hybrids are removed from the panel and are glued onto the sensor in a similar process as used in hybrid building. Two component epoxy glue *Polaris PF-7006* which requires overnight curing is used instead of UV-Glue because the latter does not cure fully as UV cure does not reach all of the glue due to the large hybrid area. The next block consists of gluing the powerboard onto the sensor applying the same process.

In the metrology block, the macroscope is utilised to verify the glue heights and positions of the FPCs and determine the sensor bow. This is necessary to ensure compatibility in further production steps and that envelopes of other components of the final detector are not violated. Afterwards, modules are put into a testframe, a PCB used for bonding and electrical testing.

This is followed by the bonding block. First, the powerboard is connected to the hybrids of the modules, which in turn are bonded to the testframe. Then, the ABCStar ASICs are bonded to the sensor. Each of them has four rows which are bonded to two rows of strips on the sensor. After the first row is bonded, a three point gain scan is performed which is sensitive to the increased noise due to the connected strip and therefore detecting failed bonds.

The final block is module testing, where the module is thermocycled in ten cycles from 40 °C to −35 °C while being powered. This is used to reduce the early life failure rate of finished modules. Electrical tests are performed to verify the module is inside of specification. For example, up to 2 % bad channels are deemed acceptable. A channel is bad, when it is dead (does not respond or has no connection to the sensor), noisy (more than 1.5 times the expected noise level) or cannot be trimmed. Afterwards, the module is ready to be shipped to a petal assembly site.

Production Rates

A production time of 2.75 years is scheduled for modules of the ITk Strip end-cap. Dortmund will build a quarter of the R2 and an eighth of the R5 modules resulting in 192 of each type. Assuming 40 productions weeks per year and half the production rate in the first year, 90 weeks are available. After taking yield estimates into account, this results in 2.34 R2 and 2.42 R5 modules to be built per week.

It is currently planned to built up to three batches of four modules each in two weeks to achieve the necessary rate. This is compatible with current estimates of time needed per production block. These estimates are to be verified in a test week, where the flow of production is simulated by building prototype modules according based on the work flow presented in this chapter.

5. Leakage Current Measurements of Irradiated Silicon Diodes

For the operation of silicon sensors in high radiation environments, the leakage current is an important factor. Radiation damage causes the leakage current to increase and changes the doping concentration resulting in larger voltages needed to deplete the sensor. Thus, power dissipation increases with radiation damage. If the cooling power is insufficient to handle this increase, the sensor keeps warming up which causes an even higher leakage current leading to a thermal runaway. Additionally, an increase of leakage current leads to an increase in noise. The increase of leakage current with radiation can also be used to monitor the radiation damage and the sensor temperature. Both of these applications require to scale leakage current with temperature.

For these reasons, the leakage current of highly irradiated silicon diodes is studied here with a focus on the scaling behaviour with temperature.

5.1. Radiation Damage and Annealing

The radiation damage in silicon is caused by the interactions of traversing particles with silicon. These interactions can be grouped into ionising and non-ionising processes. Damage caused by the first group primarily affects surfaces and interfaces and thus the behaviour of transistors while the second group causes damage to the crystal lattice. As silicon sensors do not have logic elements such as transistors, this section focuses on radiation damage caused by non-ionising processes.

The assumption that the effects in a silicon bulk caused by radiation can be described by the Non-Ionising Energy Loss (NIEL) is called the NIEL hypothesis [53]. This allows the normalisation of radiation damage caused by different radiation types and energies to the damage created by an equivalent fluence Φ_{eq} of 1 MeV neutrons. This is based on the assumption, that the observed effects of irradiation are proportional to the number of point and cluster defects of the lattice. The displacement damage cross-section D, which is proportional to the NIEL [53], is shown for different particle types as a function of their energy in Figure 5.1. The difference in D is caused by the different kinematic parameters (particle mass and momentum) as well as the difference in the Ionising Energy Loss (IEL) due to the charge of the particles. A given fluence Φ is converted with

$$\Phi_{\mathrm{eq}} = \kappa\Phi \tag{5.1}$$

into the equivalent fluence. The hardness factor κ is specific for each irradiation source, which can either be calculated via the displacement damage cross-section

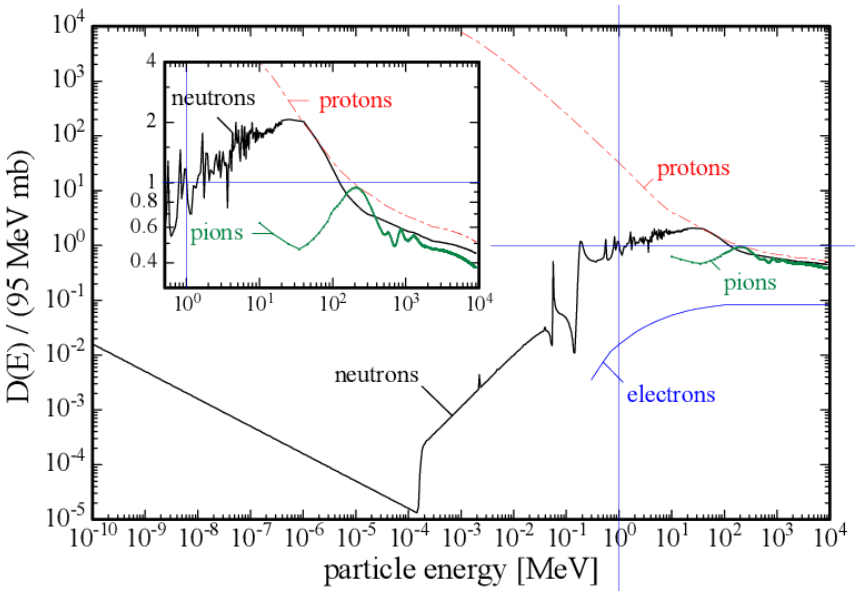

Figure 5.1.: The displacement damage cross-section in silicon by different particle types and energies. Damage from 1 MeV neutrons, which is used for normalising, is highlighted. The inset shows an expansion of the energy range above 1 MeV. [53]

or determined experimentally via the change in leakage current after irradiation. This results in the equivalent fluence $n_{\mathrm{eq}}\mathrm{cm}^{-2}$, which is used to quantify radiation damage. The NIEL can either cause phonon exitation, which has no permanent effect, or damage to the crystal lattice which changes the properties of the device.

In the following Sections, the microscopic defects and the change in the macroscopic behaviour of silicon devices are discussed.

5.1.1. Microscopic Radiation Damage

On the microscopic scale, radiation damage causes different types of defects which introduce new energy levels including primary point defects and cluster defects. They can be studied by their reaction to external stimulation. One method to study the defects is Deep-Level Transient Spectroscopy (DLTS) [55]. For this method, a voltage pulse is applied to a partially depleted silicon device filling or emptying traps in the silicon bulk and the capacitance transients are measured. This is done at different temperatures of the device, thereby allowing access to a wide range of energy levels.

In Figure 5.2, different defect types are shown in the silicon lattice. Common primary point defects are vacancies in the crystal lattice and atoms (silicon or impurity atoms) located in between the lattice structure called interstitials. A Frenkel defect is a complex of an interstitial and a vacancy. These defects are unstable and can move through the lattice. This can lead to a recombination of a vacancy with an interstitial or the formation of more complex defect structures, for example a vacancy next to an impurity atom. An E-center is a vacancy next to a phosphorus atom, typically used as n-dopant, and an A-center is a vacancy next to an oxygen atom. The formation of

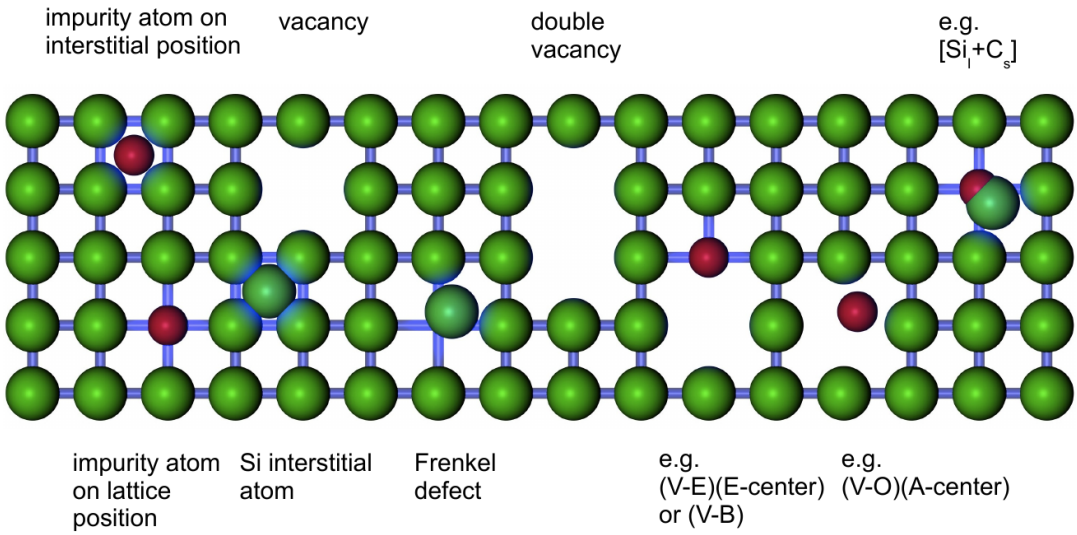

Figure 5.2.: Radiation induced defects in a silicon lattice. [54]

an E-center is called donor removal as it prevents the phosphorus to act as a donor. The A-center is a deep level acceptor which can trap electrons, thereby reducing the charge collection efficiency.

As the energy necessary to remove a silicon atom from a lattice is three orders of magnitude below the typical maximum collision energy of incoming particles [31], such a Primary Knock-on Atom (PKA) can cause cascading damage. In this process, a large cluster of defects is caused instead of isolated point defects. The development of a model based on microscopic defects able to describe the quantitative changes in macroscopic behaviour is an ongoing field of research.

5.1.2. Macroscopic Radiation Damage

The microscopic defects in the bulk greatly affect the behaviour of silicon sensors which can be described with an effective theory known as the Hamburg model [53, 56]. This model also describes annealing: at higher temperatures, defects become unstable and can disappear or combine into more stable complexes.

These macroscopic defects and their annealing are discussed in the following Sections.

Leakage Current

Radiation damage increases the number of mid gap energy levels, which, as described in Section 2.4, increases the leakage current. The increase ΔI, which is shown in Figure 5.3a, can be described as a function of the equivalent fluence by

$$\Delta I\left(\Phi_{\mathrm{eq}}\right) = \alpha \Phi_{\mathrm{eq}} V \tag{5.2}$$

with the damage rate α and the depleted volume V. The damage rate α is independent of the irradiation type and fluence and therefore the leakage current can be used

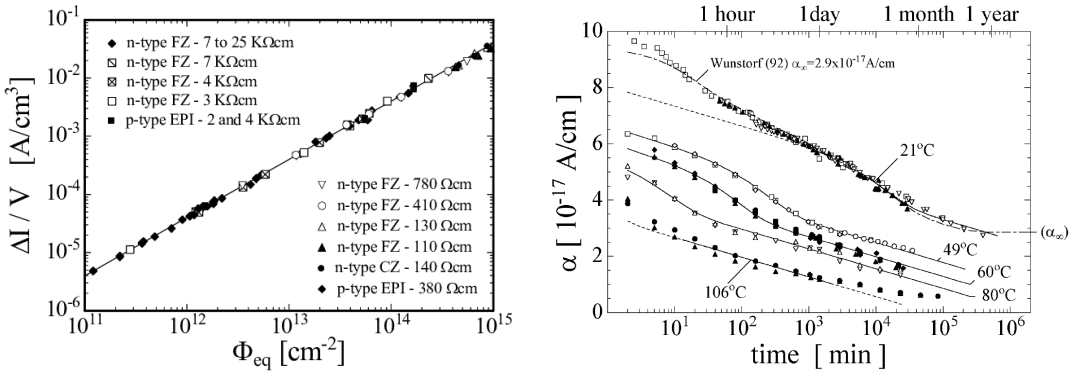

(a) (b)

Figure 5.3.: a) Change of the leakage current with fluence [53] b) Change of α with annealing for temperatures from 21 °C to 106 °C. [56]

to determine unknown fluences. However, since the leakage current is temperature dependent, α is usually defined at 20 °C. As measurements at this temperature are not feasible for highly irradiated silicon devices, measurements at lower temperatures are scaled to 20 °C. The leakage current is also affected by annealing. To minimise the influence of annealing during the irradiation and while handling the sample, it is a convention established by the RD48 collaboration, that the leakage current after 80 min of annealing at 60 °C is used to determine the fluence. Under these conditions, the damage rate is $\alpha_{80/60}$ =4.0 × 10^{-17} A cm^{-1} [53]. To determine α, the depleted volume needs to be known. For fluences up to 1×10^{15} n_{eq}cm^{-2}, α is typically measured after full depletion and the depletion width is equal to the device thickness. However, highly irradiated devices are not fully depleted at typical operation voltages of up to 1000 V.

The change of α with annealing has been extensively studied in [56] and is shown in Figure 5.3b. Over the investigated range of temperature and annealing, the leakage current is continuously decreasing. For an annealing temperature T_A, it can be described by

$$\alpha(t) = \alpha_I \exp\left(\frac{-t}{\tau_I}\right) + \alpha_0 - \beta \ln\left(\frac{t}{t_0}\right) \tag{5.3}$$

for α in the range from 1×10^{-17} A cm^{-1} to 6×10^{-17} A cm^{-1}. The exponential term describes the short term annealing with the amplitude α_I, the annealing duration t and the time constant τ_I which is given by

$$\frac{1}{\tau_I} = k_{0I} \exp\left(\frac{E_I}{k_B T_A}\right). \tag{5.4}$$

In [56], the experimental results for the parameters are

$$\alpha_I = (1.23 \pm 0.06) \times 10^{-17}\,\text{A cm}^{-1}, \tag{5.5}$$

$$k_{0I} = 1.2^{+5.3}_{-1.0} \times 10^{13}\,\text{s}^{-1} \text{ and} \tag{5.6}$$

$$E_I = (1.11 \pm 0.05)\,\text{eV}. \tag{5.7}$$

Equation 5.4 is an Arrhenius relation with the activation energy E_I and the frequency factor k_{0I}. According to [56], this mechanism is likely caused by a single defect as k_{0I} is compatible with the most abundant phonon frequency $\frac{k_B T}{h}$.

The logarithmic term describes the long term annealing effects on the leakage current and is not based on a physical model. With t_0 set to 1 min, the following parameters were determined experimentally in [56]:

$$\alpha_0 = -(8.9 \pm 1.3) \times 10^{-17}\,\mathrm{A\ cm^{-1}} + (4.6 \pm 0.4) \times 10^{-14}\,\mathrm{AK\ cm^{-1}} \times \frac{1}{T_A} \text{ and} \quad (5.8)$$

$$\beta = (3.07 \pm 0.18) \times 10^{-18}\,\mathrm{A\ cm^{-1}}. \quad (5.9)$$

Effective Doping Concentration

With the introduction of new defects into the silicon bulk, the effective doping concentration $N_{\mathrm{eff}} = N_D - N_A$ changes. This happens through the removal of dopants and the introduction of defects acting as donors or acceptors. When E-centers are created, the phosphorus atom cannot act as donor any more. Similar defects are formed with boron atoms, which are used for p-doping. However, they are unstable and therefore do not contribute to the change in N_{eff}. As newly introduced defects are predominantly acceptors, this results in a decrease in N_{eff} with fluence [57]. In Figure 5.4a, this is shown for a sensor with an n-type bulk. With the removal of donors and introduction of acceptors, the bulk type inverts into a p-type with a linear increase in $|N_{\mathrm{eff}}|$ afterwards. This results in a steady increase in depletion voltage with fluence after type inversion. For devices with a high resistivity, type inversion occurs in the fluence range from $1 \times 10^{12}\,\mathrm{n_{eq}cm^{-2}}$ to $1 \times 10^{13}\,\mathrm{n_{eq}cm^{-2}}$ [31]. Sensors with a p-type bulk do not show type inversion.

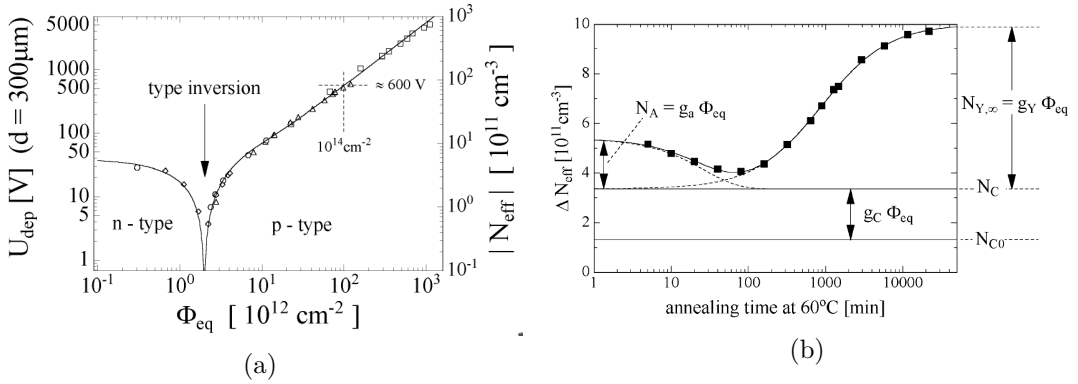

Figure 5.4.: a) Change of $|N_{\mathrm{eff}}|$ with fluence [57] b) Change of ΔN_{eff} with annealing. [56]

In figure 5.4b, the annealing of the radiation induced ΔN_{eff} is shown at 60 °C. The change can be described as

$$\Delta N_{\mathrm{eff}}(\Phi_{\mathrm{eq}}, t(T_a)) = N_A(\Phi_{\mathrm{eq}}, t(T_a)) + N_C(\Phi_{\mathrm{eq}}) + N_Y(\Phi_{\mathrm{eq}}, t(T_a)). \quad (5.10)$$

N_A is a short term component in which N_{eff} is increasing. For a sensor with a p-type bulk, this results in a decrease in depletion voltage and N_A is therefore also known

as beneficial annealing. This mechanism is attributed to the removal of acceptors. However, the generation of donors with annealing could also cause this effect.

N_C describes the constant component which is unaffected by annealing. The incomplete removal of donors and the introduction of acceptor-like defects contribute to this term.

For long term annealing, N_Y becomes relevant which is also called reverse annealing as it leads to an increase in $|N_{\text{eff}}|$ and is caused by a further build-up of acceptors. A more detailed discussion of these terms can be found in [56].

Temperature Scaling of Leakage Current in Irradiated Sensors

The scaling of leakage current with temperature presented in Section 2.4.1 is based on the assumption of a silicon bulk with a depletion region growing from one side while the rest of the bulk is an undepleted and electrically inactive region without an electrical field and called the Electrically Neutral Bulk (ENB). Therefore, it can be assumed that the current is generated in the depleted volume according to the process described there.

Studies of irradiated sensors with Edge-TCT [1] [58] and charge collection efficiency [59] measurements have shown, these assumptions are not fulfilled for highly irradiated diodes. Instead of a bulk separated into an undepleted and a depleted region, regions with a high electric field grow from both sides (known as "double junction" effect) of the bulk while a small electric field is present in the region in between which is sometimes referred to as active ENB. Due to this, the scaling behaviour of the leakage current in these sensors is an active field of research.

A review of available measurements was done in [36]. It showed that the scaling behaviour of irradiated sensors with fluences up to $1 \times 10^{15}\,\mathrm{n_{eq}cm^{-2}}$ is compatible with the expected value of $E_{\text{eff}} \approx 1.21\,\text{eV}$ for bias voltages above depletion voltage. For a sample irradiated up to $1 \times 10^{16}\,\mathrm{n_{eq}cm^{-2}}$, depletion voltage was not reached and E_{eff} was measured to be smaller than the expected value but increasing with voltage. The author proposed, that this is due to the contribution of charge carriers from the active ENB to the bulk current. A temperature dependence of the fraction of charge carriers generated in the active ENB being pulled out and contributing to the bulk current could cause a change in the $I(T)$ behaviour and affect E_{eff}. Further studies of E_{eff} for highly irradiated sensors were conducted in [60, 61]. In those studies, E_{eff} was averaged over the entire voltage range of the current-voltage characteristics used to determine E_{eff} as no change with bias voltage was observed. For sensors irradiated beyond $5 \times 10^{15}\,\mathrm{n_{eq}cm^{-2}}$, E_{eff} was measured to be below the expected value and decreasing with fluence. A difference between [36] and [60, 61] lies in how the sensors were contacted: the first used a contact to a guard ring and a contact to the bulk to separate the bulk current from the surface current. This was not done in the other studies.

Further investigation of this could help in detector operation. As shown in [62], the leakage current is used to measure the radiation damage to the sensors in tracking

[1] Transient Current Technique (TCT) uses a laser to deposit charge at a known position in the sensor. Edge-TCT injects the laser through the edge of the sensor for precise studies of the electric field throughout the bulk.

Table 5.1.: Investigated samples with their respective fluences and annealing times at 60 °C.

Sample	Vendor part number	Fluence[2] $[10^{15} n_{\mathrm{eq}} \mathrm{cm}^{-2}]$	Fluence uncertainty %	Annealing range [min]
P1	5431-08-17	0.6	±7	1170 to 6000
P3	6141-07-17	0.7	±7.7	0 to 6000
P4	6140-01-16	3	±7	0 to 6000
P5	6142-03-16	1	±7.2	0 to 6000

detectors such as the ID of the ATLAS experiment. To use Equation 5.2, the leakage current needs to be known at 20 °C. Because irradiated sensors cannot be operated at such a high temperature due to the high power dissipation, the leakage current needs to be scaled from typical operation temperatures below 0 °C and thereby requiring precise knowledge of the scaling behaviour. For the development of new tracking detectors, the comparison of the leakage current of prototypes and the prediction of power dissipation in the detector environment based on prototype measurements also requires temperature scaling. Prototypes are irradiated to and investigated at the maximum fluences predicted at their respective location where they are typically operated without being fully depleted. Therefore it is necessary to gain understanding about the scaling behaviour before depletion.

5.2. Samples and Irradiation

For this study, four diodes listed in Table 5.1 were used. To investigate the changes in leakage current with temperature and annealing, current voltage characteristics of the samples were measured while these parameters were varied. A diode is shown in Figure 5.5a. They have a p^+-implant of 3 mm × 3 mm on their front side which is surrounded by 16 guard rings and an n^+ implant on their back. Therefore, they are known as guard ring diodes. The diodes have an n-type bulk and a thickness of 250 µm. They use Diffusion Oxygenated Float Zone (DOFZ) material, which is chosen for its improved radiation hardness. The design of the diode allows to contact the innermost guard ring, which can be seen in the schematic design shown in Figure 5.5b. This allows to separate surface currents from the signal measured through the contact on the central implant and therefore, the diodes are well suited for studies of the bulk behaviour. The diodes were produced on wafers for the pixel sensors of the ATLAS ID.

The samples were irradiated in 2009 [63] at the CERN Proton Irradiation Facility (IRRAD) [64]. IRRAD uses 24 GeV/c protons from the CERN PS. Their equivalent fluences as listed in Table 5.1 are determined with a hardness factor of 0.51 [56]. During this campaign, the cooling system failed. Due to this, the diodes were exposed to an unknown temperature and their annealing status is not well known. Additionally, these diodes were used in previous studies and therefore exposed to annealing while handling, in case of P1 also involving controlled annealing. In Table 5.1, the inves-

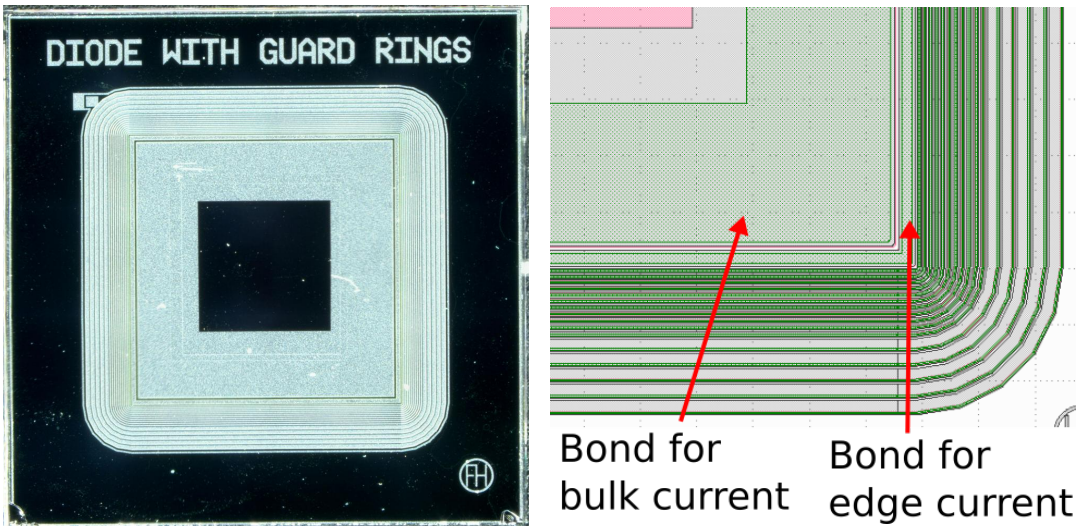

(a) (b)

Figure 5.5.: a) Picture of the p-side of a guard ring diode. b) Schematic layout of a guard ring diode. The innermost ring around the central p-implant is used to separate the edge current from the bulk current. [4]

tigated ranges of annealing at 60 °C are listed. The numbers given are the first and the last step where data was obtained. They do not include uncontrolled annealing. The samples were selected from the diodes of this irradiation campaign to investigate the fluence region, where E_{eff} begins to deviate from the expected value in literature as presented in Chapter 5.1.2.

For this study, the samples were glued, as shown in Figure 5.6, with the n-side down onto *LilP* PCBs [65] using *Dow Corning SSE4445*, a gel with high thermal conductivity. This PCB has four pads for wirebonds. Two of them (marked '1') are used for wirebonds to the remaining metalization of the dicing street, thereby establishing an electric connection to the backside of the diode. The pads marked with '2' and '3' are connected to the metalization on the central p^+ implant and the innermost guard ring respectively. A thermistor is placed on the PCB marked with '4' and its temperature measurement is used as estimate of the diode temperature.

5.3. Setup

The measurements are performed inside a climate chamber able to reach temperatures as low as −40 °C. The samples are placed as shown in Figure 5.7. In addition to the thermistor on the PCB, further thermistors are spread throughout the chamber to observe the behaviour of the setup. All thermistors are read out using a *Keithley K2000* multimeter. To avoid condensation, the volume is flushed with dry air as the climate chamber cannot regulate humidity below 0 °C.

A schematic of the electrical connections is shown in Figure 5.8. A *Keithley K2410* sourcemeter is used to supply the high voltage to the n-side and measure the to-

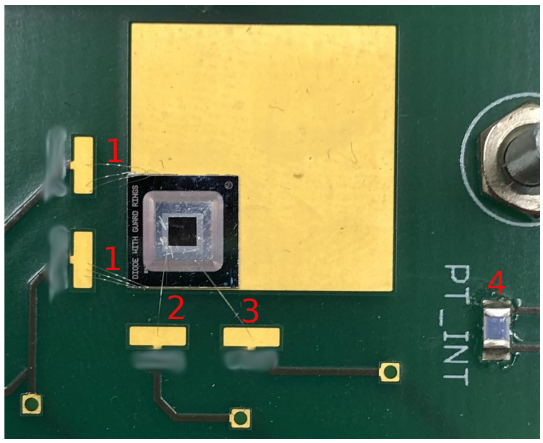

Figure 5.6.: Sample glued on a PCB, including bonds to connect the n-side (1), the central p-implant (2), and the innermost guard-ring (3). The thermistor (4) is visible in the lower right corner. [4]

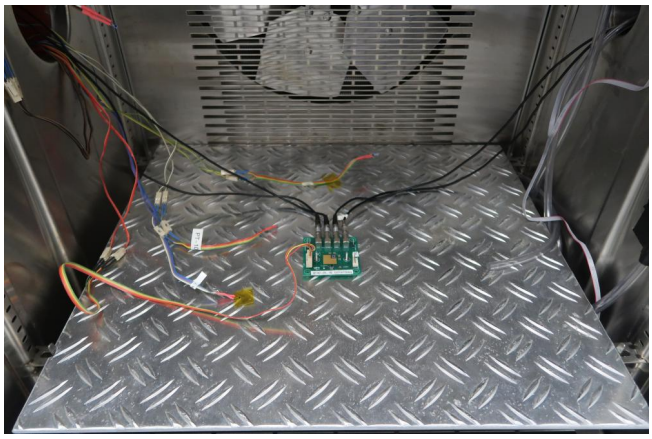

Figure 5.7.: PCB in the climate chamber setup with cabling, thermistors and dry-air tubing.

tal current I_t. On the p-side, the current from the innermost guard-ring is directly returned to the sourcemeter while the current I_b through the central implant is measured by a *Keithley K196* multimeter before being returned. When charge carriers are created inside of the bulk, they drift towards the electrodes. Depending on their location and the electric field inside of the bulk, holes can drift to either the central implant or the guard ring. Thus, I_b is only part of the overall bulk current while the current through the contacted guard ring is comprised of the surface current as well as the rest of the bulk current. The devices are controlled with the software *E4control*[3] enabling remote and automated data taking.

[3] `https://github.com/sdungs/E4control`

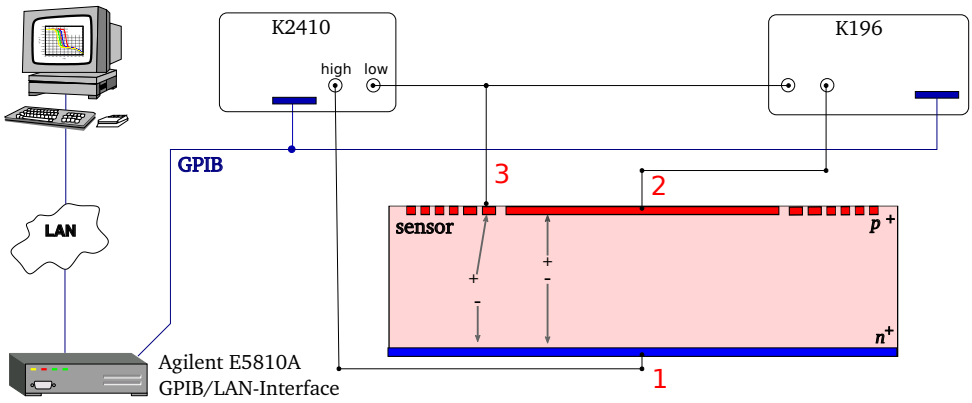

Figure 5.8.: Schematic of the measuring setup. The connection to the n-side (1), the central p-implant (2), and the innermost guard-ring (3) are highlighted.

5.4. Measurements of the Current-Voltage Characteristics

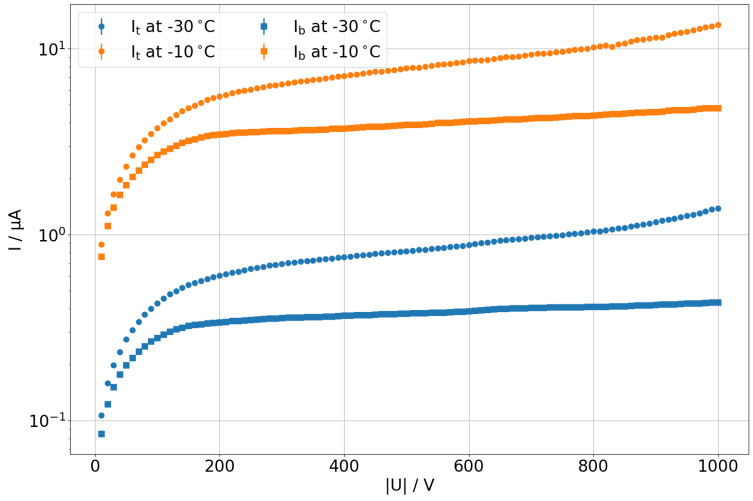

Figure 5.9.: Current-voltage characteristics of the sample P3 at −10 °C and −30 °C before annealing. The total current is shown as well as the bulk current.[4]

During the measurements, a temperature range from 0 °C to −36 °C is used and I-V scans are performed in 2 K steps. Each I-V scan measures the bulk as well as the total current from 0 V to 1000 V while the temperature is monitored unless a current limit of 50 mA is reached, in which case the scan is stopped. These scans are performed in 10 V steps. At each voltage, the current is measured ten times in quick succession after an initial waiting period of 10 s.

In figure 5.9, the I-V characteristics of sample P3 are measured at −10 °C and −30 °C for both the bulk current I_b and the total current I_t. As expected, the current is higher for the higher temperature and a plateau region is visible starting at 200 V.

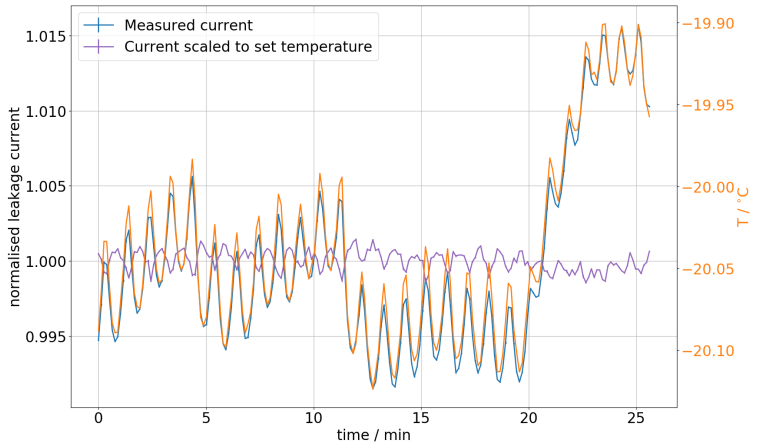

Figure 5.10.: Change of the leakage current over time of sample P3 at 400 V and −20 °C before annealing. Shown are the measured leakage current, the measured temperature on the PCB and the current scaled to −20 °C.

Comparing the bulk with the total current, it can be seen that the separation of the bulk current from the surface current is effective as the plateau region above 200 V is much more pronounced for the bulk current.

To investigate the uncertainty of the current measurements, long term measurements of P3 are performed before annealing. For each of the temperatures of the I-V characteristics, the current was measured over a longer period for multiple voltages. After an initial waiting period, 200 current values are determined with five seconds in between them. Each value is the average of ten measurements in a row. The measurement at −20 °C and 400 V is presented in Figure 5.10. The relative deviation from the mean against time is shown for the current as measured as well as for the current scaled to −20 °C to correct for the measured changes of temperature, which are shown as well. The measured leakage current as well as the measured temperature is cyclical. Therefore, it is assumed that the deviations of the current are caused by the slight thermal cycles of the climate chamber while being set to a constant temperature. However, those deviations can still be seen after correcting for the measured temperature but are phase shifted by 180°. Beginning from the 20th minute of the measurement, the measured current increases as well as the temperature. As the corrected current is not affected as heavily by this change in temperature as from the cycles, the hypothesis was developed, that the thermistor is more responsive to rapid fluctuations in temperature than the diode. Under this assumption, the temperature fluctuations of the diode are smaller than those of the thermistor and thus resulting in the cycles being inverted after scaling the current.

As the I-V scans used in this study only use ten measurements in quick succession at a given temperature and voltage, it cannot be determined at which stage of the cycle the measurement is taken. Since the effect from the cycle is larger than the standard deviation of these measurements, the uncertainty is estimated from the long term measurement. The values averaged over ten single measurements have a standard deviation of about 1 ‰ which is assumed as uncertainty of the current.

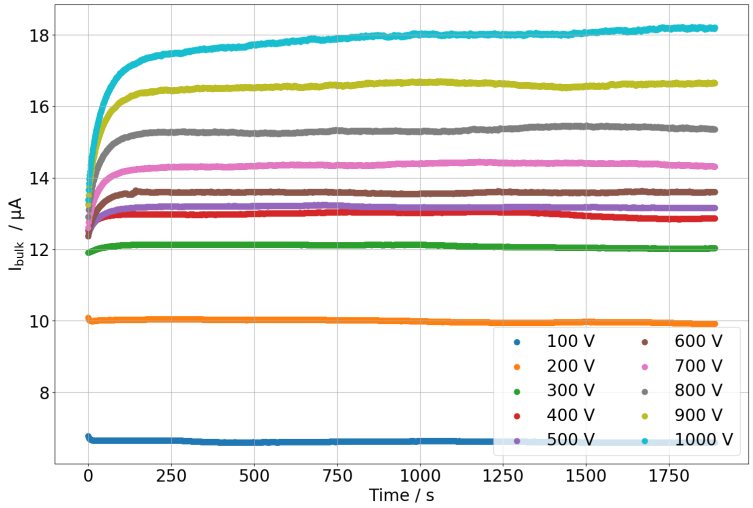

Figure 5.11.: Bulk current over time of the sample P5 after increasing the voltage from 0 V to target voltages from 100 V to 1000 V with the largest possible slew rate slew rate.

5.4.1. Power Limit

To investigate the scaling behaviour of leakage current with temperature, knowledge of the diode temperature is paramount. Due to power dissipation, the temperature of the diode increases above ambient and therefore above the measurement of the thermistor. Due to this, it is studied how much power dissipation is tolerable before this effect known as self heating becomes significant. As the thermistor is not useful to measure this effect, the bulk current is used to study self heating.

For this, the increase of current over time, and thereby the increase of temperature, after applying voltage is studied. The sample P5 is used for this study. It is kept at a constant temperature and 0 V before the voltage is increased with the maximum possible slew rate. Then, the bulk current is monitored for 30 min. For a temperature of 0 °C and voltages from 100 V to 1000 V, this is shown in Figure 5.11. The current stays constant after turn on for voltages up to 400 V. While the initial current is similar for all voltages above 400 V, the current increases over time at higher voltages. This is assumed to be self heating caused by the higher power dissipation.

To be able to determine a power limit were self heating becomes significant, this increase is quantified by the normalised slope in the first 30 s, which is determined by a linear fit. In Figure 5.12, the slope of measurements at 0 °C and −10 °C is shown against the total diode power which is determined from the maximum total current during the measurement and the applied voltage. In this study, a slope above $1‰ \cdot s^{-1}$ is interpreted as a sign of significant self heating. Therefore, a power limit of 5 mW is used to exclude measurements for the study of the scaling behaviour.

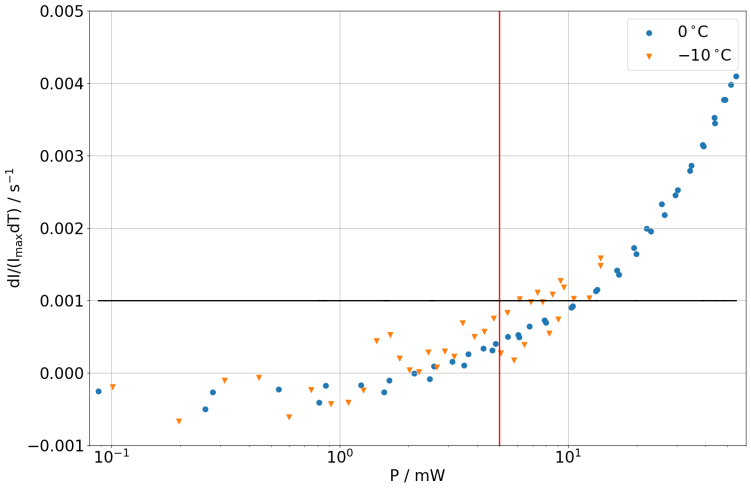

Figure 5.12.: Normalised slope of the current in the first 30 s after a target voltage was reached. The power limit at 5 mW and an increase of $1‰ \cdot s^{-1}$ are highlighted. [4]

5.5. Temperature Scaling of Leakage Current

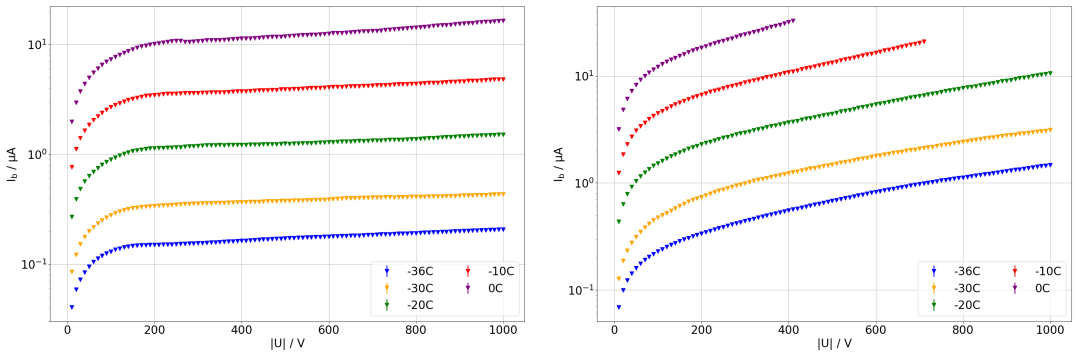

(a) (b)

Figure 5.13.: Bulk current for sample a) P3 and b) P4 for multiple temperatures.

The data taken describes the behaviour of the bulk and total current for the four samples under the variation of temperature, annealing and voltage which allows to thoroughly study how their leakage current scales with temperature and if Equation 2.16 is applicable. In Figures 5.13a and 5.13b, the scaling behaviour of the bulk current is shown for samples P3 and P4 respectively before annealing over voltage. In case of P4, the current limit was reached and the measurements were aborted before reaching 1000 V. For both samples, the scaling behaviour is as expected from Equation 2.16 with the current increasing by roughly a factor of three with an increase of 10 °C. Therefore, the equation is assumed to be applicable and E_{eff} is determined to investigate the observed decrease in E_{eff} with fluence in irradiated samples. To inves-

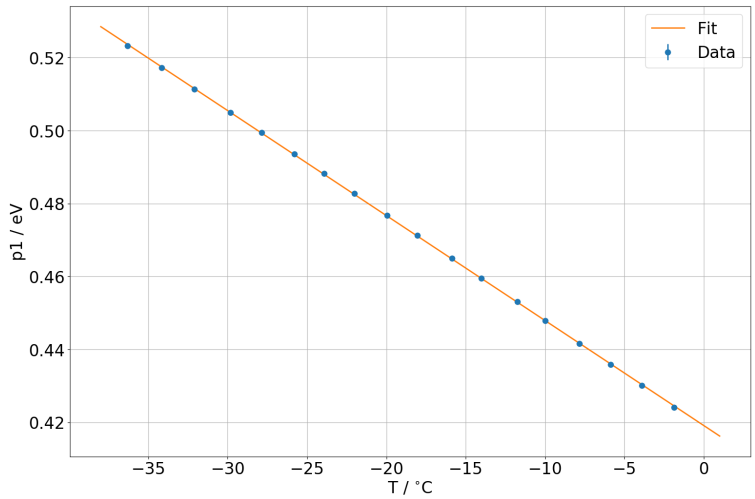

Figure 5.14.: Linear fit to the measured values of $p1(T)$ of the sample P3 before annealing at 250 V.

tigate if the hypothesis of an influence of an active ENB is valid, E_{eff} is determined as a function of voltage to study it before and after the samples are assumed to be fully depleted.

5.5.1. Determining the Effective Energy as Function of the Voltage

To determine E_{eff} from I-V characteristics, the Proportionality 2.16 is used. This is done via a method described in [66]. In this method, a proportionality factor A is introduced, which is dependent on the device characteristics, including its size and its bulk material, and the applied bias voltage:

$$I(T) = AT^2 \exp\left(-\frac{E_{\text{eff}}}{2kT}\right). \tag{5.11}$$

Then the equation is rearranged to isolate the unknown parameters E_{eff} and A on the right resulting in

$$\frac{I(T)}{T^2} = A \exp\left(-\frac{E_{\text{eff}}}{2kT}\right). \tag{5.12}$$

Next, the logarithm of Equation 5.12 is taken,

$$\ln\left(\frac{I(T)}{T^2}\right) = \ln(A) - \frac{E_{\text{eff}}}{2kT}, \tag{5.13}$$

and the equation is rearranged into

$$-2kT \ln\left(\frac{I(T)}{T^2}\right) = E_{\text{eff}} - 2kT \ln(A). \tag{5.14}$$

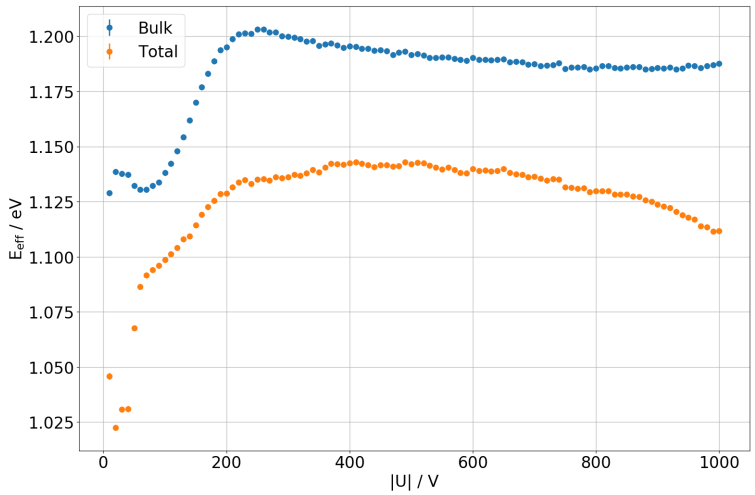

Figure 5.15.: E_{eff} against voltage for the sample P3 before annealing in the temperature interval from $-30\,°\text{C}$ to $-20\,°\text{C}$ for the bulk and the total current.

Now, the data from I-V measurements at different temperatures can be represented using the left side of equation 5.15. Then, a first degree polynomial $p1(T)$ is fitted to the data:

$$-2kT\ln\left(\frac{I(T)}{T^2}\right) := p1(T) = B + 2CkT, \tag{5.15}$$

where B, the value of $p1(0\,\text{K})$, can be identified as E_{eff} and C is $-\ln(A)$.

This is done in Figure 5.14, where the bulk current measured at $-36\,°\text{C}$ to $-2\,°\text{C}$ of sample P3 at a voltage of $250\,\text{V}$ is used. For this method, accurate temperature readings are needed. Therefore, E_{eff} is not determined for voltages, where a data point to be used for the fit is outside of the power limit which implies self heating.

If this is done for all voltages, E_{eff} can be plotted against the voltage as shown in Figure 5.15 for data taken at temperatures from $-30\,°\text{C}$ to $-20\,°\text{C}$. In this figure, E_{eff} determined from the bulk current I_b as well as from the total current I_t is shown. Both measurements clearly deviate from each other as using the total current results in a significantly lower value of E_{eff}. This due to the fact that I_t does not meet the assumption of current being solely generated in the bulk but also includes the surface current. As A contains the information about the device geometry and therefore the volume of bulk where current is generated, E_{eff} can be determined from I_b which is only part of the total generation current.

E_{eff} against voltage determined from I_b shows a clear dependency on voltage: at low voltages, E_{eff} is significantly below the expected value of $1.21\,\text{eV}$ and keeps rising until a value in the order of the expected value is reached and the observed E_{eff} only changes slightly afterwards resulting in a plateau region. Comparing E_{eff} in Figure 5.15 with the bulk current in Figure 5.13a, it can be seen that the plateau region of the I-V characteristic starts at the same voltage as a value of E_{eff} close to the expected value is reached. As the start of the plateau region of the leakage current is commonly associated with reaching full depletion, this is compatible with the hypothesis of [36] that other contributions, for example from an active ENB, to current

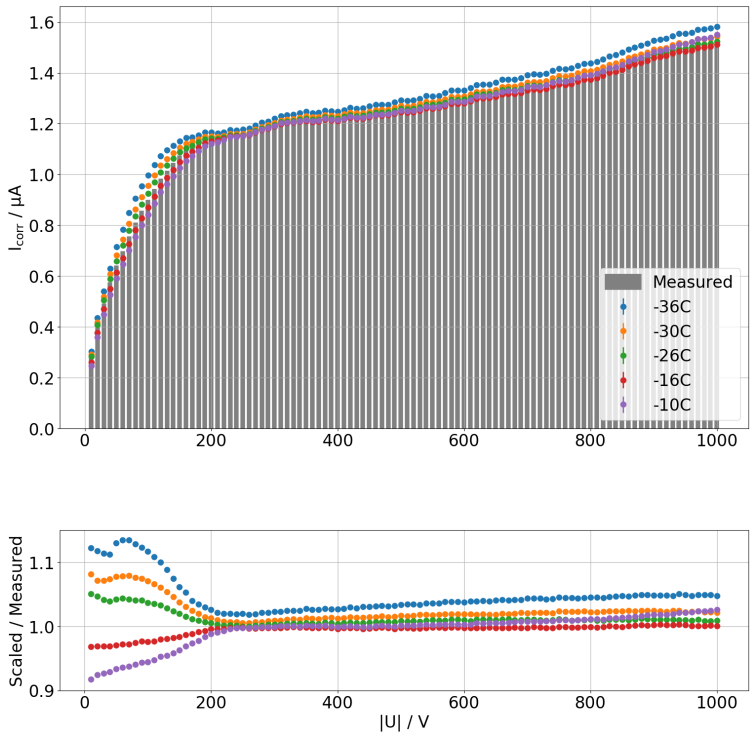

Figure 5.16.: Bulk current of the sample P3 before annealing measured at −36 °C to −10 °C scaled to −20 °C using $E_{\text{eff}} = 1.21\,\text{eV}$ in comparison to the current measured at −20 °C.

generation change the scaling behaviour before depletion. This behaviour is much less pronounced if E_{eff} is determined from I_t, which could be an explanation why no voltage dependence was found in [61]. For further investigations, I_b is used.

In Figure 5.16, the error from scaling current while using the literature value of $E_{\text{eff}} = 1.21\,\text{eV}$ is shown for the sample P3 before annealing. For this, currents measured from −36 °C to −10 °C were scaled to −20 °C and are compared with the current measured at this temperature. At the starting and the end temperature, the measured temperatures are used for each voltage. Looking at the ratio between the current scaled to −20 °C using $E_{\text{eff}} = 1.21\,\text{eV}$ and the measured current at that temperature, the largest deviations appear as expected at low voltages. Also, it can be seen that scaling over larger temperature intervals leads to larger errors of scaled current.

5.5.2. Influence of the Temperature Interval used to Determine E_{eff}

During this investigation, a dependence of E_{eff} on the temperature is observed. To investigate this, E_{eff} is determined for multiple 10 K temperature intervals. The size of 10 K was chosen to minimise the temperature range while maintaining enough data points for the fit. In Figure 5.17, this is shown for the sample P3. The values of E_{eff} measured from the temperature intervals deviate in the range of ±2% in the

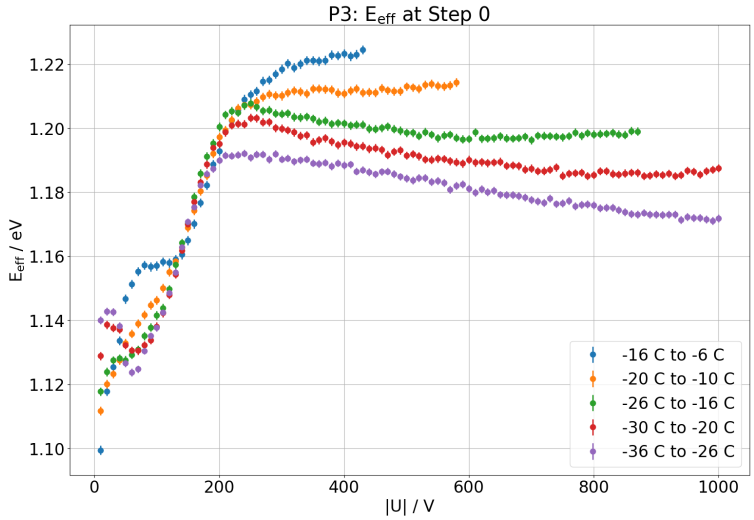

Figure 5.17.: E_{eff} for different temperature intervals for P3 before annealing. [4]

plateau region while being on a similar level before the plateau. In Figure 5.18, the residuals of the fits at 150 V and 400 V are shown in a temperature range from −36 °C to −6 °C. For the first voltage, the residuals are compatible with a random distribution around zero and show no temperature dependence while a dependence on voltage is visible for the second voltage as expected from Figure 5.17.

The origin of this effect, which was also observed in [36], is currently unknown. Self heating is excluded as a possible reason as self heating is a dependent on the power dissipation while this effect has no observed correlation with power as seen with the simultaneous onset of this effect in Figure 5.17. To reduce the impact of this effect, E_{eff} determined in the temperature interval between −30 °C to −20 °C will be used in further investigations unless stated otherwise.

In the Appendix A.1, plots similar to Figure 5.17 can be found for all samples at different stages of annealing.

5.6. Influence of Fluence on Leakage Current Scaling

Figure 5.19 shows the bulk current for all diodes in the study at −30 °C after 1170 min of annealing at 60 °C. As expected, the samples with the lowest fluence, P1 and P3, show the lowest leakage current while P4 with the highest fluence has the highest current. P4 is the only sample for which the current does not saturate, implying that full depletion is not achieved.

As the leakage current changes with fluence, the scaling behaviour is affected as well. As shown in Section 5.5, the scaling parameter E_{eff} increases until the sample is assumed to be fully depleted and E_{eff} is close to the literature value of E_{eff}. This is shown for all the used samples in Figure 5.20 before annealing.

P3 and P5 show similar behaviour of E_{eff} as a function of voltage at this stage of annealing as sample P3 before annealing in Section 5.5: E_{eff} close to 1.10 eV at 10 V and increasing towards a plateau afterwards. P4 with the highest fluence does

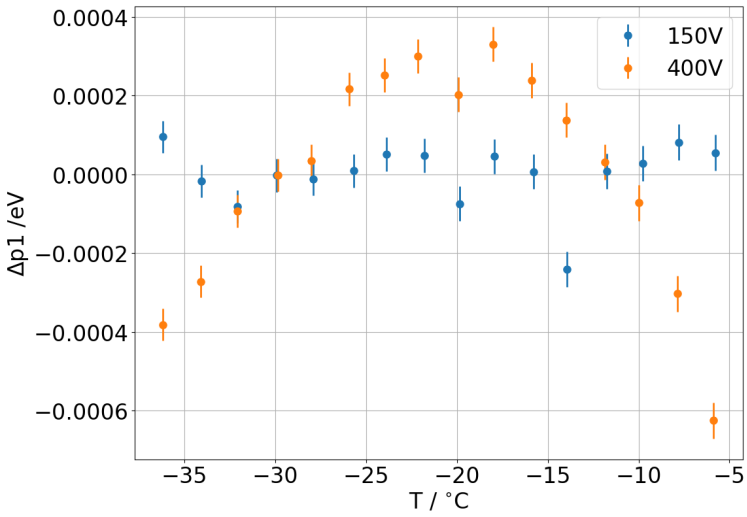

Figure 5.18.: Residuals of the fit to determine E_{eff} at 150 V and 400 V for the sample P3 before annealing for −36 °C to −6 °C.[4]

not reach a plateau region before hitting the power limit above 550 V. This is to be expected from the I-V characteristic which does not show a saturation region either. The plateau region of the samples is at $E_{\text{eff}} = 1.19\,\text{eV}$ and not at the expected $E_{\text{eff}} = 1.21\,\text{eV}$. It is uncertain if this offset is due to the used methodology, samples, or an effect due to irradiation.

All the samples show changes in E_{eff} with an increase in voltage. Therefore, no value of E_{eff} can be determined for irradiated samples which is applicable at all voltages. The onset of the saturation region shifts to higher voltages with fluence. As the same is expected for the depletion voltage, this strengthens the hypothesis that the onset of the saturation is linked to achieving full depletion. With these results, the change in scaling behaviour for samples irradiated to fluences above $1 \times 10^{15}\,\text{n}_{\text{eq}}\text{cm}^{-2}$, which was observed in previous studies, can be explained. For samples with lower fluences, values of compatible with 1.21 eV were measured. Such samples are typically tested and thus this is expected from the results of this thesis. As samples irradiated to fluences beyond $1 \times 10^{15}\,\text{n}_{\text{eq}}\text{cm}^{-2}$ are typically operated without being fully depleted, a lower value of E_{eff} is observed for them.

Thus, leakage current scaling with a constant value of E_{eff} is applicable in case of the ITk strip detector with estimated fluences up to $1 \times 10^{15}\,\text{n}_{\text{eq}}\text{cm}^{-2}$, a sensor thickness of 300 µm and a maximum operation voltage of 500 V. For samples irradiated to fluences beyond that, further studies are necessary to gain deeper understanding into the physics processes involved and to find applicable values of E_{eff} to allow for precise scaling of the leakage current.

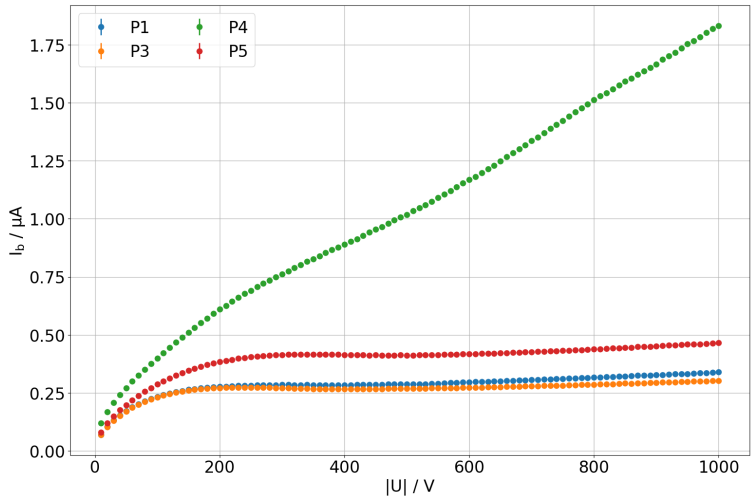

Figure 5.19.: Bulk current against voltage for all samples at −30 °C after annealing equivalent to 1170 min at −60 °C.

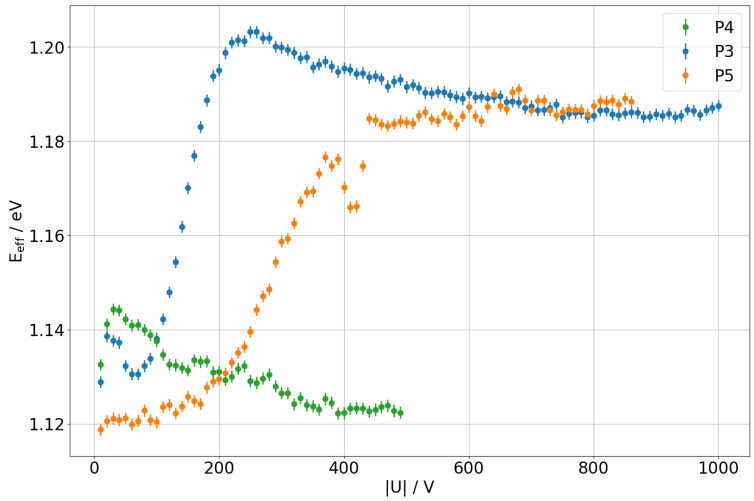

Figure 5.20.: E_{eff} against bias voltage for all samples before annealing.

5.7. Influence of Annealing on Leakage Current Scaling

As the leakage current as well as full depletion voltage are affected by annealing, an annealing study with samples at different fluences is performed. The samples are measured before annealing as well as between annealing steps up to an annealing time of approximately 6000 min at 60 °C.

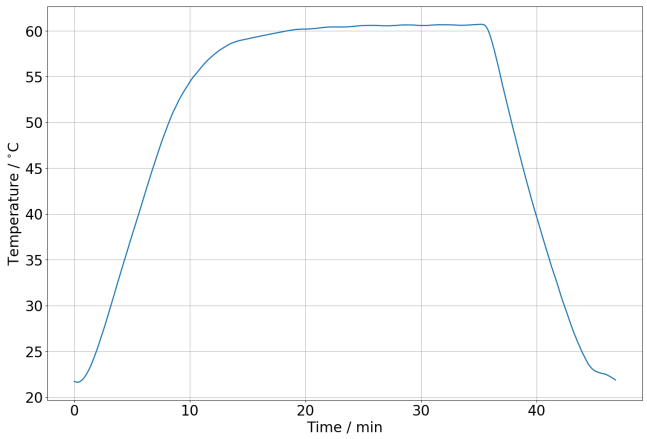

Figure 5.21.: Standard annealing step equating approximately 30 min of annealing at 60 °C.

The diodes are annealed in the climate chamber. For this process, a standard annealing step is used for a reproducible temperature profile shown in Figure 5.21. Starting from 20 °C, the chamber is set to 60 °C for 1950 s and then back to 20 °C. Although this has the downside of longer heating and cooling periods of the samples in comparison to placing the samples directly into a preheated oven, this method was selected as it allows remote operation and can be done between measurements of the samples without access to the chamber. The duration was chosen to roughly equate 30 min at 60 °C.

At later stages of annealing, multiple steps are performed consecutively due to the reduced annealing effects per time. This method was chosen instead of prolonging the heating period to achieve a consistent time scale. In Table 5.2, the steps are listed where the diodes are characterised.

In Figures 5.22a and 5.22b, a tool developed in [67] is used to estimate $|N_{\text{eff}}|$ and α respectively as function of the annealing duration for the sample P3 using the Hamburg model presented in Section 5.1. As the timescale includes cooling and heating periods, the steps are visible in the graphs in plateau regions. However, they are not corrected for annealing that might have happened before this study. Therefore it is expected that the relative drop in leakage current with annealing is lower than indicated in these graphs. Annealing effects before this study are assumed to be negligible for the later steps.

In two cases, the data needed to be modified before further usage. For the sample P1 at step 60, the leakage current measurement shows high noise in the temperature range from −20 °C to −32 °C. As the setup was performing a temperature scan

Table 5.2.: Annealing steps where I-V characteristics are measured for each sample.

Diodes	Steps
P1	39,44,60,90,135,200
P3	0,1,2,3,4,6,9,14, 24,39,60,90,135,200
P4	0,1,2,3,4,6,9,14, 24,39,44,60,90,135,200
P5	0,1,2,3,4,6,9,14, 28,39,60,90,135,200

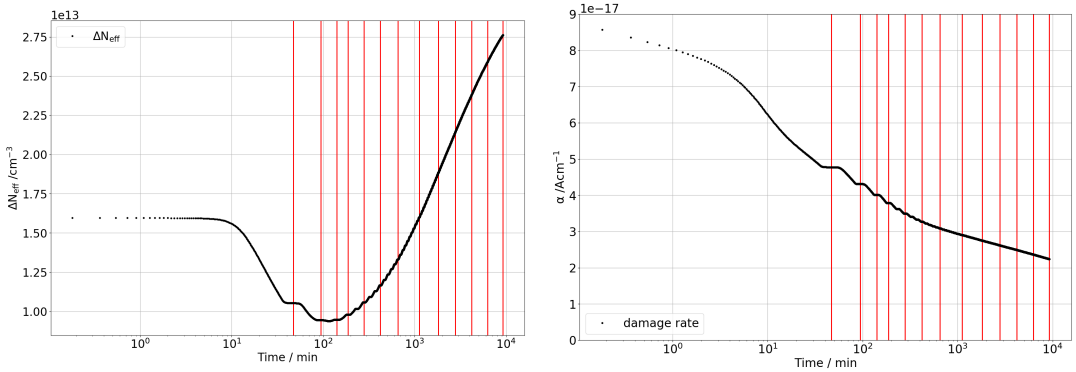

(a) (b)

Figure 5.22.: a) $|N_{\text{eff}}|$ and b) α against annealing duration for sample P3. I-V scans were performed at the vertical lines.

from 0 °C to −36 °C autonomously and measurements at other temperatures were unaffected, an external source is assumed. The affected measurements were removed from the data set. In case of the sample P4 at step 44, the bond to the guard ring of the diode was connected to the multimeter instead of the bond to the central implant. Therefore, the bulk current was determined by subtracting the edge current from the total current.

5.7.1. Decrease of the Current with Annealing

With annealing, the leakage current of the samples goes down as expected from the Hamburg model. A comparison between the observed relative reduction in leakage current at 250 V and 600 V and the expectations against annealing duration is shown in Figure 5.23 for the sample P3. The total annealing duration in this plot is equivalent to 6000 min of annealing at 60 °C. The predictions are taken from the tool developed in [67]. The measured currents as well as the predictions have been normalised to their value after the first annealing step. Additionally, the current measured before annealing is plotted at 10 s to allow the usage of a logarithmic scale.

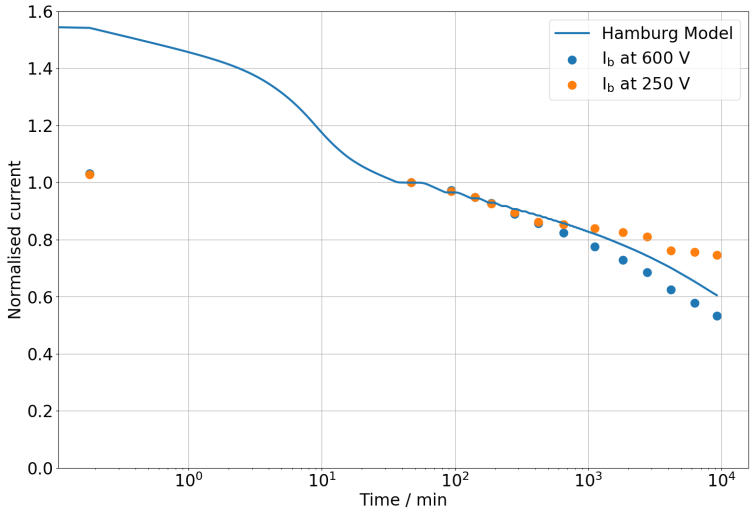

Figure 5.23.: Normalised current against annealing duration of the sample P3.

The plot shows a smaller relative reduction of leakage current in the measured data than expected from the model. This is especially pronounced in the small difference in measured leakage current before and after the first annealing step while the model predicts a drop by about a third. This is compatible with the assumption of annealing before this study, which would result in a smaller change during the investigated annealing times.

An unexpected feature is the deviation between the relative currents at 250 V and 600 V starting after 420 min of annealing at 60 °C (650 min of actual annealing duration). This can also be seen in Figures 5.24a and 5.24b, where I_b is shown for different annealing steps of the samples P1 and P3 at −30 °C. For both, the current decreases with annealing as expected from Equation 5.3. However, the shape of I_b against voltage changes with further annealing: At longer annealing times, I_b has a local maximum at approximately 250 V and a plateau region starts at 500 V. In Appendix A.2, this plot can be found for I_t and I_b of all samples at −30 °C and −10 °C, showing a similar effect in I_b for the samples P3 and P5 while P4 with the highest fluence of $3 \times 10^{15}\,\mathrm{n_{eq}cm^{-2}}$ does not show the same effect as no saturation region is reached either before or after annealing.

The effect is not found in I_t which is monotonically increasing with voltage for all samples. As there is no known physical explanation why the generated leakage current in a given volume decreases with an increase in voltage, it is assumed that the change in I_b is caused by a change of volume. As stated in Section 5.3, the current generated in the bulk can be either drained through the central implant (which is then measured as I_b) or the innermost guard ring based on the electric field in the bulk. Apparently, long term annealing affects the behaviour of the electric field in the edge region which makes the volume contributing to I_b dependent on voltage.

From Figure 5.24a, further insights into this effect can be gained. At around 250 V, I_b after 6000 min of annealing exceeds the current of the previous steps while in the plateau region, I_b decreases with annealing as expected. This implies that the volume

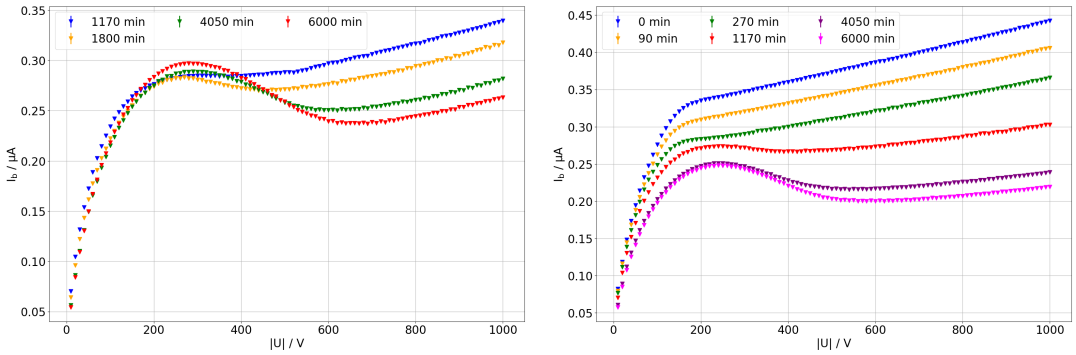

(a) (b)

Figure 5.24.: Bulk current of the samples a) P1 and b) P3 against voltage at −30 °C for different stages of annealing.

contributing to I_b at 250 V increases with annealing, while the additional volume is drained by the guard ring at higher voltages. To understand this effect, further investigation is necessary. With a TCT measurement, charge could be deposited at known locations and its drift to the electrodes investigated. Additionally, a simulation study could shed light on this.

As the nature of this effect is unknown, its effects on the temperature scaling behaviour remain unclear, resulting in a systematic uncertainty where this effect has a significant contribution to I_b. Based on the first significant deviation between the normalised currents at 250 V and 600 V, as shown in Figure 5.23, this effect is assumed to appear only after 420 min of annealing at 60 °C. As the decrease in leakage current at high voltages is compatible with the expectations from the Hamburg model, this effect is assumed to be negligible above 600 V for the investigated samples.

5.7.2. Changes of the Scaling Behaviour

Annealing affects the observed E_{eff} as a function of voltage for all samples. In Figure 5.25, this is shown for the sample P3. The most obvious effect is visible in the shift of the onset of the plateau region to higher bias voltages at the later stages of annealing. At 250 V, E_{eff} first increases into a peak after 420 min of annealing at 60 °C and drops below the original level at later stages of annealing. However, this peak appears in the region where I_b shows unexpected results. Thus, it is likely that this peak is caused by the change in volume drained by the central implant. As it is expected in the Hamburg model, that the full depletion voltage changes with annealing, the scaling behaviour in the region of the depletion voltage is especially interesting. However, this would require a deeper understanding of volumes contributing to I_b or samples with a different geometry which do not exhibit the same effect. In Appendix A.3, plots similar to Figure 5.25 can be found for all samples. Additionally, E_{eff} against voltage is shown there for all samples at different stages of annealing.

For annealing times up to 120 min at 60 °C, little change is observed. However, long term annealing up to 6000 min shows a slight increase of E_{eff} in the plateau region.

In Figure 5.26, E_{eff} as a function of annealing and voltage is shown for all samples.

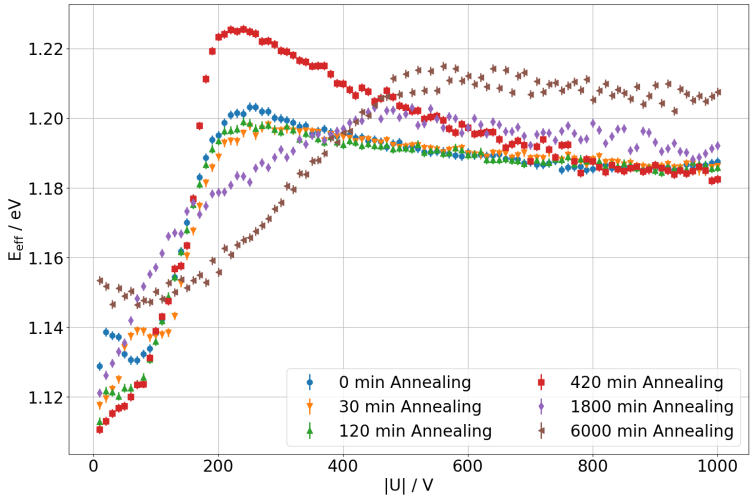

Figure 5.25.: E_{eff} against voltage at different stages of annealing for P3

In case of P4, E_{eff} decreases with voltage before annealing which changes to an increase with annealing after long term annealing. This hints that annealing could be a relevant parameter in selecting the correct value in E_{eff} when scaling the leakage current of samples irradiated beyond $1 \times 10^{15}\,\text{n}_{\text{eq}}\text{cm}^{-2}$. However, further studies with a sample size larger than one are necessary to follow up on this. For P1, P3 and P5, the only significant changes are in the onset of the plateau region after long term annealing. As all of these samples are affected by the change in volume which is drained by the central implant after long term annealing, no conclusion can be drawn by that change. Thus, the annealing study confirms the applicability of 1.21 eV above depletion voltage for samples irradiated up to $1 \times 10^{15}\,\text{n}_{\text{eq}}\text{cm}^{-2}$ in short term annealing but is inconclusive regarding the effects of long term annealing.

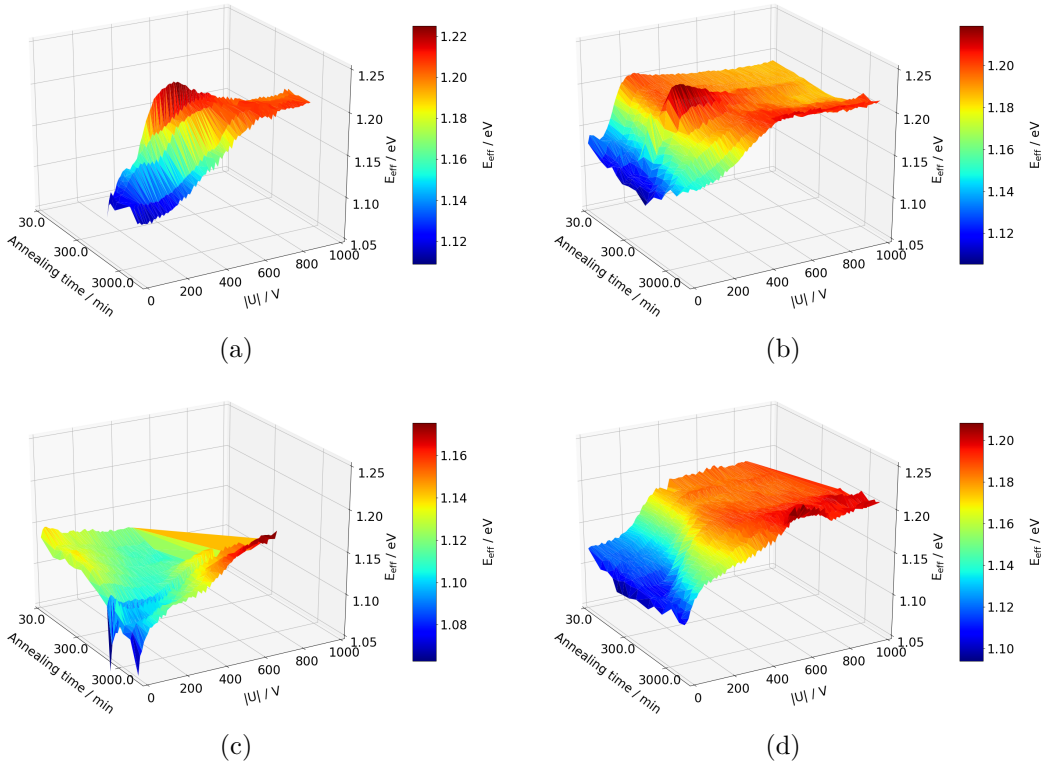

Figure 5.26.: E_{eff} against voltage at different stages of annealing for a) P1 b) P3 c) P4 and d) P5

6. Conclusions

The LHC will be upgraded to the HL-LHC in 2026. Due to the then increased number of collisions, and therefore number of tracks per bunch crossing, a higher granularity and an increased radiation hardness is required thereby necessitating extensive upgrades of the LHC experiments. One of the upgrades of the ATLAS experiment is the Inner Tracker (ITk), an all silicon detector using pixel and strip sensors, which will replace the Inner Detector (ID).

Components for the strip detector of the ITk strip detector will be built at sites throughout the world. Dortmund is one of the sites assembling hybrids and modules for the end cap. The planned production flow was developed and is presented in this thesis. In the next steps, production and test stations will be set up and final decisions on QA and QC procedures will be implemented. In the final step before production, the ITk strip collaboration will qualify the site in 2020. For this, modules will be built and tested in Dortmund, which will be then sent to other institutions to verify that they are inside of specifications. Additionally, members of the collaboration will inspect the site to qualify the production flow and verify that the necessary production rates can be achieved.

The scaling of leakage current with temperature in irradiated diodes with fluences from $6 \times 10^{14}\,\mathrm{n_{eq}cm^{-2}}$ to $3 \times 10^{15}\,\mathrm{n_{eq}cm^{-2}}$ was investigated. A novel approach of this study was the emphasis on the dependence of the scaling parameter E_{eff} on voltage showing that E_{eff} saturates at values between 1.18 eV and 1.21 eV when the bulk is depleted. If the bulk is not fully depleted, lower values of E_{eff} were observed. This supports the hypothesis, that the lower value of E_{eff} observed for samples with a fluence above $1 \times 10^{15}\,\mathrm{n_{eq}cm^{-2}}$ in previous studies is caused by them not being fully depleted. Therefore, the established value of $E_{\mathrm{eff}} = 1.21\,\mathrm{eV}$ can be used for detectors exposed to fluences below $1 \times 10^{15}\,\mathrm{n_{eq}cm^{-2}}$, for example the ITk strip detector, to scale with high accuracy. However, this value is not applicable for detectors exposed to higher fluences, like the ITk pixel detector. This study also investigated the change of E_{eff} with annealing, which showed no significant change in short term annealing. However, an effect which is not yet understood caused the volume drained by the central implant to change with voltage in an unexpected way after long term annealing.

Based on this thesis, investigation of the scaling behaviour with an increased sample size would allow to gain a more comprehensive understanding and allow to find suitable values of E_{eff} for samples irradiated to fluences above $3 \times 10^{15}\,\mathrm{n_{eq}cm^{-2}}$.

Bibliography

[1] L. Evans and P. Bryant. *LHC Machine*. JINST, 3:S08001, 2008.

[2] G. Aad et al. *Observation of a new particle in the search for the Standard Model Higgs boson with the ATLAS detector at the LHC*. Phys. Lett., B716:1–29, 2012.

[3] S. Chatrchyan et al. *Observation of a new boson at a mass of 125 GeV with the CMS experiment at the LHC*. Phys. Lett., B716:30–61, 2012.

[4] F. Wizemann et al. *Temperature scaling of reverse current generated in proton irradiated silicon bulk*. JINST, 14:P07008, July 2019.

[5] *Convention for the establishment of a European organization for nuclear research : Paris, 1st July, 1953 : as amended*. CERN, Geneva, 1971.

[6] G. Arnison et al. *Experimental Observation of Isolated Large Transverse Energy Electrons with Associated Missing Energy at s**(1/2) = 540-GeV*. Phys. Lett., B122:103–116, 1983.

[7] M. Banner et al. *Observation of Single Isolated Electrons of High Transverse Momentum in Events with Missing Transverse Energy at the CERN anti-p p Collider*. Phys. Lett., B122:476–485, 1983.

[8] E. A. Mobs. *The CERN accelerator complex. Complexe des accélérateurs du CERN*, Oct 2016. URL `http://cds.cern.ch/record/2225847`. General Photo, OPEN-PHO-ACCEL-2016-013.

[9] F. Abe et al. *Observation of top quark production in $\bar{p}p$ collisions*. Phys. Rev. Lett., 74:2626–2631, 1995.

[10] S. Abachi et al. *Observation of the top quark*. Phys. Rev. Lett., 74:2632–2637, 1995.

[11] *The HL-LHC project website*. URL `http://hilumilhc.web.cern.ch/about/hl-lhc-project`. Online, accessed: 25.04.2019.

[12] J. Pequenao. *Computer generated image of the whole ATLAS detector*. Mar 2008. URL `http://cds.cern.ch/record/1095924`.

[13] J. Pequenao and P. Schaffner. *How ATLAS detects particles: diagram of particle paths in the detector*. Jan 2013. URL `https://cds.cern.ch/record/1505342`.

[14] ATLAS Collaboration. *Track Reconstruction Performance of the ATLAS Inner Detector at $\sqrt{s} = 13$ TeV*. Technical Report ATL-PHYS-PUB-2015-018, CERN, Geneva, Jul 2015.

[15] G. Aad et al. *The ATLAS Experiment at the CERN Large Hadron Collider*. JINST, 3:S08003, 2008.

[16] E. Abat et al. *The ATLAS Transition Radiation Tracker (TRT) proportional drift tube: Design and performance*. JINST, 3:P02013, 2008.

[17] Y. Giomataris, P. Rebourgeard, J. P. Robert, and G. Charpak. *MICROMEGAS: A High granularity position sensitive gaseous detector for high particle flux environments*. Nucl. Instrum. Meth., A376:29–35, 1996.

[18] M. Lipinski. *The Phase-1 Upgrade of the CMS Pixel Detector*. Technical Report CMS-CR-2017-135. 06, CERN, Geneva, May 2017.

[19] A. A. Alves, Jr. et al. *The LHCb Detector at the LHC*. JINST, 3:S08005, 2008.

[20] K. Aamodt et al. *The ALICE experiment at the CERN LHC*. JINST, 3:S08002, 2008.

[21] G. Apollinari et al., editors. *High-Luminosity Large Hadron Collider (HL-LHC): Technical Design Report V. 0.1*, volume 4/2017 of *CERN Yellow Reports: Monographs*. CERN, Geneva, 2017.

[22] ATLAS Collaboration. *Physics at a High-Luminosity LHC with ATLAS*. Technical Report ATL-PHYS-PUB-2013-007, CERN, Geneva, Jul 2013.

[23] P. Azzi et al. *Standard Model Physics at the HL-LHC and HE-LHC*. In *HL/HE-LHC Workshop: Workshop on the Physics of HL-LHC, and Perspectives at HE-LHC*, 2019.

[24] M. Cepeda et al. *Higgs Physics at the HL-LHC and HE-LHC*. In *HL/HE-LHC Workshop: Workshop on the Physics of HL-LHC, and Perspectives at HE-LHC*, 2019.

[25] X. Cid Vidal et al. *Beyond the Standard Model Physics at the HL-LHC and HE-LHC*. In *HL/HE-LHC Workshop: Workshop on the Physics of HL-LHC, and Perspectives at HE-LHC*, 2018.

[26] A. Cerri et al. *Opportunities in Flavour Physics at the HL-LHC and HE-LHC*. In *HL/HE-LHC Workshop: Workshop on the Physics of HL-LHC, and Perspectives at HE-LHC*, 2018.

[27] Z. Citron et al. *Future physics opportunities for high-density QCD at the LHC with heavy-ion and proton beams*. In *HL/HE-LHC Workshop: Workshop on the Physics of HL-LHC, and Perspectives at HE-LHC*, 2018.

[28] ATLAS Collaboration. *Technical Design Report for the ATLAS Inner Tracker Strip Detector*. Technical Report CERN-LHCC-2017-005. ATLAS-TDR-025, CERN, Geneva, Apr 2017.

[29] ATLAS Collaboration. *Letter of Intent for the Phase-II Upgrade of the ATLAS Experiment*. Technical Report CERN-LHCC-2012-022. LHCC-I-023, CERN, Geneva, Dec 2012. Draft version for comments.

[30] S. M. Sze and M.-K. Lee. *Semiconductor devices : physics and technology*. John Wiley & Sons, New York, 3rd edition, 2012. ISBN 978-0470-53794-7.

[31] H. Kolanoski and N. Wermes. *Teilchendetektoren Grundlagen und Anwendungen*. Springer Spektrum, 2016.

[32] M. S. Tyagi. *Introduction to Semiconductor Materials and Devices*. John Wiley & Sons, 1991.

[33] A. Gisen. *Quad module prototypes and design improvement studies of planar n^+-in-n silicon pixel sensors for the ATLAS Inner Tracker upgrade*. Dissertation, Technische Universität Dortmund, 2018.

[34] G. Lutz. *Semiconductor Radiation Detector Device Physics*. Springer-Verlag, 1st edition, 1999.

[35] A. Chilingarov. *Generation current temperature scaling, Part 1: Theory*. Technical Report PH-EP-Tech-Note-2013-001, CERN, Geneva, Jan 2013.

[36] A. Chilingarov. *Temperature dependence of the current generated in Si bulk*. JINST, 8(10):P10003, 2013.

[37] M. A. Green. *Intrinsic concentration, effective densities of states, and effective mass in silicon*. Journal of Applied Physics, 67(6):2944–2954, 1990.

[38] D. W. R. Leo. *Techniques for Nuclear and Particle Physics Experiments*. Springer-Verlag Berlin Heidelberg, 2. auflage edition, 1987.

[39] C. Leroy and P.-G. Rancoita. *Principles of Radiation Interaction in Matter and Detection*. World Scientific, 2nd edition, 2009.

[40] T. Wittig. *Slim edge studies, design and quality control of planar ATLAS IBL pixel sensors*. Dissertation, TU Dortmund, 2013.

[41] S. Parker, C. Kenney, and J. Segal. *3D — A proposed new architecture for solid-state radiation detectors*. Nucl. Instrum. Meth., A395(3):328 – 343, 1997. Proceedings of the Third International Workshop on Semiconductor Pixel Detectors for Particles and X-rays.

[42] ATLAS Collaboration. *Technical Design Report for the Phase-II Upgrade of the ATLAS TDAQ System*. Technical Report CERN-LHCC-2017-020. ATLAS-TDR-029, CERN, Geneva, Sep 2017.

[43] ATLAS Collaboration. *Technical Design Report for the ATLAS Inner Tracker Pixel Detector*. Technical Report CERN-LHCC-2017-021. ATLAS-TDR-030, CERN, Geneva, Sep 2017.

[44] ATLAS Collaboration. *Expected Tracking Performance of the ATLAS Inner Tracker at the HL-LHC*. Technical Report ATL-PHYS-PUB-2019-014, CERN, Geneva, Mar 2019.

[45] ATLAS Collaboration. *Simulated HL-LHC collision event in the ATLAS detector*. General Photo, May 2019. URL `https://cds.cern.ch/record/2674770`.

[46] J. S. Keller. *The ATLAS ITk strip detector system for the High Luminosity LHC upgrade*. Technical report, April 2019.

[47] ATLAS Collaboration. *Technical Proposal: A High-Granularity Timing Detector for the ATLAS Phase-II Upgrade*. Technical Report CERN-LHCC-2018-023. LHCC-P-012, CERN, Geneva, Jun 2018.

[48] M. Garcia-Sciveres. *The RD53A Integrated Circuit*. Technical Report CERN-RD53-PUB-17-001, CERN, Geneva, Oct 2017.

[49] K. Dette. *Total Ionising Dose effects in the FE-I4 front-end chip of the ATLAS Pixel IBL detector*. JINST, 11(11):C11028, 2016.

[50] A. Affolder et al. *DC-DC converters with reduced mass for trackers at the HL-LHC*. JINST, 6(11):C11035–C11035, nov 2011.

[51] A. Salzburger. *Optimisation of the ATLAS Track Reconstruction Software for Run-2*. J. Phys. Conf. Ser., 664(7):072042, 2015.

[52] J. Lönker. Private Communication, 2019.

[53] G. Lindstrom. *Radiation damage in silicon detectors*. Nucl. Instrum. Meth., A512:30–43, 2003.

[54] G. Troska. *Development and operation of a testbeam setup for qualification studies of ATLAS Pixel Sensors*. Dissertation, TU Dortmund, January 2012.

[55] D. V. Lang. *Deep-level transient spectroscopy: A new method to characterize traps in semiconductors*. Journal of Applied Physics, 45(7):3023–3032, 1974.

[56] M. Moll. *Radiation Damage in Silicon Particle Dectectors*. Dissertation, Universität Hamburg, 1999.

[57] R. Wunstdorf. *Systematische Untersuchungen zur Strahlenresitenz von Silizium-Detektoren für die Verwendung in Hochenergiephysik-Experimenten*. Dissertation, Universität Hamburg, 1992.

[58] G. Kramberger, V. Cindro, I. Mandic, M. Mikuz, M. Milovanovic, M. Zavrtanik, and K. Zagar. *Investigation of Irradiated Silicon Detectors by Edge-TCT*. IEEE Trans. Nucl. Sci., 57(4):2294–2302, 2010.

[59] L. J. Beattie, T. J. Brodbeck, A. Chilingarov, G. Hughes, S. A. McGarry, P. N. Ratoff, and T. Sloan. *The electric field in irradiated silicon detectors*. Nucl. Instrum. Meth., A418:314–321, 1998.

[60] S. Wonsak, A. Affolder, G. Casse, P. Dervan, I. Tsurin, and M. Wormald. *Measurements of the reverse current of highly irradiated silicon sensors*. Nucl. Instrum. Meth., A796:126–130, 2015.

[61] M. Wiehe, S. Wonsak, S. Kuehn, U. Parzefall, and G. Casse. *Measurements of the reverse current of highly irradiated silicon sensors to determine the effective energy and current related damage rate.* Nucl. Instrum. Meth., A877:51–55, 2018.

[62] ATLAS Collaboration. *A Leakage Current-based Measurement of the Radiation Damage in the ATLAS Pixel Detector.* Technical Report ATL-INDET-PUB-2014-004, CERN, Geneva, Aug 2014.

[63] A. Rummler. *Design and Commissioning of a Setup for Charge Collection Efficiency Measurements of Highly Irradiated ATLAS Pixel Sensors.* Diploma thesis, TU Dortmund, 2009.

[64] M. Glaser, L. Durieu, F. Lemeilleur, M. Tavlet, C. Leroy, and P. Roy. *New irradiation zones at the CERN PS.* Nucl. Instrum. Meth., A426:72–77, 1999.

[65] S. Dungs. *Design und Charakterisierung von planaren n^+-in-p Pixelsensoren für das ATLAS Experiment.* Master thesis, TU Dortmund, 2017.

[66] R. Klingenberg, S. Altenheiner, M. Andrzejewski, K. Dette, C. Gössling, A. Rummler, and F. Wizemann. *Temperature-dependent characterizations of irradiated planar n + -in-n pixel assemblies.* Nucl. Instrum. Meth., A765:135–139, 2014.

[67] C. Krause. *Entwicklung eines Programmes zur Berechnung von Annealingeffekten in bestrahltem Silizium nach dem Hamburger Modell.* Bachelor thesis, TU Dortmund, 2019.

Danksagung

Bei der Erstellung dieser Arbeit habe ich von vielen Seiten auf unterschiedliche Art Unterstützung bekommen, die diese Arbeit in diesem äußerst interessanten Gebiet innerhalb der internationalen ATLAS-Kollaboration ermöglicht haben.

Ein großer Dank gilt Prof. Dr. Kevin Kröninger dafür, dass er mir die Arbeit an diesem tollen Lehrstuhl ermöglicht hat und die Betreuung übernommen hat. Dr. Johannes Albrecht danke ich dafür, dass er sich bereit erklärt hat, das Zweitgutachten dieser Arbeit zu übernehmen.

Ebenso möchte ich PD Dr. Reiner Klingenberg danken, der mich bis zu seinem plötzlichen Tod betreut und unterstützt hat. Es war eine tolle Zusammenarbeit mit Dir und danke dafür, dass Du mich mit deiner stetigen Neugier angesteckt hast.

Auch möchte ich Prof. Dr. Claus Gößling danken, der mich vor gut sechs Jahren für dieses Themengebiet begeistert und mich in meiner Bachelor- und Masterarbeit betreut hat.

Ein besonderer Dank gilt Jens, der mir dabei geholfen hat die Arbeit in der Endphase zu fokussieren und mir mit seinen Korrekturen zu dieser Arbeit enorm geholfen hat.

Einen Dank möchte Ich auch Silke, Jonas und Mike aussprechen für die hervorragende Zusammenarbeit für die Vorbereitung der Produktion von Streifenmodulen. Silke bewundere ich für den großen Einsatz, den sie trotz ihrer schweren Krankheit bis zu ihrem Tod erbracht hat - und dabei oftmals für viel Freude bei uns allen gesorgt hat. Ich danke Jonas dafür, dass er mir stets dabei geholfen hat, innerhalb der ITk Strip Kollaboration zu navigieren und viele meiner Fragen beantworten konnte. Mike gilt mein Dank dafür, dass er sich hervorragend um die vielen Herausforderungen gekümmert hat, vor die uns der Reinraum gestellt hat - und auch immer schnell einen Bonddraht gesetzt hat, wenn ich mal wieder einen beschädigt habe.

Auch möchte ich Andreas danken, an den ich mich immer wieder mit kleineren und größeren Problemen wenden konnte und der mir auch geholfen hat, in dem er diese Arbeit Korrektur gelesen hat.

Mareike und Valerie gilt ein großer Dank für die tolle Bürogenossenschaft, dafür, dass man sich gemeinsam über Protokolle ärgern konnte sowie für die gemeinsamen Eispausen im Sommer.

Andrea und Markus möchte Ich danken, die in vielen großen und kleinen Belangen eine bemerkenswerten Unterstützung waren.

Ich möchte mich auch beim Rest der ATLAS Upgrade Gruppe bedanken für die tolle Zusammenarbeit, sei es beim Programmieren oder bei Problematiken im Labor.

Dem ganzen Lehrstuhl möchte ich für das ausgesprochen gute Klima danken und die gemeinsam verbrachte Zeit in der Uni somit zu verschönern. Insbesondere zu nennen sind hierbei die Frühstücksrunde, die Mensarunde sowie die Café Che Fraktion (zwischen denen ich munter gewechselt habe) sowie diverse gemeinsam verspeiste

Kuchen - als auch für viel gemeinsamen Spaß bei den Frühjahrestagungen. Lasertag und E4 e.V. gilt ein Dank für die vielen gemeinsamen lustigen Unternehmungen.

Meinem Vater Dino und meinem Bruder Julian möchte ich für die wertvolle Unterstützung während meiner gesamten Universitätslaufbahn danken. Dino gilt besonderer Dank für seine stetige Unterstützung in meinen Studium der Physik und für das geduldige Korrekturlesen aller meiner Arbeiten. Bei Julian möchte ich den tollen Chauffeurservice hervorheben, wenn wir zusammen in die Heimat gefahren sind.

Meinen Mitbewohnern Malte und Steven will Ich danken, dass Sie mir geholfen haben die Arbeit in der Uni zu lassen und es auch Verständnis hatten, wenn die Laune mal im Keller war.

Publications, Conference Contributions and Talks

Publications

A. Gisen, S. Altenheiner, I. Burmeister, C. Gößling, R. Klingenberg, K. Kröninger, J. Lönker, M. Weers, F. Wizemann: *Planar n-in-n quad module prototypes for the ATLAS ITk upgrade at HL-LHC.* JINST 12, December 2017, C12032.

M. Weers, S. Altenheiner, A. Gisen, M. Hötting, V. Hohm, K. Kröninger, J. Lönker, M. Muschak, A.K. Raytarowski, J. Weingarten, F. Wizemann: *Lab and test beam results of irradiated silicon sensors with modified ATLAS pixel implantations.* JINST 13, November 2018. C11004.

A. Gisen, S. Altenheiner, C. Gößling, M. Grothe, R. Klingenberg, K. Kröninger, J. Lönker, M. Weers, T. Wittig, F. Wizemann : *Investigation of modified ATLAS pixel implantations after irradiation with neutrons.* Nucl.Instrum.Meth. A**924**, April 2019, pp. 203-207.

R.F.H. Hunter et al: *First bulk and surface results for the ATLAS ITk Strip stereo annulus sensors.* Nucl.Instrum.Meth. A**924**, April 2019, pp. 142-146.

F. Wizemann, A. Gisen, K. Kröninger and J. Weingarten: *Temperature scaling of reverse current generated in proton irradiated silicon bulk.* JINST 14, July 2019, P07008.

M. Wagner, A. Gisen, M. Hötting, V. Hohm, C. Krause, K. Kröninger, A. Kroner, J. Lönker, M. Muschak, J. Weingarten, F. Wizemann: *First Annealing Studies of Irradiated Silicon Sensors with Modified ATLAS Pixel Implantations.* Submitted to Nucl.Instrum.Meth. A in August 2019.

Conference Contributions and Talks

F. Wizemann: *ATLAS ITk Silicon Strip Module Production in Dortmund.* Poster at the “Frühjahrstagung der DPG”, March 2017, Münster, Germany.

F. Wizemann: *Charakterisierung von bestrahlten Si-Dioden.* Talk at the “49. Herbstschule für Hochenergiephysik“, September 2017, Maria Laach, Germany.

F. Wizemann: *Charakterisierung von bestrahlten Si-Dioden.* Talk at the “Frühjahrstagung der DPG“, March 2018, Hamburg, Germany.

F. Wizemann: *Measurement of E_{eff} for Irradiated and Annealed Diodes.* Talk at the “33rd RD50 Workshop“, November 2018, Geneva, Switzerland.

F. Wizemann: *Measurement of E_{eff} for Irradiated and Annealed Diodes.* Talk at the “Frühjahrstagung der DPG“, March 2019, Aachen, Germany.

A. Appendix

A.1. Influence of the Temperature Interval used to Determine E_{eff}

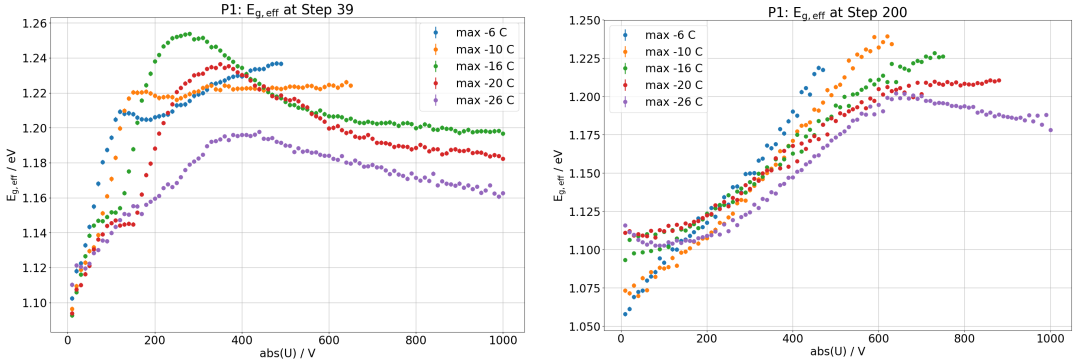

Figure A.1.: E_{eff} for different temperature intervals for P1 before annealing and after 1800 min of annealing at 60 °C.

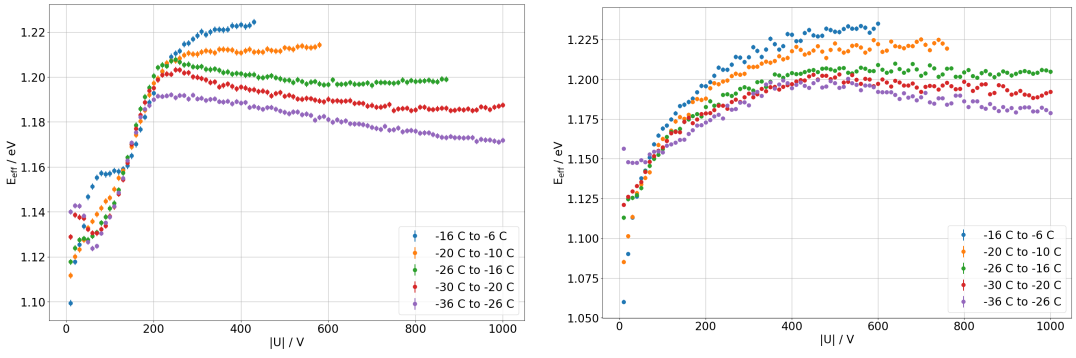

Figure A.2.: E_{eff} for different temperature intervals for P3 before annealing and after 1800 min of annealing at 60 °C.

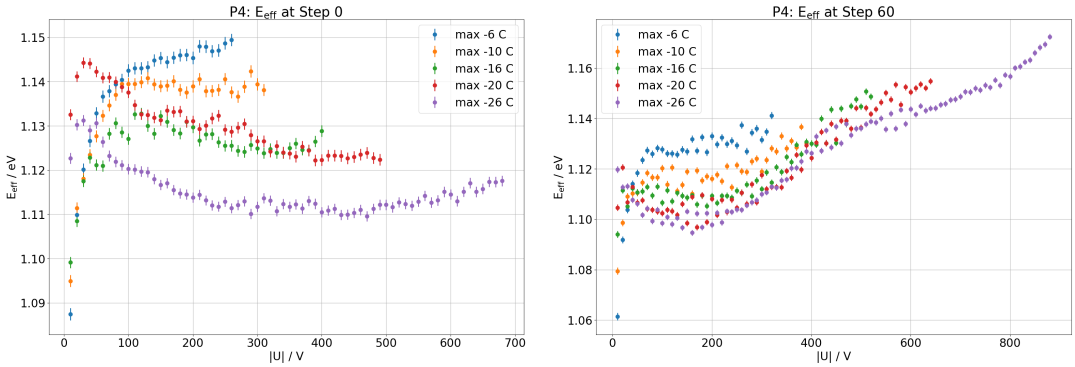

Figure A.3.: E_{eff} for different temperature intervals for P4 before annealing and after 1800 min of annealing at 60 °C.

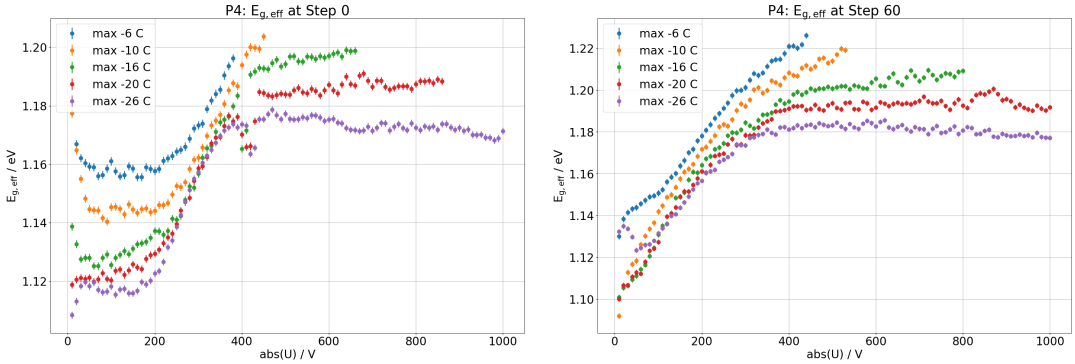

Figure A.4.: E_{eff} for different temperature intervals for P5 before annealing and after 1800 min of annealing at 60 °C.

A.2. I-V Characteristics at Different Stages of Annealing

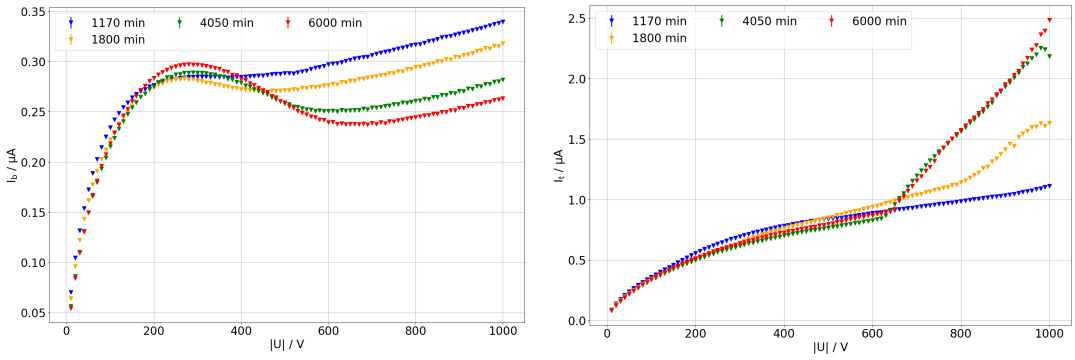

Figure A.5.: a) Bulk current and b) total current of the sample P1 against voltage at −30 °C for different stages of annealing.

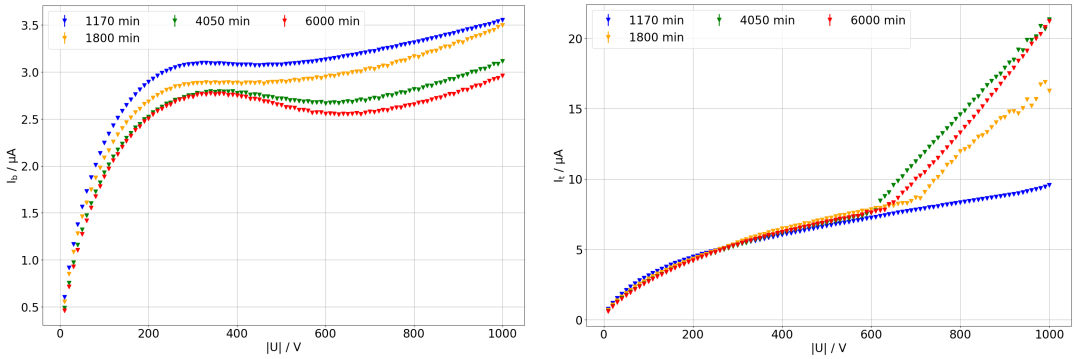

Figure A.6.: a) Bulk current and b) total current of the sample P1 against voltage at −10 °C for different stages of annealing.

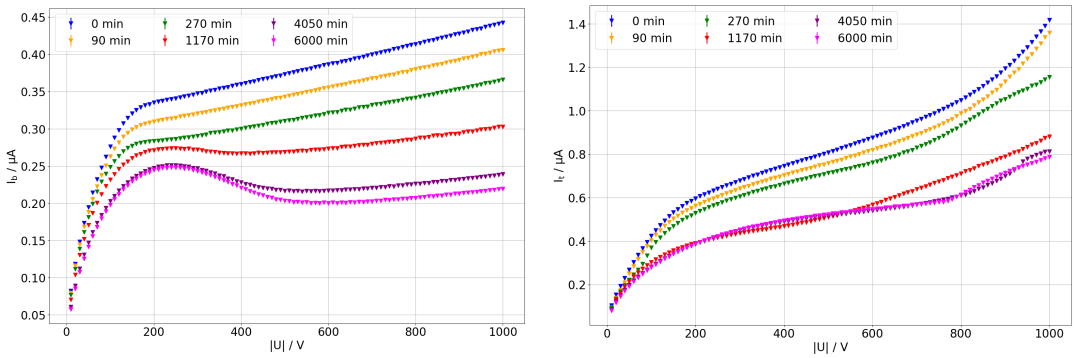

Figure A.7.: a) Bulk current and b) total current of the sample P3 against voltage at −30 °C for different stages of annealing.

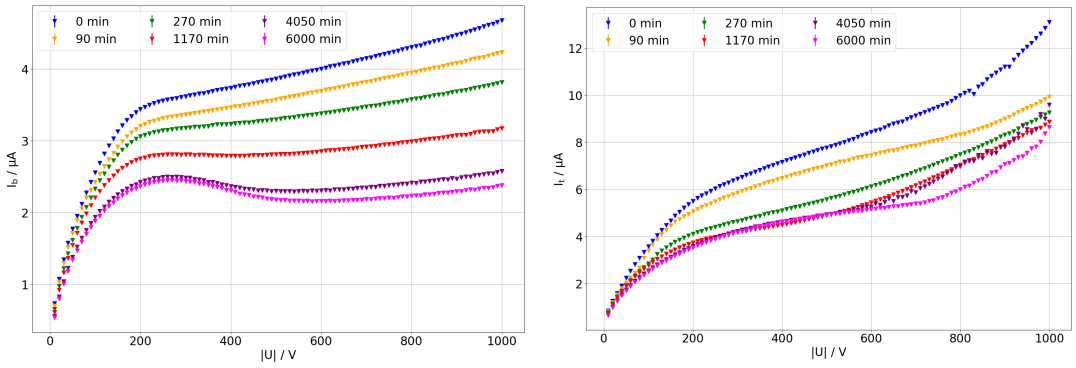

Figure A.8.: a) Bulk current and b) total current of the sample P3 against voltage at −10 °C for different stages of annealing.

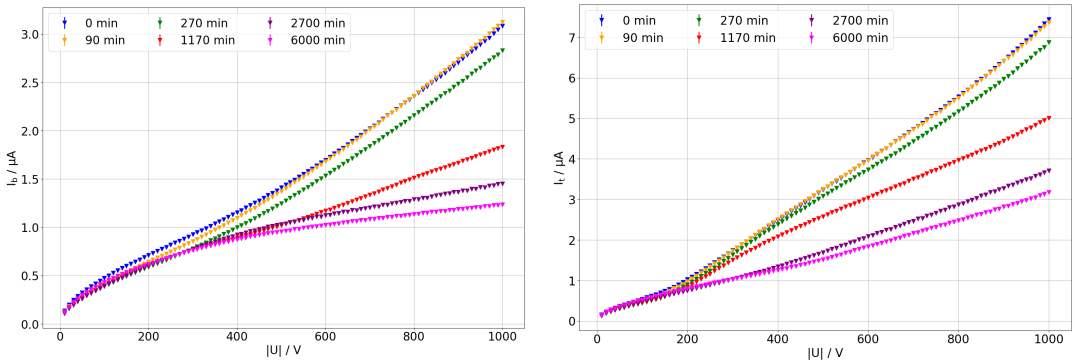

Figure A.9.: a) Bulk current and b) total current of the sample P4 against voltage at −30 °C for different stages of annealing.

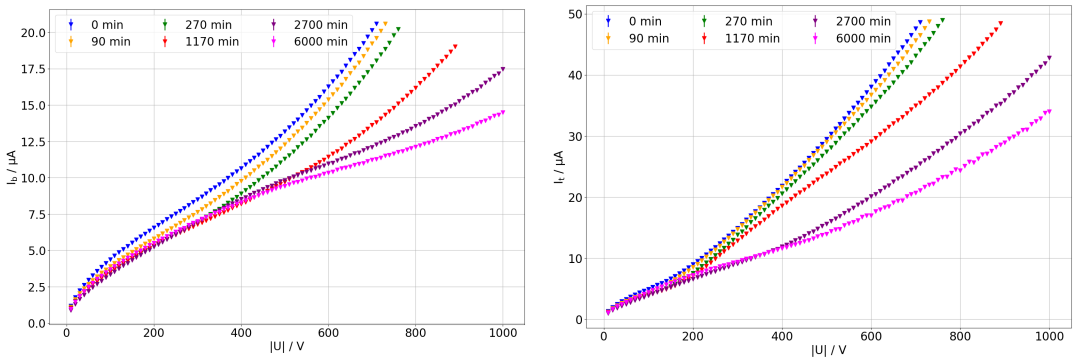

Figure A.10.: a) Bulk current and b) total current of the sample P4 against voltage at −10 °C for different stages of annealing.

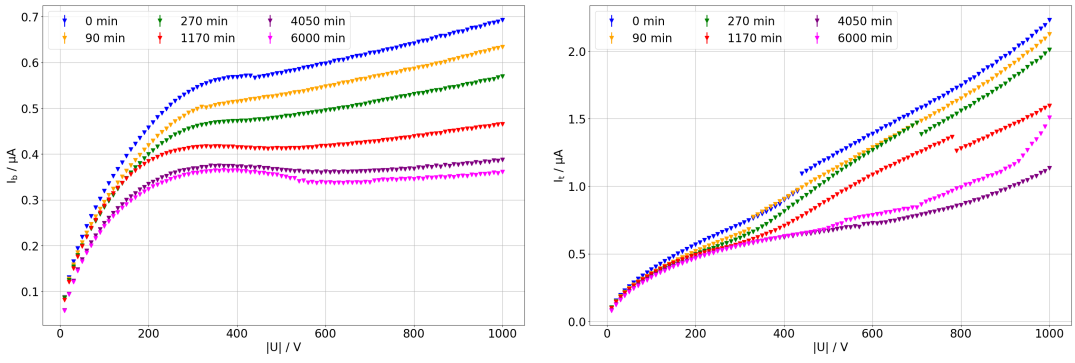

Figure A.11.: a) Bulk current and b) total current of the sample P5 against voltage at −30 °C for different stages of annealing.

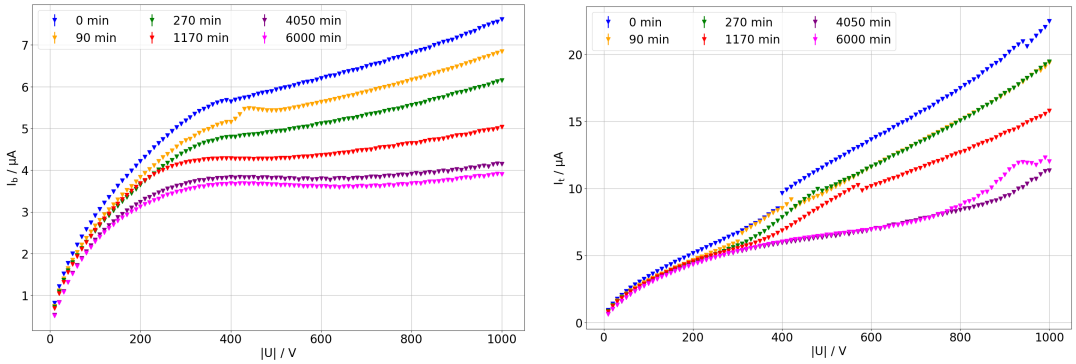

Figure A.12.: a) Bulk current and b) total current of the sample P5 against voltage at −10 °C for different stages of annealing.

A.3. Changes of the Scaling Behaviour

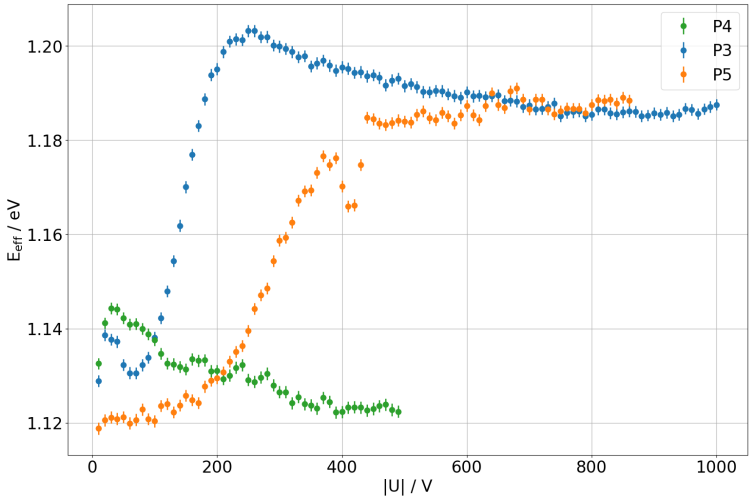

Figure A.13.: E_{eff} against voltage for P3, P4 and P5 before annealing.

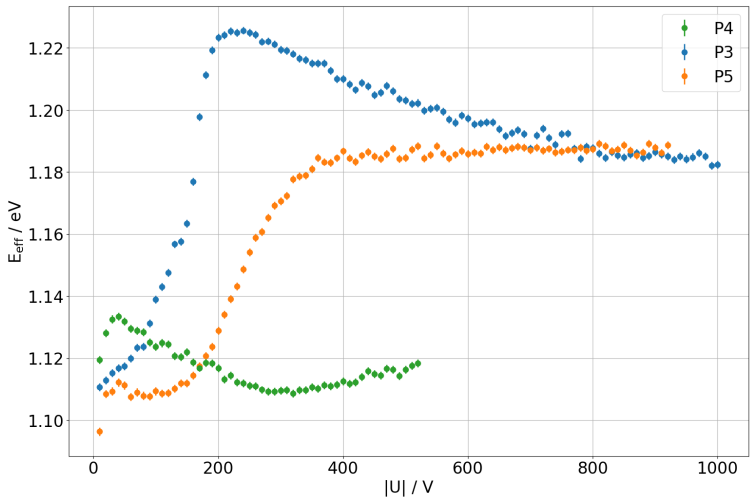

Figure A.14.: E_{eff} against voltage for P3, P4 and P5 after 420 min of annealing at 60 °C.

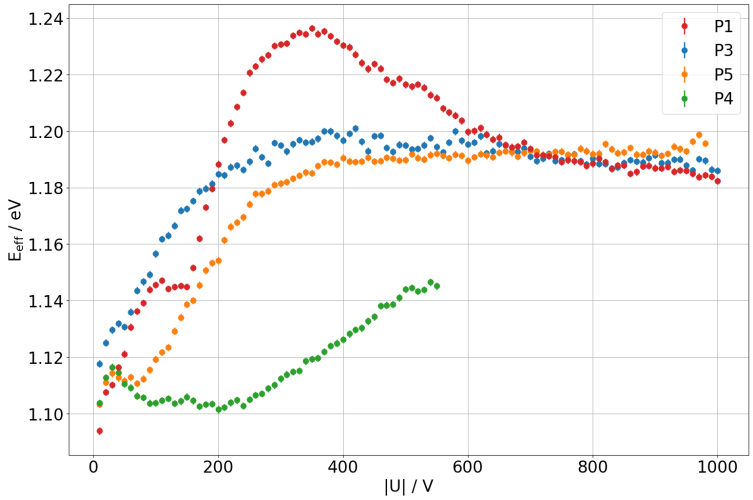

Figure A.15.: E_{eff} against voltage for all samples after 1180 min of annealing at 60 °C.

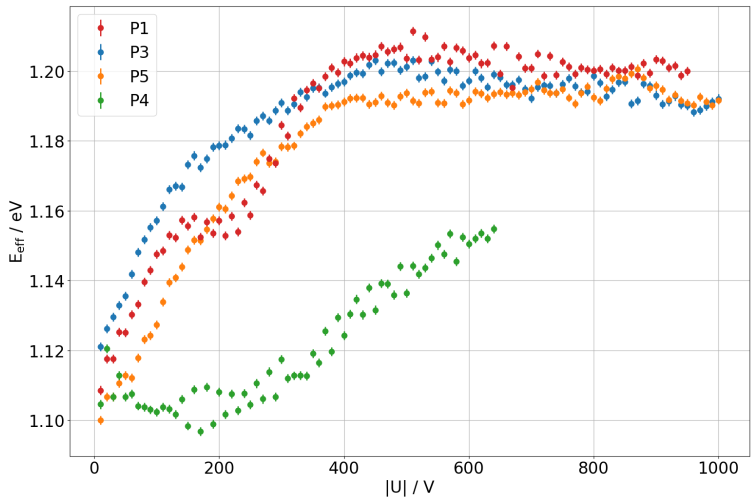

Figure A.16.: E_{eff} against voltage for all samples after 1800 min of annealing at 60 °C.

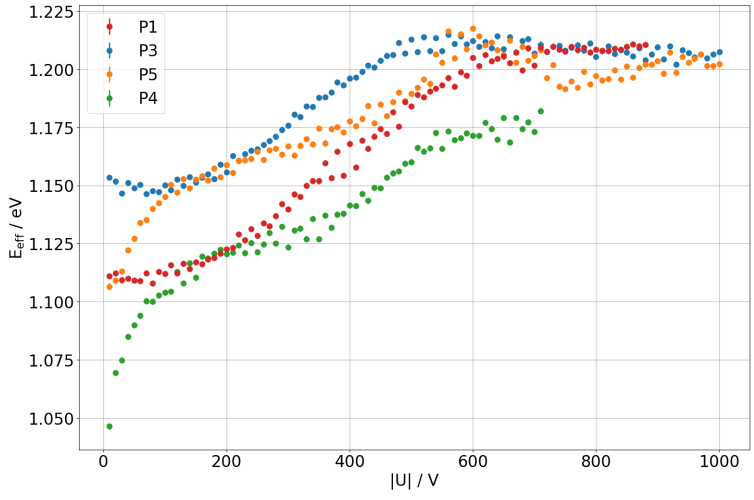

Figure A.17.: E_{eff} against voltage for all samples after 6000 min of annealing at 60 °C.

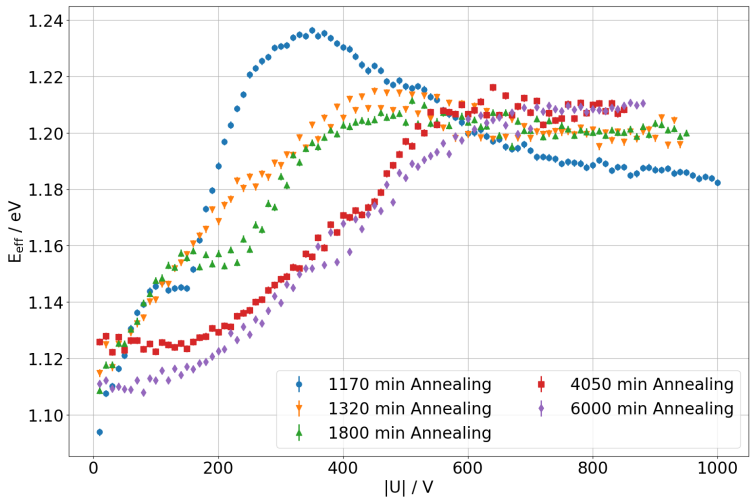

Figure A.18.: E_{eff} against voltage at different stages of annealing for P1.

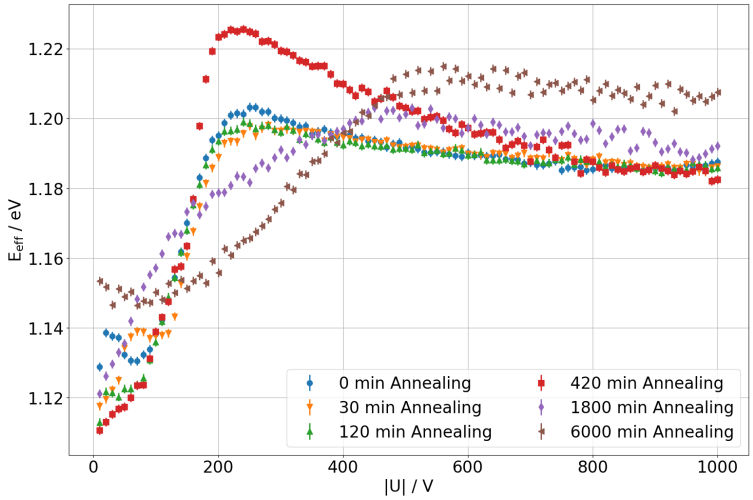

Figure A.19.: E_{eff} against voltage at different stages of annealing for P3.

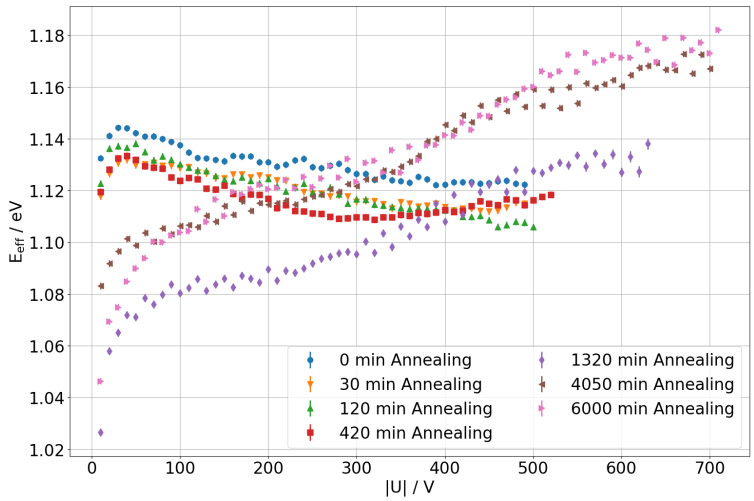

Figure A.20.: E_{eff} against voltage at different stages of annealing for P4.

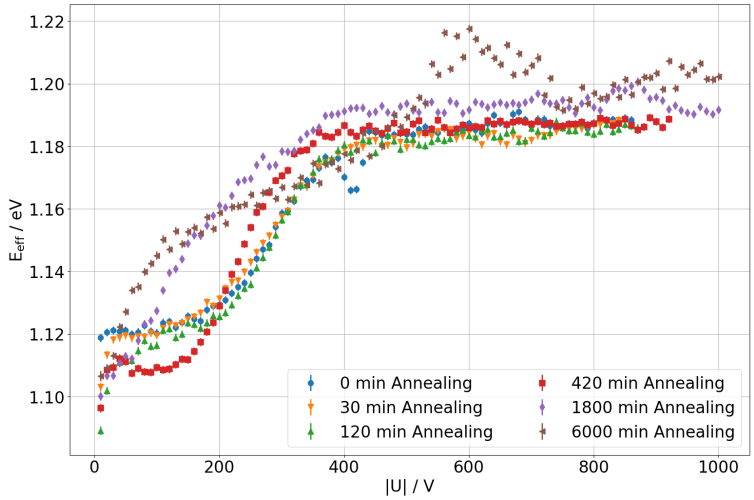

Figure A.21.: E_{eff} against voltage at different stages of annealing for P5.